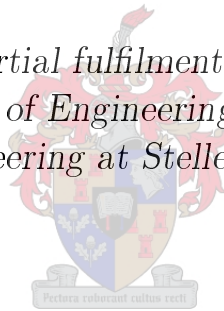


# Design, simulation, manufacture and testing of a free-piston Stirling engine

by

Ivan Niell Deetlefs

*Thesis presented in partial fulfilment of the requirements for  
the degree of Master of Engineering (Mechanical) in the  
Faculty of Engineering at Stellenbosch University*



Department of Mechanical and Mechatronic Engineering,  
Stellenbosch University,  
Private Bag X1, MATIELAND **7602**, South Africa

Supervisor: Mr. R.T. Dobson

December 2014

## Declaration

By submitting this thesis electronically, I declare that the entirety of the work contained therein is my own, original work, that I am the sole author thereof (save to the extent explicitly otherwise stated), that reproduction and publication thereof by Stellenbosch University will not infringe any third party rights and that I have not previously in its entirety or in part submitted it for obtaining any qualification.

Date: ..... 24/10/2014 .....

Copyright © 2014 Stellenbosch University  
All rights reserved.

# Abstract

## Design, simulation, manufacture and testing of a free-piston Stirling engine

I.N. Deetlefs

*Department of Mechanical and Mechatronic Engineering,  
Stellenbosch University,  
Private Bag X1, MATIELAND 7602, South Africa*

Thesis: MEng (Mech)

December 2014

The aim of this study was to design and manufacture an experimentally testable free-piston Stirling engine (FPSE), including a linear electric generator; to develop and validate a theoretical simulation model; to identify problem areas pertaining to its manufacture; and finally to assess the work undertaken, to lay out the groundwork for the future development of a 3 kWe FPSE suitable for incorporation in a solar Stirling dish power generator. A redesigned version of the Beale B-10B demonstrator engine was manufactured to overcome design difficulties and to simplify testing. The design made use of an electric generator designed at the Department of Electrical and Electronic Engineering at Stellenbosch University. Experimental measurements included piston and displacer motions, hot side and cold side temperatures, working space pressure, electric generator output, as well as heat rejection via a water jacket. Experimental measurements were taken prior to and subsequent to the addition of the electric generator. Indicated power was calculated as 0,659 W at a frequency of 10,99 Hz prior to the addition of the electric generator. The addition of the electric generator was unsuccessful since it was not well matched with the engine. The indicated power calculated was between 0,138 W and 0,144 W for different loads on the electric generator, while the electrical output power ranged from 1,23 mWe to 1,79 mWe. The addition of the electric generator produced non-continuous motion caused by magnetic forces instead of engine pressure variations. The major manufacturing difficulty was the attachment of magnets for the electric generator, but this was overcome with the manufacture of a special assembly jig. The theoretical simulation model was a combination of a third-order and dynamic analysis. Working space values were solved by the application of the conservation of mass, momentum and energy equations for a one-dimensional discretised model of the engine, while the motion of the piston and displacer was determined by applying the equations of motion. The majority of experimental measurements were predicted more accurately when higher heat transfer coefficients were used between the working space and wall

temperatures. The theoretical simulation model was used to gain insight into the effect of input parameters on engine operation. The displacer rod diameter was shown to have implications on output power and stability, while it was shown that there is a natural tendency to deliver constant output power at a near-constant frequency over a range of piston loads for an FPSE. It was also shown that the design of an FPSE is complex and that the design of all components should be done in parallel. The control of an FPSE was seen to be both a necessity and can be used to exploit the advantages of the uncoupled nature of an FPSE.

# Uittreksel

## Ontwerp, simulاسie, vervaardiging en toets van 'n vrye-werksuier Stirling enjin

I.N. Deetlefs

*Departement Meganiese en Megatroniese Ingenieurswese,  
Universiteit van Stellenbosch,  
Privaatsak X1, MATIELAND 7602, Suid Afrika*

Tesis: MIng (Meg)

Desember 2014

Die doel van hierdie studie was om 'n eksperimentele toetsbare vrye-werksuier Stirling enjin te vervaardiging, wat 'n lineêre elektriese kragopwekker insluit; om 'n teoretiese simulاسie model te ontwikkel en te yk; om vervaardiging probleme te identifiseer; en om die ondernemende werk te assesseer om 'n fondasie te lê vir die toekomstige ontwikkeling van 'n 3 kWe vrye-werksuier Stirling enjin wat by 'n Stirling sonskottel ingelyf kan word. 'n Herontwerpte weergawe van die Beale B-10B demonstrاسie enjin was vervaardig om ontwerp probleme te bowe te kom en om die toets daarvan te vereenvoudig. Die ontwerp het gebruik gemaak van 'n elektriese kragopwekker wat by die Departement Elektriese en Elektroniese Ingenieurswese aan die Universiteit van Stellenbosch ontwerp is. Eksperimentele metings het die werksuier en verplaser bewegings ingesluit, sowel as die warm kant en koue kant temperature, die werkruimte druk, die elektriese uitset van die kragopwekker, sowel as die hitteuitruiling wat met 'n water verkoelingskringloop gepaard gaan. Eksperimentele metings was geneem voor en na die byvoeging van die elektriese kragopwekker. Kraglewering was bereken op 0,659 W teen 'n frekwensie van 10,99 Hz voordat die elektriese kragopwekker bygevoeg is. Die byvoeging van die elektriese kragopwekker was onsuksesvol omdat die nie gepas was vir die enjin nie. Die kraglewering is bereken op vlakke wat gewissel het tussen 0,138 W en 0,144 W vir die verskillende belastings op die elektriese kragopwekker, terwyl die elektriese uitset gewissel het tussen 1,23 mWe en 1,79 mWe. Die byvoeging van die elektriese kragopwekker het 'n nie-aaneenlopende beweging veroorsaak weens die magnetiese kragte wat dit beïnvloed het in plaas van enjindruk variasies. Die belangrikste ontwerpuitdagings was die ontwerp van 'n werksuier en verplaser wat 'n klein toleransie passing kon handhaaf om sodoende 'n seël te verseker terwyl dit aan temperatuur variasies blootgestel was. Die grootste vervaardigingsprobleem was die aanheg van magnete vir die elektriese kragopwekker, maar dit is te bowe gekom deur 'n spesiale voeg te vervaardig. Die teoretiese simulاسie model was 'n kombinasie van 'n derde-orde en 'n dinamiese analise. Werkruimte waardes

was opgelos deur die toepassing van die behoud van massa, momentum en energie vergelykings vir 'n een-dimensionele gediskretiseerde model van die enjin, terwyl die beweging van die werksuier en verplaser bepaal was deur die toepassing van die bewegingvergelings. Die meerderheid van die eksperimentele metings was meer akkuraat voorspel wanneer hoër warmteoordrag koëffisiënte tussen die werkruimte en muurtemperatuur gebruik was. Die teoretiese simulasiemodel was gebruik om insig in terme van die effek van invoer veranderlikes op die enjin gedrag te toon. Daar was getoon dat die verplaserstaaf diameter implikasies het op kragoplewing en stabiliteit, terwyl die natuurlike tendens van 'n vrye-werksuier Stirling enjin gewys was om 'n konstante kraguitvoer te lewer op 'n naby-konstante frekwensie oor 'n reeks werksuier laste. Daar was ook gewys dat die ontwerp van 'n vrye-werksuier Stirling enjin kompleks is en dat die ontwerp van alle komponente in parallel gedoen moet word. Die beheer van 'n vrye-werksuier Stirling enjin was gewys om beide noodsaaklik te wees, sowel as gebruik kan word om die unieke voordele van 'n vrye-werksuier Stirling enjin se ongekoppelde natuur te ontgin.

# Acknowledgements

*The author would like to acknowledge the following people for their assistance during the project:*

*The Mechanical Engineering Department Workshop, for their help and advice on manufacturing.*

*My supervisor, Mr R.T. Dobson, for his advice, and for his financial and comical contributions to this project.*

# Contents

<b>Declaration</b>	<b>i</b>
<b>Abstract</b>	<b>ii</b>
<b>Uittreksel</b>	<b>iv</b>
<b>Acknowledgements</b>	<b>vi</b>
<b>List of Figures</b>	<b>x</b>
<b>List of Tables</b>	<b>xiii</b>
<b>Nomenclature</b>	<b>xiv</b>
<b>1 Introduction</b>	<b>1</b>
<b>2 Literature study</b>	<b>4</b>
2.1 Background . . . . .	4
2.1.1 Workings of a Stirling engine . . . . .	4
2.1.2 Kinematic and free-piston . . . . .	5
2.2 Theoretical simulation methods . . . . .	7
2.2.1 Cycle analysis . . . . .	8
2.2.2 Second-order analysis . . . . .	12
2.2.3 Third-order analysis . . . . .	12
2.2.4 Dynamic analysis . . . . .	13
2.3 Stirling engine configurations . . . . .	14
2.3.1 Alpha configuration . . . . .	14
2.3.2 Beta configuration . . . . .	15
2.3.3 Gamma configuration . . . . .	16
2.3.4 Stirling configuration comparisons . . . . .	16
2.4 Performance parameters . . . . .	18
2.4.1 Operating pressure . . . . .	18



2.4.2	Dead space . . . . .	18
2.4.3	Temperature ratio . . . . .	19
2.5	Physical considerations . . . . .	20
2.5.1	Close tolerance sealing . . . . .	20
2.5.2	Centring . . . . .	20
2.5.3	Piston and displacer restoring force . . . . .	22
<b>3</b>	<b>Theoretical simulation model</b>	<b>24</b>
3.1	Introduction . . . . .	24
3.2	Piston and displacer motion . . . . .	24
3.3	Cell and nodal network . . . . .	27
3.4	Solution of system equations . . . . .	28
3.5	Program flow . . . . .	32
3.6	Initialising . . . . .	34
3.7	Software and sample calculations . . . . .	36
3.8	Validation . . . . .	37
<b>4</b>	<b>Design</b>	<b>42</b>
4.1	Introduction . . . . .	42
4.2	Initial design challenges . . . . .	42
4.3	Design description . . . . .	43
4.4	Electric generator . . . . .	45
4.5	Annulus size . . . . .	48
4.6	Design by simulation . . . . .	49
<b>5</b>	<b>Experimental test setup</b>	<b>55</b>
5.1	Experimental test setup design . . . . .	55
5.2	Measuring equipment . . . . .	59
<b>6</b>	<b>Results and discussion</b>	<b>62</b>
6.1	Setting equipment references . . . . .	62
6.2	Engine test without electric generator . . . . .	63
6.3	Engine test with electric generator . . . . .	69
<b>7</b>	<b>Conclusions</b>	<b>74</b>
	<b>Appendices</b>	<b>78</b>
<b>A</b>	<b>Calibration</b>	<b>A.1</b>
A.1	Method . . . . .	A.1
A.2	Data-logging equipment . . . . .	A.1
A.3	Compression springs . . . . .	A.2

A.4	Laser displacement sensors . . . . .	A.5
A.5	Pressure sensor . . . . .	A.7
A.6	Multimeter . . . . .	A.11
A.7	Thermocouples . . . . .	A.12
	A.7.1 Calibration equipment . . . . .	A.12
	A.7.2 Temperature references . . . . .	A.13
	A.7.3 Results . . . . .	A.13
<b>B</b>	<b>Theoretical simulation equations</b>	<b>B.1</b>
B.1	Fundamental equations . . . . .	B.1
	B.1.1 Mass . . . . .	B.2
	B.1.2 Momentum . . . . .	B.3
	B.1.3 Energy . . . . .	B.4
B.2	Discretisation . . . . .	B.7
	B.2.1 Mass . . . . .	B.8
	B.2.2 Energy . . . . .	B.8
<b>C</b>	<b>Source code</b>	<b>C.1</b>
<b>D</b>	<b>Sensitivity analysis</b>	<b>D.1</b>
	<b>List of References</b>	<b>E.1</b>

# List of Figures

2.1	Compartments of a Stirling engine. (c) Compression space, (k) Cooler, (r) Regenerator, (h) Heater, (e) Expansion space. . . . .	5
2.2	Stirling engine comparison. (a) Free-piston Stirling engine, (b) Kinematic Stirling engine. . . . .	6
2.3	A comparison of work done per cycle between the ideal Stirling cycle and ideal Carnot cycle. . . . .	9
2.4	Dynamic analysis. . . . .	13
2.5	Stirling engine configurations. (a) Alpha configuration, (b) Beta configuration, (c) Gamma configuration. . . . .	15
2.6	Comparison of gamma configuration using the post-and-flange design and beta configuration. (a) Post-and-flange gamma configuration, (b) Beta configuration. . . . .	17
2.7	Air flow in a typical gas bearing. . . . .	21
2.8	Standard shaker (Peckham Engineering and Tool, 1994). . . . .	21
2.9	Three common methods of achieving a restoring force. (a) Gas spring, (b) Flexure bearing, (c) Compression spring. . . . .	22
3.1	Free body diagrams. (a) Piston, (b) Displacer. . . . .	25
3.2	Cell and nodal networks. . . . .	28
3.3	Cell and node interaction. . . . .	29
3.4	Theoretical simulation model flow diagram. . . . .	33
3.5	Extrapolated wall temperature profile. . . . .	35
3.6	Piston motion. . . . .	38
3.7	Displacer motion. . . . .	39
3.8	Pressure curves. . . . .	40
4.1	Engine comparison. (a) Beale B-10B demonstrator engine (Sunpower Inc.), (b) Presented engine. . . . .	44
4.2	Electric generator assembly. (a) Stator assembly, (b) Magnet assembly. . . . .	46

4.3	Attachment of magnets in a Halbach configuration. (a) Magnet configuration and magnetisation, (b) Tendency of adjacent magnets to move away from the magnet holder, (c) Assembly jig. . . . .	47
4.4	Output power versus load added to piston. . . . .	50
4.5	Effect on engine operation as piston load is increased. . . . .	51
4.6	Effect on engine operation as displacer rod diameter is decreased. . . . .	52
4.7	Effect on engine operation. (a) Increasing piston spring stiffness, (b) Increasing displacer spring stiffness, (c) Increasing piston mass, (d) Increasing displacer mass. . . . .	54
5.1	Experimental test setup. . . . .	56
5.2	Recesses and thermocouple clearance grooves. (a) Heater head end cap, (b) Cooler section. . . . .	57
5.3	Thermocouple insertion. (a) Cross-section of end cap groove, (b) Cross-section of cooler section groove. . . . .	57
5.4	Heater head prior to insulation addition. . . . .	58
5.5	Photo of experimental test setup. . . . .	60
6.1	Reference positions. . . . .	62
6.2	Piston and displacer motions. . . . .	64
6.3	Variations in volume of compression and expansion space. . . . .	65
6.4	Pressure curve. . . . .	66
6.5	Resultant pressure-volume curve. . . . .	67
6.6	Piston and displacer motions. . . . .	70
6.7	Electric generator output voltage. . . . .	71
6.8	Variations in the volume of the compression and expansion space. . . . .	72
6.9	Pressure curve. . . . .	73
A.1	Spring calibration rig. . . . .	A.3
A.2	Calibration curve for piston compression spring. . . . .	A.4
A.3	Calibration curve for displacer compression spring. . . . .	A.5
A.4	Calibration curve for laser 1. . . . .	A.6
A.5	Calibration curve for laser 2. . . . .	A.7
A.6	Pressure calibration setup. . . . .	A.8
A.7	Calibration curve for pressure sensor. . . . .	A.9
A.8	Vacuum test setup. . . . .	A.10
A.9	Vacuum test results. . . . .	A.11
A.10	Calibration curve for multimeter. . . . .	A.12
A.11	Aluminium billet calibrating device. . . . .	A.14
A.12	Calibration curves for thermocouples calibrated with Fluke field metrology well. (a) $T_{cold}$ , (b) $T_{w\_in}$ , (c) $T_{w\_out}$ . . . . .	A.15

A.13	Calibration curve for $T_{hot}$ . . . . .	A.16
A.14	Calibration curves for thermocouples calibrated with JMM thermal well. (a) $T_{wall\_1}$ , (b) $T_{wall\_2}$ , (c) $T_{wall\_3}$ , (d) $T_{wall\_4}$ . . . . .	A.17
B.1	Control volume and control surface illustration. . . . .	B.1
B.2	Illustration of cells and nodes. . . . .	B.8
D.1	Piston and displacer motions. (a) $C_{pd} = 10$ N s/m, (b) $C_{pd} = 5$ N s/m, (c) $C_{pd} = 2, 5$ N s/m. . . . .	D.2

# List of Tables

3.1	Sample calculations with $Nu = 50$ , $Cf_p = 6 \text{ N s/m}$ , $v_p = 0$ and $v_d = 0$ .	36
3.2	Summary of theoretical simulation results. . . . .	41
6.1	Summary of the experimental test of the presented engine without electric generator. . . . .	68
6.2	Summary of the experimental test of the presented engine with electric generator. . . . .	71
A.1	Data-logging card details (National Instruments). . . . .	A.2
A.2	Linear curve fit results for compression spring calibration. . . . .	A.4
A.3	Linear curve fit results for laser 1 and laser 2 calibration. . . . .	A.6
A.4	Pressure sensor specifications. . . . .	A.8
A.5	Linear curve fit results for pressure sensor calibration. . . . .	A.10
A.6	Multimeter calibration. . . . .	A.11
A.7	Temperature-generating equipment. . . . .	A.13
A.8	Sub-standard calibration. . . . .	A.14
A.9	Thermocouple calibration. . . . .	A.16
D.1	Summary of sensitivity analysis results. . . . .	D.1

## Nomenclature

$A$	area, m <sup>2</sup>
$A_n$	cross-sectional area at node, m <sup>2</sup>
$A_{wall}$	area between wall cell and working space cell, m <sup>2</sup>
$c_p$	constant pressure specific heat, J/kg K
$c_v$	constant volume specific heat, J/kg K
$D$	diameter, m
$D_h$	hydraulic diameter, m
$D_i$	annulus inner diameter, m
$D_o$	annulus outer diameter, m
$F$	force, N
$F_f$	frictional force, N
$F_k$	spring force, N
$G$	generator voltage, V
$g$	mass flux, kg/m <sup>2</sup> s
$h$	convection heat transfer coefficient, W/m <sup>2</sup> K
$h$	specific enthalpy, J/kg
$k$	iteration variable
$k$	spring constant, N/m
$k$	thermal conductivity, W/m K
$L$	length, m
$M$	total mass of working fluid, kg
$m$	mass, kg
$N_{cell}$	number of working space cells
$N_{wall}$	number of wall cells
$Nu$	Nusselt number
$p$	pressure, Pa
$Q$	total heat transfer, J
$R$	specific gas constant, J/kg K
$Re$	Reynolds number
$T$	temperature, K
$T_n$	conditional temperature at node, K

$T_{wall}$	wall cell temperature, K
$T_{wall\_1}$	temperature at position 1 along heater head exterior, K
$T_{wall\_2}$	temperature at position 2 along heater head exterior, K
$T_{wall\_3}$	temperature at position 3 along heater head exterior, K
$T_{wall\_4}$	temperature at position 4 along heater head exterior, K
$t$	time, s
$u$	specific internal energy, J/kg
$V$	volume, m <sup>3</sup>
$V_{c0}$	compression space volume constant, m <sup>3</sup>
$V_{e0}$	expansion space volume constant, m <sup>3</sup>
$v$	velocity, m/s
$W$	work, J
$X$	stroke amplitude, m
$x$	displacement, m
$x_{d0}$	displacer equilibrium position, m
$x_{p0}$	piston equilibrium position, m

**Greek symbols**

$\alpha$	phase, rad
$\mu$	dynamic viscosity, kg/m s
$\nu$	specific volume, m <sup>3</sup> /kg
$\rho$	density, kg/m <sup>3</sup>
$\omega$	angular velocity, rad/s

**Subscripts**

<i>bounce</i>	bounce space
<i>c</i>	compression space
<i>cold</i>	cold side
<i>d</i>	displacer
<i>e</i>	expansion space
<i>eff</i>	effective
<i>h</i>	heater
<i>hot</i>	hot side
<i>i</i>	<i>i</i> -th working space element
<i>j</i>	<i>j</i> -th wall element



<i>k</i>	cooler
<i>p</i>	piston
<i>pd</i>	between piston and displacer
<i>r</i>	regenerator
<i>ref</i>	reference
<i>rod</i>	displacer rod
<i>w_in</i>	inlet to water jacket
<i>w_out</i>	outlet to water jacket

### **Superscripts**

<i>t</i>	at time t, s
$\Delta t$	time step duration, s

### **Acronyms and initialisms**

CHP	combined heat and power
CSP	concentrated solar power
CTPC	component test power converter
FPSE	free-piston Stirling engine
GRC	Glenn Research Center
IRENA	International Renewable Energy Agency
NASA	National Aeronautics and Space Administration (USA)
PV	photovoltaic
PVC	polyvinyl chloride
SPDE	space power demonstrator engine

# 1 Introduction

The Stirling engine is a reciprocating, external combustion engine that converts heat into mechanical energy by means of the expansion and contraction of a contained working fluid, usually a gas. The original Stirling engine was invented in 1816 by the Reverend Robert Stirling (Sier, 1995) and is now classified as a *kinematic Stirling engine*. A kinematic Stirling engine uses a typical crank mechanism with a flywheel to produce a 90° out of phase reciprocating motion of the piston parts.

In 1964, however, the *free-piston Stirling engine (FPSE)* was invented by William Beale, a professor of Mechanical Engineering at Ohio University (web, 2014a).

The FPSE is unique in that it eliminates all wearing mechanisms associated with a kinematic Stirling engine and thus eliminates the need for lubricant. It replaces the crank mechanism of the kinematic Stirling engine by a linear mechanical storage device such as a compression spring. Side forces on the piston parts are eliminated in this manner and it provides the FPSE with the possibility of extremely long operating life, higher efficiency and zero maintenance.

In spite of all of these advantages, however, the commercial deployment of FPSE products has largely been unsuccessful. Infinia Corporation, for example, arguably the world's leading manufacturer of free-piston Stirling cycle engines for distributed power, recently filed for Chapter 11 relief, which led to its take over by Qnergy (web, 2013b).

It is believed, however, that a 3 kWe FPSE solar concentrating dish for rural off-grid electric power supply could be a suitable application for an FPSE and this study forms part of this ultimate aim. The main reasons are that theft of photovoltaic panels are a problem, while low maintenance and reliability are essential to rural off-grid power. In order to design an FPSE, however, a theoretical simulation model first needs to be developed and validated to be used for its design.

A limited amount of experimental data for FPSEs is available in the literature (Formosa and Fr chet te, 2013), however. Available data is also usually restricted in the amount of measured variables. This makes it difficult to convincingly validate a theoretical simulation model. A study done by Saturno (1994), for example, made use of the experimental test results of the Beale B-10B demonstrator engine (Sunpower Inc.), but measurements were restricted to the piston motion and hot side temperature only. An experimentally testable engine with an adequate amount of measurable variables is thus needed to validate a theoretical simulation model.

Research and development FPSE units are only available at very high cost,

however. Prices for purchasable units from Sunpower Inc. and the Microgen Engine Corporation were investigated by means of direct correspondence with the companies. A 1 kW developer's kit from Sunpower Inc. (web, 2014b) was available for purchase, as well as a 1 kW unit from the Microgen Engine Corporation, which is also based on Sunpower Inc. technology (web, 2013a).

This study is aimed at solving this problem. Experimental test results need to be generated and a theoretical simulation model needs to be developed to validate these results, and in light of what is mentioned above, necessitates the need for the manufacture of an experimentally testable FPSE.

Originally, the development of the 3 kWe FPSE was an objective of this study but it was soon realised that this would require efforts beyond which could be provided by this study. The objectives were then redirected to design and manufacture an experimental engine that could be tested to validate a theoretical simulation model. The addition of a linear electric generator was also to be incorporated into the design. The electric generator design forms part of ongoing development at the Department of Electrical and Electronic Engineering at Stellenbosch University (Joubert *et al.*, 2012).

The final objectives of this study therefore were to design and manufacture an experimentally testable FPSE, including a linear electric generator; to develop and validate a theoretical simulation model; to identify problem areas pertaining to its manufacture; and finally to assess the work undertaken, to lay out the groundwork for the future development of a 3 kWe FPSE suitable for incorporation in a solar Stirling dish power generator.

The design of the FPSE would only be aimed at producing an experimentally testable engine. Not to design an optimised engine, but rather to design an engine that could be used for testing and experimentation. The design of the electric generator would be provided by the Department of Electrical and Electronic Engineering at Stellenbosch University, while the manufacture would be the responsibility of the author. The theoretical simulation model would be based on the application of the conservation of mass, momentum and energy equations for a one-dimensional discretised model of the engine. This would allow it to be developed into a fully descriptive model and powerful design tool. The experimental results produced by testing the engine would be used to validate the theoretical simulation model. The identification of problem areas with regard to manufacture would include that of the engine itself, as well as the electrical generator. Although the problem areas were to be constrained mostly to the actual manufactured engine, it could also include possible areas of concern to be encountered in future as the design progresses. The assessment of the work undertaken would include the investigation, in more general terms, of where challenges would be encountered to realise the development of a 3 kWe FPSE.

Two experimental engines had to be manufactured. The first engine made use of the *standard shaker* type flexure bearings, of which design information is not readily available. The process of manufacturing and testing these flexure bearings was very time consuming. This, and challenges with achieving a smooth running piston and displacer that could seal effectively caused the design to be redirected. The design was redirected to alter the design of the Beale B-10B demonstrator engine instead.

The piston and displacer of the Beale B-10B demonstrator engine were retained and most of the dimensions. The design of the Beale B-10B demonstrator engine was, however, changed to include components such as a water jacket and electric generator. This engine was designed to be experimentally tested and provided the means of validating the theoretical simulation model.

The theoretical simulation model provided satisfactory results when compared to experimental test results. It also provided insight into the effect of input parameters on engine operation.

The addition of the electric generator was not successful, however. The electric generator and engine were not well matched. The engine parameters that the electric generator was designed for (that of the first experimental engine), were not achieved because of the redirection to the design based on the Beale B-10B demonstrator engine. The addition of the electric generator is included in the study, however, since an important contribution is made with regard to its assembly. The attachment of the permanent magnets for the electric generator has been a challenge in past attempts because of the attractive and repulsive forces between them.

## 2 Literature study

This literature study starts with a short background and then addresses central themes relevant to the study at hand. The central themes relate to methods of designing an FPSE by theoretical simulation, comparing different engine configurations, determining basic performance parameters and identifying physical considerations that are unique to FPSEs.

### 2.1 Background

This short background explains how the Stirling engines works in principle, as well as how the free-piston and kinematic Stirling engines differ from one another. A mention is also made of where the idea of a free-piston originated.

#### 2.1.1 Workings of a Stirling engine

The Stirling engine functions on the principle of cyclically heating and cooling a contained working fluid, which usually is a gas. The working fluid is sealed off by a piston that runs in a cylinder. As the working fluid is heated it increases in pressure and forces the piston outward. The working fluid is subsequently cooled and the piston retracts.

Since the Stirling engine is an external combustion machine, the hot and cold sides of the engine are separated. The working fluid is heated by being moved to the hot side of the engine and cooled by being moved to the cold side of the engine. In order to move the working fluid, an additional piston is needed, named the displacer. A Stirling engine thus usually comprises of a piston which outputs the mechanical work and a displacer which is made as light as possible to move working fluid between the hot and cold sides of the engine.

Figure 2.1 shows how the Stirling engine is divided into different compartments, which each have a specific function. The compression space and cooler are located on the cold side of the engine while the heater and expansion space are located on the hot side of the engine. Temperature in the regenerator is distributed between the cooler and heater temperatures.

For a heat engine to produce a net amount of work, less work should be expended during compression of the working fluid than work output during expansion. Most of the working fluid should thus be on the cold side of the engine during compression and most of the working fluid should be on the hot side of the engine during expansion. The compression and expansion spaces were thus named accordingly.

The cooler is responsible for cooling air that comes from the regenerator on its way to the compression space. The opposite is true for the heater. The regenerator serves as a thermal heat store that either supplies heat to the working fluid on its

way to the heater or removes heat from the working fluid on its way to the cooler. The regenerator usually consists of a stack of wire mesh and can be thought of as a thermal sponge.

### 2.1.2 Kinematic and free-piston

The idea of a free-piston did not start with the Stirling engine. The first free-piston engine was an internal combustion single-piston spark-ignited air compressor patented in 1928 by R.P. Pescara (U.S. patent 1 657 641). Free-piston internal combustion engines that have produced experimental results include the air compressor, gas generator, hydraulic engine and electrical generator (Mikalsen and Roskilly, 2007).

The relative movement of the piston and displacer for Stirling engines, termed the phase, is very important to ensure the location of the working fluid. A Stirling engine produces no power if the piston and displacer are in phase.

In a kinematic engine, the phase is set by mechanically linking the piston and displacer with a crank mechanism and flywheel. The FPSE achieves this by replacing the crank mechanism with a linear storage device attached to both the piston and displacer respectively. The piston and displacer thus become uncoupled. A linear storage device refers to the fact that it acts only along the direction of the piston or displacer motion, i.e. there are no side forces. Examples of a linear storage device include a compression spring, gas spring and flexure bearing. A graphical comparison is given in Figure 2.2.

There are many advantages that an FPSE provides over a kinematic engine. Firstly, all wearing mechanisms can be eliminated since there are no more side forces on the piston and displacer. If there are no side forces on the piston, there is no need for lubrication and sealing can now be achieved by a small tolerance sliding fit of the piston and displacer.

Hermetic sealing and pressurisation is possible for both the kinematic Stirling engine and FPSE. A higher operating pressure, relates to increased power density.

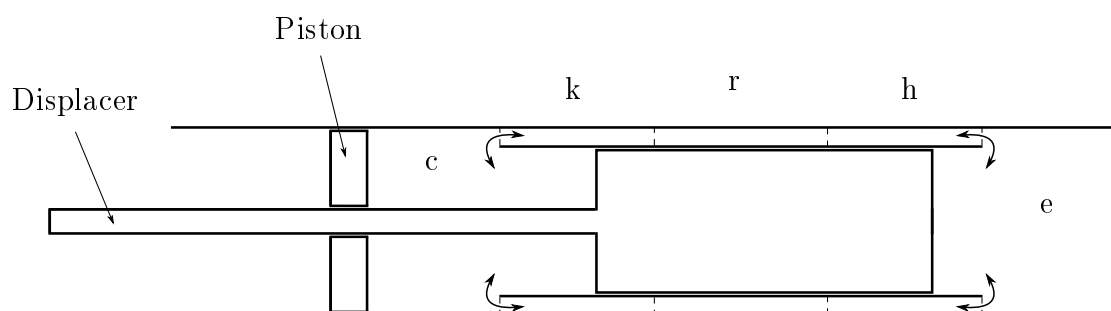


**Figure 2.1:** Compartments of a Stirling engine. (c) Compression space, (k) Cooler, (r) Regenerator, (h) Heater, (e) Expansion space.

Cheng and Yang (2012) also showed that, for a kinematic Stirling engine, the performance is highly dependent on mechanism effectiveness. For one instance, the maximum dimensionless shaft work was nearly double when the mechanism effectiveness was increased from 0,7 to 0,8. In a free-piston configuration, the mechanism effectiveness essentially is 1.

Most of the FPSE advantages have arguably not yet been proven beyond reasonable doubt. The kinematic engine also has been researched in much greater depth, especially by Philips of the Netherlands. Between the 1930s and 1970s, Philips produced Stirling engines of up to 224 kW output and also was responsible for the invention of the Rhombic drive, which is used as the crank mechanism for a beta configuration kinematic engine (Cinar *et al.*, 2005). In spite of all development efforts of the kinematic Stirling engine, engineering challenges have not allowed the full potential of Stirling engines to be realised and they have been unsuccessful commercially (Lane and Beale, 1997).

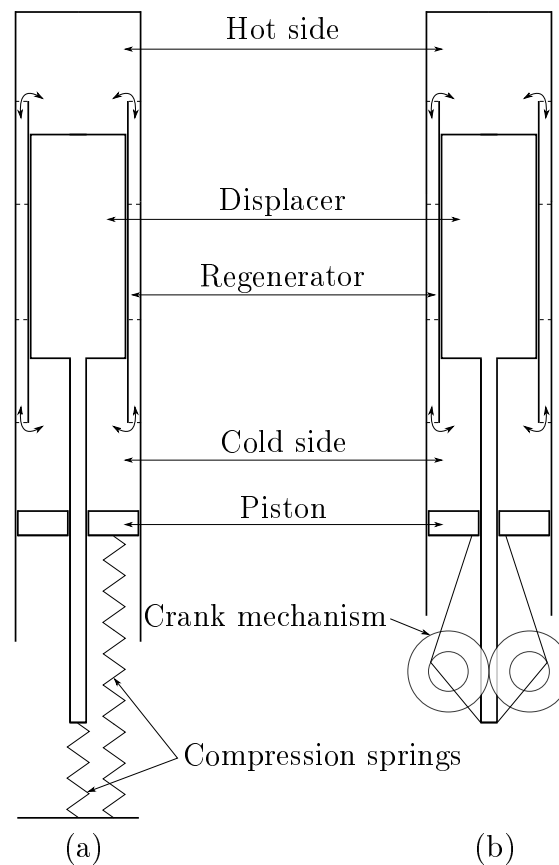


**Figure 2.2:** Stirling engine comparison. (a) Free-piston Stirling engine, (b) Kinematic Stirling engine.

The FPSE has the potential to solve most of the engineering problems associated with the kinematic Stirling engine. The unproven status of the FPSE has led NASA GRC to conduct tests on a number of FPSEs with the aim of providing long-term performance data on multiple units to build a life and reliability database (Oriti, 2012). By August 2012, GRC had been operating 38 FPSE electric generators, 18 of which were ongoing. The units tested include Technology Demonstration Convertors (TDCs) from Infinia Corporation and Advanced Stirling Convertors (ASCs) from Sunpower, Inc.

The majority of shut downs have been as a result of support facility issues and not the FPSE units. One shut down was because of air ingress into one of the horizontally opposed units (TDC #13 and TDC #14) that led to oxidation of the stainless steel regenerator. This was addressed by welding the unit to ensure hermetic sealing (Schreiber and Thieme, 2007). TDC #13 and TDC #14 are also the longest running pair of Stirling convertors at GRC and, since June 2003, had accumulated over 60 000 hours (6,8 years) of operation by 2012 (Oriti, 2012).

More recently, however, the ASC-E2 units (#1, #2, #3 and #4) have produced conversion efficiencies of between 32% and 38% (according to the GRC method for calculating net heat input) (Oriti and Wilson, 2011).

The many advantages of FPSEs are also the limiting factors of their performance and commercial viability. Operating at higher temperatures and pressures has negative effects on life, reliability and cost. Creep becomes especially important with high operating temperatures. The greatest design requirements, according to Noble *et al.* (1990), are those of creep rupture and creep and fatigue interaction. Creep is characterised by plastic deformation occurring under a load below the yield point and is always related to temperature and time.

Not much data of Stirling engine failure is available, although NASA GRC recently started a programme for the durability testing of FPSEs that were designed for the ASRG programme (Meer and Oriti, 2012). Testing consists of operating the units in regions beyond those intended to meet the product specification, specifically to determine the effect of lateral contact, overstroke and over-temperature events.

## 2.2 Theoretical simulation methods

This section is aimed at highlighting the advantages and disadvantages of the available theoretical simulation models which led to the resultant simulation code.

Historically, theoretical simulation of Stirling engines has been divided into first-, second- and third-order analysis methods. First-order is the least complex and third-order is the most complex.

The methods discussed here start with thermodynamic cycle analysis methods, which form the basis for other methods, and then proceeds with second-order through to third-order methods. Finally, a mention is made of dynamic analysis,



which is unique to FPSEs because of the coupling between the thermodynamics and engine dynamics. First-order analysis is omitted, since it does not provide great use for design purposes.

### 2.2.1 Cycle analysis

Cycle analysis is an ideal depiction of what is happening in a Stirling engine and is hence never used on its own. It rather is used as the basis for other methods, especially second-order methods. The three cycles generally used are the ideal Stirling cycle, the ideal isothermal model and the ideal adiabatic model.

These three forms of cycle analysis are now discussed.

#### Ideal Stirling cycle

The ideal Stirling cycle has been created for internal combustion engines to depict the theoretical thermodynamic cycle that the working fluid experiences. It assumes that all working fluid goes through the same set of processes. The ideal Stirling cycle, as shown in Figure 2.3, comprises four processes:

**1-2:** isothermal compression

**2-3:** constant volume heat addition

**3-4:** isothermal expansion

**4-1:** constant volume heat rejection

As the working fluid is pushed through the regenerator it either heats or cools the working fluid, producing a constant volume heating or cooling process. As the compression and expansion processes occur, heat is either removed or supplied by the cooler or heater. This compression or expansion process is assumed to happen isothermally.

It can be proven that the thermal efficiency of the ideal Stirling cycle is equal to the ideal Carnot efficiency, which is the theoretical maximum for any heat engine (see Equation 2.1). It is important to note that the heat addition and heat rejection processes at constant volume must be accomplished by the regenerator. This is required so that these two processes are not included in the calculation of efficiency ( $\eta$ ). The heat input ( $Q_{in}$ ) and heat output ( $Q_{out}$ ) thus are calculated only from the compression and expansion processes respectively:

$$\eta_{th,Stirling} = \frac{Q_{in} - Q_{out}}{Q_{in}} = 1 - \frac{T_{cold}}{T_{hot}} = \eta_{th,Carnot} \quad (2.1)$$

The work done per cycle, however, is greater for the Stirling cycle than for the Carnot cycle for the same extremes in temperature and volume. This is illustrated in Figure 2.3 by superimposing the Carnot cycle onto the Stirling cycle:

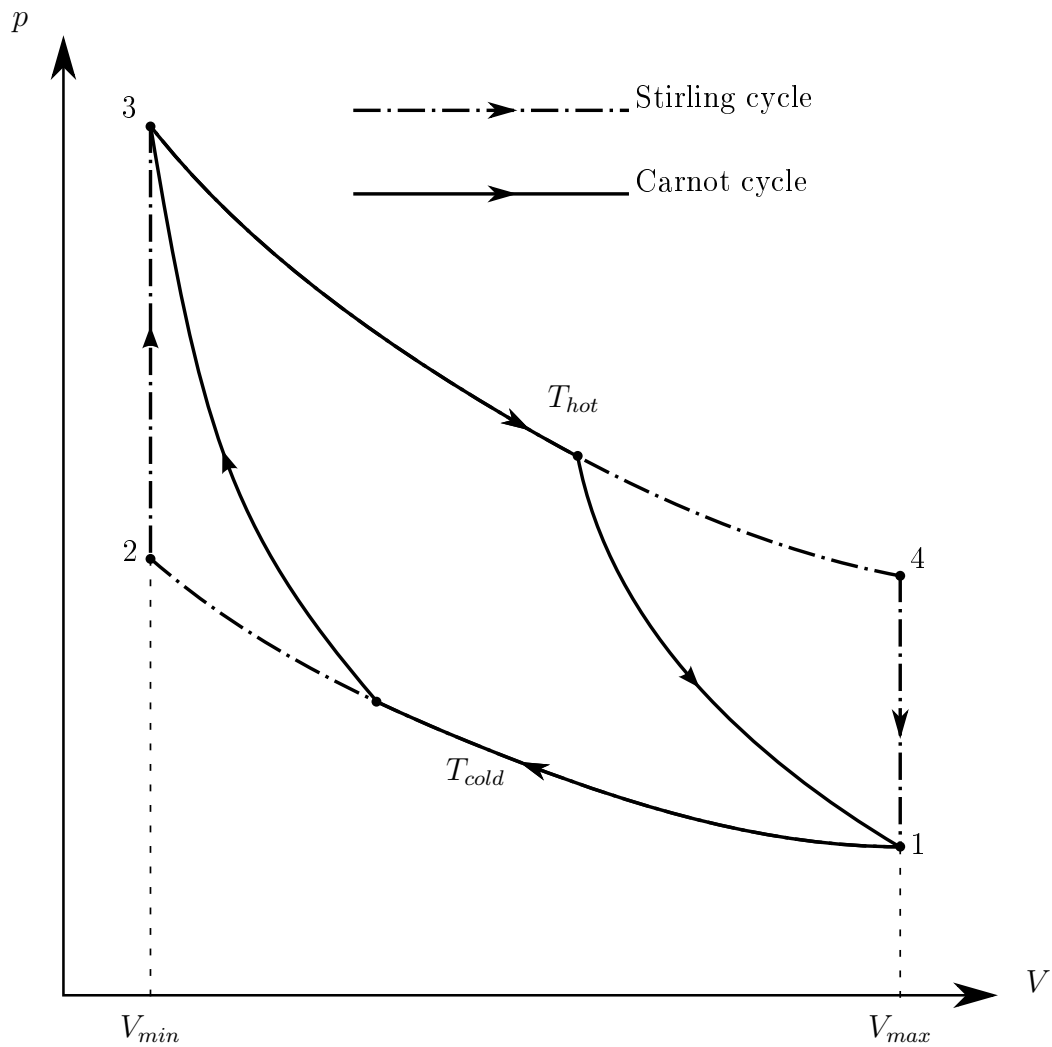


**Figure 2.3:** A comparison of work done per cycle between the ideal Stirling cycle and ideal Carnot cycle.

$$\left( \oint dW \right)_{Stirling} > \left( \oint dW \right)_{Carnot} \quad (2.2)$$

The Stirling cycle, however, is not the only cycle to have an efficiency equal to the Carnot efficiency. The Stirling cycle and Carnot cycle both fall under the Reitlinger cycle, which consists of two isothermal processes and two polytropic processes of the same kind (Senft, 2007). If perfect regeneration is achieved between the two polytropic processes, the efficiency equals that of Carnot, since  $Q_{in}$

is again determined only by isothermal expansion and  $Q_{out}$  by isothermal compression. The Carnot cycle actually requires no regeneration, since its polytropic processes are adiabatic.

For larger Stirling engines, however, it is more difficult to get heat into the engine. As the diameter of the Stirling engine increases, the volume of working fluid increases quadratically, while the heat transfer area to the working fluid only increases linearly. The compression and expansion processes are then better approximated as adiabatic instead of isothermal. This reduces the Stirling cycle to the Otto cycle, also named the adiabatic Stirling cycle:

**1-2:** adiabatic compression

**2-3:** constant volume heat addition

**3-4:** adiabatic expansion

**4-1:** constant volume heat rejection

This is an inherent problem with Stirling engines. Many designs make use of very complicated heater heads to increase heat transfer, such as the ‘starfish’ heater head used in the 25 kWe FPSE designed by MTI for NASA under the SSE program (Dhar, 1999*a*). This firstly increases manufacturing complexity and cost, and secondly increases the possibility of failure, since most of these designs require many welding joints which are subject to stress under thermal cycling.

### **Schmidt model (ideal isothermal model)**

Owing to the fact that the Stirling engine has different compartments at different temperatures, not all of the working fluid experiences the same thermodynamic cycle. The Schmidt model was conceived by assuming that each of the five major engine compartments are isothermal, namely the compression space, cooler, regenerator, heater and expansion space. The compression space and cooler are assumed to be at the heat sink temperature ( $T_{cold}$ ) and the heater and expansion space are assumed to be at the heat source temperature ( $T_{hot}$ ). The model then goes further to include the volume changes of the compression and expansion spaces by means of assuming sinusoidal motion with a phase shift between them. Since all the spaces are considered isothermal, the Schmidt model is sometimes named the isothermal model.

The assumptions of the Schmidt model are summarised as follows:

1. sinusoidal movement of parts
2. temperatures are known for the different compartments of the engine
3. working fluid is an ideal gas

4. pressure is the same throughout the engine
5. constant mass of working fluid ( $M = const$ ), i.e. no leakage

An important outcome is that an equation for pressure is produced that is defined for the entire cycle. The equation for pressure comes to the following:

$$p = \frac{MR}{V_e/T_e + V_h/T_h + V_r/T_r + V_k/T_k + V_c/T_c} \quad (2.3)$$

After inserting the isothermal temperature assumptions, we get the following:

$$p = \frac{MR}{V_{hot}/T_{hot} + V_r/T_r + V_{cold}/T_{cold}} \quad (2.4)$$

Only the effective regenerator temperature ( $T_r$ ) must be written in terms of  $T_{hot}$  and  $T_{cold}$ . A linear temperature profile is assumed along the length ( $L_r$ ) of the regenerator, which is integrated with respect to mass over its length and then compared to the ideal gas equation as follows:

$$T_r(x) = \frac{(T_{hot} - T_{cold})}{L_r}x + T_{cold} \quad (2.5)$$

$$m_r = \int_0^{V_r} \rho dV = \int_0^{L_r} \frac{p}{RT_r(x)} A_r dx = \frac{pV}{RT_{eff}} \quad (2.6)$$

$$T_{eff} = \frac{(T_{hot} - T_{cold})}{\ln\left(\frac{T_{hot}}{T_{cold}}\right)} \quad (2.7)$$

The pressure equation can then be rewritten as follows:

$$p = \frac{MR}{V_{hot}/T_{hot} + V_r \ln\left(\frac{T_{hot}}{T_{cold}}\right) / (T_{hot} - T_{cold}) + V_{cold}/T_{cold}} \quad (2.8)$$

Although there is no analytical solution to find the work done per cycle, it can be solved by a Fourier series expansion of the pressure term as done by Urieli and Berchowitz (1984).

### **Finkelstein model (ideal adiabatic model)**

Since the compression and expansion processes are sometimes better approximated as adiabatic instead of isothermal, the Finkelstein model was devised. Although most of the assumptions are the same as for the Schmidt model, the temperatures in the compression and expansion spaces have to be solved. This requires the conservation of mass equation, the conservation of energy equation and an equation

of state. The adiabatic model is assumed to be a better assumption for all except miniature engines, and especially for large engines running at high frequencies (Chen and Griffin, 1983).

The Schmidt model, however, is easily solved compared to the Finkelstein model. The Schmidt model produces an equation for the pressure at any point during the cycle, whereas the Finkelstein model only produces an expression for  $dp/dt$ , which also contains conditional temperature terms that depend on the direction of flow. Since pressure needs to be solved by numerical integration, it is no longer a closed-form solution.

### 2.2.2 Second-order analysis

Second-order methods start with cycle analysis and individual loss mechanisms are then identified. The cycle analysis predicts power and efficiency and the loss terms are used to adjust these. The common cycle to use is either the Schmidt model or the Finkelstein model. Semi-adiabatic cycles have also been used, most notable by Philips (Martini, 1983).

By identifying these loss terms individually, it is easier to identify where improvements can be made. Mechanisms for power loss include (Martini, 1983): flow friction, mechanical friction, reheat loss due to an ineffective regenerator, gas and solid conduction, and conduction through the regenerator matrix.

Although second-order methods provide an uncomplicated method of design optimisation, they were developed for the kinematic Stirling engine where the phase is known. Second-order methods have to be expanded for FPSEs in order to solve for the piston and displacer motions.

### 2.2.3 Third-order analysis

The fact that a Stirling engine works on reversing flow is the largest complicating factor, since flow is always unsteady. As mentioned by Chen and Griffin (1983), third-order methods consist of three basic procedures: 1) to divide the working space into a network of control volumes, 2) to set up the differential equations for conservation of mass, momentum and energy and also an equation of state for the working fluid, and 3) to solve simultaneously the system of difference equations by some adequate numerical method.

Terms for heat transfer and flow friction have been the challenging areas, as mentioned by Urieli (1977). The third-order computer simulation presented by Urieli (1977) replaced the Fanning friction factor for flow friction with the Reynolds friction factor to avoid the problem of not conserving a pressure drop when flow is reversed.

Although third-order analysis is generally the most involved method, it has the biggest potential for providing accurate results and can capture start-up characteristics. The differential equations can also be simplified by certain assumptions, such as neglecting the kinetic energy of the working fluid. The major drawback

of third-order methods is that insight into design improvements is largely lost and can only be determined by a parametric study, i.e. parameters have to be changed and the simulation is then executed for each situation.

#### 2.2.4 Dynamic analysis

All the methods mentioned above deal only with the thermodynamics of the engine, since the piston and displacer motions are taken as known parameters. In an FPSE, the piston and displacer are uncoupled and the motion of each has to be solved. Dynamic analysis is a means of determining piston and displacer motions by considering the piston and displacer as a dynamic system of masses, dampers and springs.

The general form of the equations of motion is as follows (Kankam and Rauch, 1991):

$$[M][\ddot{X}] + [C][\dot{X}] + [K][X] = [F(t)] \quad (2.9)$$

Here  $[M]$ ,  $[C]$  and  $[K]$  refer to matrices for the system masses, damping coefficients and stiffness coefficients. A typical application will look as follows (see Figure 2.4):

$$m_p \ddot{x}_p + C_p \dot{x}_p + C_{pd}(\dot{x}_p - \dot{x}_d) + k_p x_p = (p_{bounce} - p_c)A_p - F_{load} \quad (2.10)$$

$$m_d \ddot{x}_d + C_d \dot{x}_d + C_{pd}(\dot{x}_d - \dot{x}_p) + k_d x_d = p_c A_c - p_e A_e + p_{bounce} A_{rod} \quad (2.11)$$

As can be seen, the time-dependent force terms depend on the pressure in the working space as well as the load, such as an electric generator. Assuming that the characteristic of the electric generator is known, an expression must be determined for the pressures.

This is where the different approaches to dynamic analysis can be seen. Although there are many different approaches, such as linear harmonic analysis (LHA) and control-based design, they always require simplifying assumptions. The

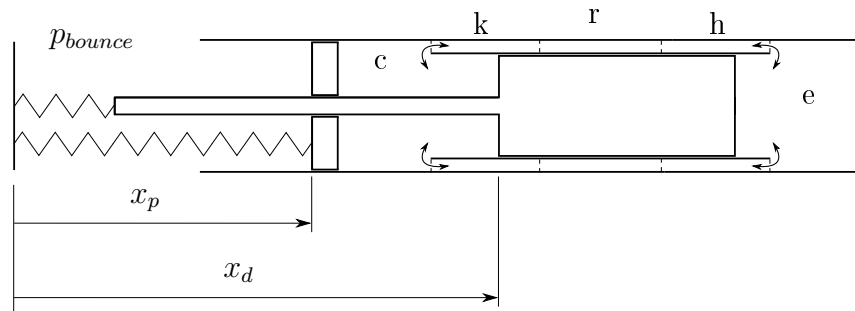


Figure 2.4: Dynamic analysis.

LHA presented by Chen and Griffin (1986) assumes sinusoidal functions for periodic variables, where the control-based design presented by Riofrio *et al.* (2008) uses the Schmidt model to determine pressure fluctuations.

In order to avoid the need for simplifying assumptions, it is possible to determine the pressure throughout the engine by means of a third-order approach, i.e. the working space is divided into a number of control volumes and the pressure is determined numerically. The theoretical simulation presented in this study makes use of this approach because of its ability to be expanded into a fully descriptive model that can be used for the design and optimisation of the engine. Although there are drawbacks to a third-order method as mentioned, it has the ability to be the most powerful simulation method.

## 2.3 Stirling engine configurations

Throughout the history of Stirling engine development, three configurations have emerged that each have a distinct method of achieving the compression and expansion of the working fluid. All of these configurations are the same in the sense that they all contain a minimum of two moving parts. The three configurations are known as the alpha, beta and gamma configurations (see Figure 2.5). As for kinematic Stirling engines, FPSEs can also take any of these configurations. Each configuration has design, manufacture and performance implications, which will now be discussed. Refer to Section 2.5.2 (page 20) for an explanation of gas bearings and flexure bearings.

### 2.3.1 Alpha configuration

The alpha configuration has its main advantage in its modular nature, which means that any part of the engine can be altered independently. The alpha configuration is different to the other configurations since it has two power pistons and no displacer. The pistons are independent of one another and no relative centring is required between them.

Another advantage of this configuration is that the working fluid only has to move backwards and forwards and does not have to move around corners or bends. Centring can be achieved by either gas bearings, flexure bearings or a combination of these.

The major downfall of this configuration, however, is that one of the pistons runs along a very hot cylinder. The differential expansion of the piston and the cylinder must be designed very carefully, as well as the linking mechanism that attaches to the hot piston. It also is not easily possible to operate two alpha configurations in a horizontally opposed manner to minimise vibrations.

Although it is technically possible to operate the alpha configuration as an FPSE, very few are encountered in the literature.

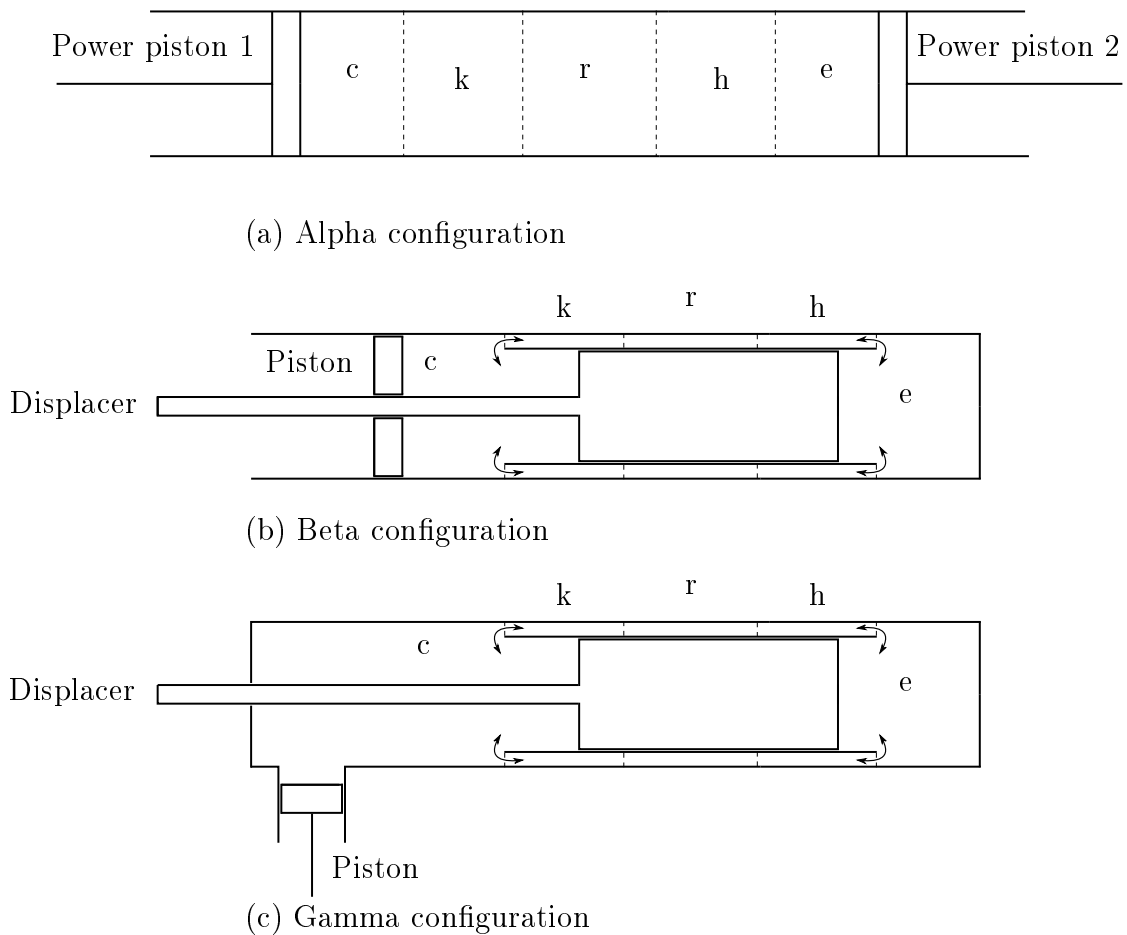


**Figure 2.5:** Stirling engine configurations. (a) Alpha configuration, (b) Beta configuration, (c) Gamma configuration.

### 2.3.2 Beta configuration

The beta configuration comprises a piston and displacer in the same cylinder. The displacer rod runs from the working space through the piston centre to what is termed the bounce space. This piston rod is there to achieve a differential area across the displacer in the working space so that a net force is always generated on the displacer in the working space.

The beta configuration allows both the piston and displacer to have their sealing surfaces on the cold side of the engine and does not have to be concerned with differential expansion of mating surfaces.

The major disadvantage, however, is that of achieving centring. The piston can be centred by gas bearings, flexure bearings or a combination of these. The difficulty, however, is with the displacer. Firstly, the displacer has to be aligned



with the piston and, secondly, it has to be aligned with the cylinder as well. Furthermore, the displacer has to be attached to a linear storage device which is usually located in the bounce space. The linear storage device is usually a flexure bearing and thus there are three locations that need to be aligned relative to one another.

It is also only possible to use flexure bearings in the bounce space. Gas bearings have to be used at the annuli between the piston and displacer rod and the displacer and cylinder respectively. The displacer, which separates the compression and expansion spaces, does so by only sealing on a short section of its larger diameter at the cold side of the engine. The diameter of the remaining length of the displacer decreases slightly toward the hot side of the engine to allow a greater tolerance to mitigate the effects of thermal expansion.

The centring difficulty posed by the beta configuration is partly solved by the gamma configuration. The beta configuration has been used extensively by Sunpower Inc. with good performance results and also was the first FPSE to be manufactured. Two beta configuration engines can easily be combined to operate in a horizontally opposed manner to minimise vibrations.

### **2.3.3 Gamma configuration**

The gamma configuration is essentially a beta configuration with the displacer and piston running in separate cylinders. This eliminates the need for centring between the piston and displacer.

The principle of achieving displacer motion remains the same in a beta and gamma configuration. A differential area across the displacer thus is required. A common gamma design, as used by Infinia Corporation, is a post-and-flange design (see Figure 2.6) which allows both the piston and displacer to be supported by flexure bearings only. The presence of the post causes the differential area and will ensure displacer movement when there is a change in working space pressure. However, no leakage must be allowed along the post between the working space and displacer interior.

The achievable stroke of a flexure bearing is dependent on its diameter. A greater diameter allows for a greater stroke. In a gamma configuration, flexure bearings for the displacer are fitted internally and connected to the post. This limits the size of the flexure bearings that can be used, and in turn limits the stroke of the displacer and also the displacement of working fluid between the hot and cold sides of the engine.

Lastly, since there is no overlapping of the piston and displacer motions in the gamma configuration, there is inherently more dead space when compared to the beta configuration.

### **2.3.4 Stirling configuration comparisons**

Cheng and Yang (2012) showed by means of a parametric study that the beta con-

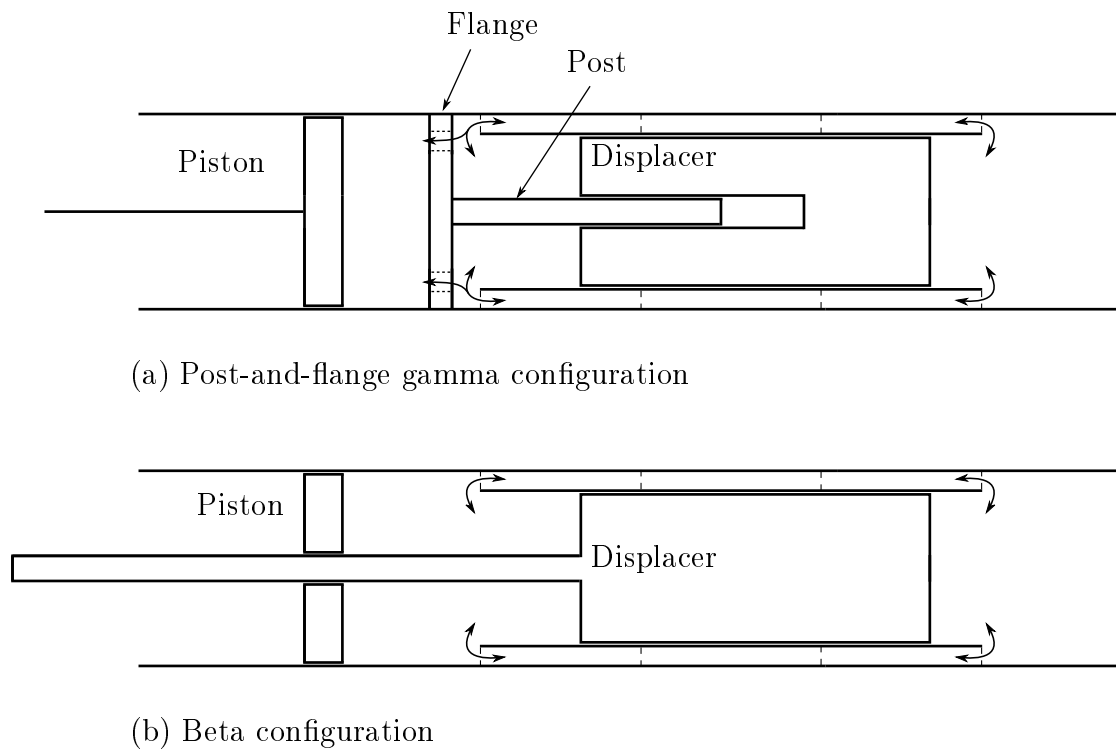


**Figure 2.6:** Comparison of gamma configuration using the post-and-flange design and beta configuration. (a) Post-and-flange gamma configuration, (b) Beta configuration.

figuration produced the highest optimal dimensionless shaft work and the gamma configuration the lowest. The gamma configuration, however, was shown to be most suitable for low-temperature differential operation while the alpha configuration was shown to be especially unsuited.

This agrees with the trend of the Stirling Radioisotope Power System Development at NASA GRC. Initially, the development of the SRG110 (gamma configuration) was supported from 1999 to 2006, when the program was redirected to the ASRG (beta configuration) with the aim of significantly increasing the specific power of the generator (Schreiber and Thieme, 2007). Although the temperature ratio of the ASRG would be larger, it is assumed that the redirection also had to do with the fact that specific power is greater for a beta configuration.

The gamma configurations TDC #13 and TDC #14, for example, each have produced an average output of 65 We at a conversion efficiency of 27%, while the beta configurations ASC-0 #3 and ASC-0 #4 have each produced an average output of 75 We at a conversion efficiency of 29% (Orti, 2012). Both of these

units have been operated between the same temperature extremes.

The alpha configuration is not considered due to the fact that one of the pistons has to seal along a hot cylinder wall, as well as due to the difficulty of generating a horizontally opposed configuration. The necessity of having the possibility of a horizontally opposed configuration is due to the fact that vibrations can be minimised. This is especially important as the mass of particularly the piston increases.

The 25 kWe gamma configuration, horizontally opposed Stirling engine (SPDE) developed by MTI under NASA contract NAS3-23883 produced a casing motion amplitude of 0,03 mm while producing 25 kW piston PV power (Dochat, 1993). This was achieved with a piston mass of 9,967 kg at a frequency of 99 Hz.

It was these considerations that led to the choice of a beta configuration design for this study.

## **2.4 Performance parameters**

This section highlights some of the factors that affect the performance of Stirling engines. The optimisation of Stirling engines is a complicated operation, however, because of the interrelation of parameters.

There are certain parameters, however, that are monotonic with respect to performance (Cheng and Yang, 2012). These include average working space pressure, dead volume and temperature ratio. The performance of a Stirling engine thus can be improved directly without resorting to complicated optimisation.

### **2.4.1 Operating pressure**

Consider again the simplified equation describing the pressure of the working space given by the Schmidt model (Equation 2.4). If an engine operates at a larger working space pressure, there is a larger mass of working fluid in the working space. If it is assumed that the temperature and volume extremes remain the same, the pressure variation in the cycle will be larger and hence the work integral will be larger.

### **2.4.2 Dead space**

In a cycle it is assumed that all working fluid goes through the same process, be it in an internal combustion engine where the working fluid experiences the same process at the same time or in a Rankine cycle where each part of the working fluid undergoes a different process at a certain time but every part of the working fluid eventually goes through the same set of processes.

This is not the case in a Stirling engine, however. There is always some working fluid that will never leave the hot side of the engine and likewise on the cold side of the engine.

Dead space refers to the spaces that exist in the machine that allow part of the working fluid to be at a different state than what the cycle stipulates, in this

case referring to the ideal Stirling cycle. When the ideal Stirling cycle stipulates that the working fluid must be at  $T_{hot}$ , then any space below  $T_{hot}$  is regarded as dead space. The regenerator will always be noted as dead space since its effective temperature is different from the hot space temperature (when all working fluid should be there), and likewise for the cold space temperature. The other forms of dead space are the heater and cooler and even the compression and expansion spaces.

Dead space has a degrading effect on work done per cycle. Consider the following integral:

$$W = \oint pdV \quad (2.12)$$

Substituting the pressure relation given by the Schmidt model (Equation 2.3) we get:

$$W = \oint \left[ \frac{MR}{V_e/T_e + V_h/T_h + V_r/T_r + V_k/T_k + V_c/T_c} \right] dV \quad (2.13)$$

Assuming the compression and expansion space volumes are sinusoids, which are always positive, and that temperatures are constant (isothermal assumption), the work integral can also be expressed as:

$$W = MR \int_0^{2\pi} \left[ \frac{1}{k_e \sin(\theta + \alpha_e) + k_c \sin(\theta + \alpha_c) + k_d} \right] d\theta \quad (2.14)$$

The dead space now essentially is represented by  $k_d$ . If  $k_d$  is increased, the variation of the pressure function will decrease, which in turn decreases the magnitude of the work integral. The opposite is true if  $k_d$  is decreased.

Dead space thus always wants to be kept to a minimum, but has a negative effect on other design characteristics. To decrease dead space one can shorten the engine, which means that the hot side and cold side are less isolated from one another and that the regenerator, heater and cooler will be less effective. This is where more advanced optimisation is required.

### 2.4.3 Temperature ratio

Although efficiency is dependent on temperature ratio, work done per cycle also increases in a similar manner to increasing the working space pressure. If  $T_{hot}$  is increased, for example, then the pressure variation per cycle will be greater, and also the work integral per cycle if the volume variation remains the same.

## 2.5 Physical considerations

Apart from many advantages, FPSEs have their own set of physical challenges. This section identifies and discusses the most unique and important challenges to overcome in the design of an FPSE.

### 2.5.1 Close tolerance sealing

It is essential for any Stirling engine to achieve good sealing of the working fluid and thus a very small tolerance has to be maintained between parts.

Since there are no side forces on the piston in an FPSE, a close tolerance fit of the piston and cylinder is all that is needed to create a seal. This includes the displacer rod running inside the piston for a beta configuration.

Since FPSEs do away with the need for lubrication, any piston runs linearly inside its cylinder without touching the walls. In more common terms, FPSEs run dry and any contact between the piston and cylinder wall is unwanted, since the fine tolerances required for sealing can be damaged from abrasion and eventually can lead to seizing, especially at high speeds. Centring thus is immensely important to allow good sealing, as well as to prohibit any contact between the piston and cylinder.

### 2.5.2 Centring

Gas bearings allow a piston to ‘float’ inside a cylinder by creating an air pocket around the piston. Gas bearings used for the ASC-E2 convertors, for example, can withstand a lateral acceleration of three times the gravitational acceleration before contact occurs (Meer and Oriti, 2012).

Gas bearings work on the principle of air flow between a high-pressure and a low-pressure plenum. Gas flows from the high- to the low-pressure plenum along the side of the piston (see Figure 2.7). This high-pressure plenum is either internally charged or externally charged. Externally charged gas bearings require an additional pump, which will require a design life similar to that of the rest of the engine and will also add moving parts to the engine (Dhar, 1999*a*).

The 25 kWe CTPC FPSE (Dhar, 1999*a*) made use of internally charged bearings because of this limitation. Internally charged bearings have their own set of challenges, however, and also limit the life of an engine. The charging pressure created in the high-pressure plenums of internally charged bearings is generated while the engine is in operation. The engine thus needs a couple of cycles before the gas bearings operate normally and hence they initially run dry. The CTPC designers thus had to do tests to find suitable wear-pairing materials to minimise this effect on engine life (Dhar, 1999*b*). Furthermore, internally charged gas bearings require increased fabrication complexity for porting holes, plenums and so forth.

Flexure bearings, as shown in Figure 2.8, will always ensure good centring, since they are designed to have high stiffness in the radial direction. The main advantage of flexure bearings is that they always provide bearing support and thus

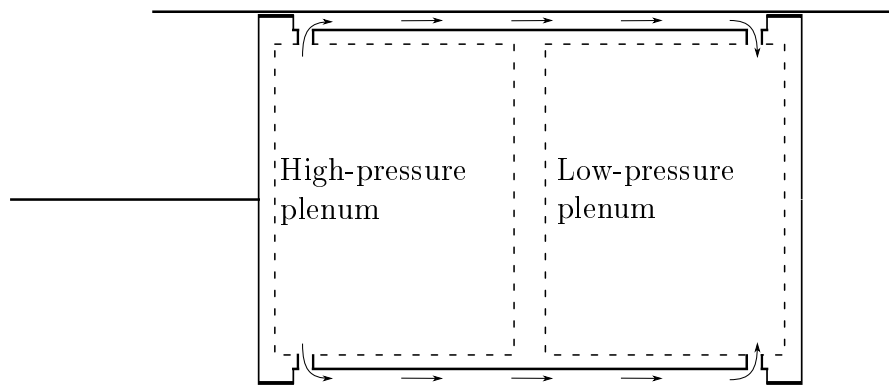


**Figure 2.7:** Air flow in a typical gas bearing.

there never is contact between the piston and the cylinder. If a piston is supported by two flexure bearings with the head of the piston overhanging, however, the piston could assume a mode of vibration and make contact with the cylinder wall. This, however, is not the case with a gas bearing that opposes any motion of the piston toward the cylinder wall.

A flexure bearing also acts as a spring in the axial direction and provides the restoring force required for the piston and displacer. This provides a neat and reasonably uncomplicated design.

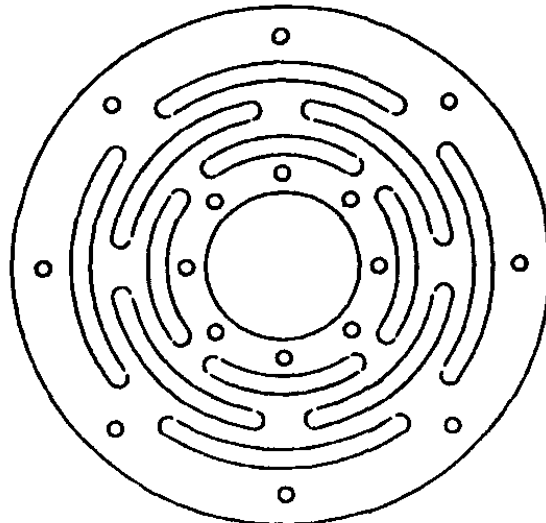


**Figure 2.8:** Standard shaker (Peckham Engineering and Tool, 1994).

### 2.5.3 Piston and displacer restoring force

The Stirling engine is an axially reciprocating engine and, unlike a turbine-type engine, the compression and expansion processes happen sequentially and discretely rather than simultaneously and continuously. This requires some of the expansion work to be stored and used for compressing the working fluid.

For an FPSE, a restoring force is needed for both the piston and displacer. The three most common methods of achieving this restoring force are by means of a gas spring, a flexure bearing or a compression spring (see Figure 2.9).

Gas springs provide a simple solution for the restoring force, but also require alignment to ensure a close tolerance fit to seal the gas. Gas bearings also suffer from hysteresis losses. When the gas is compressed it is accompanied by an increase in temperature, which causes irrecoverable heat transfer to the wall of the cylinder.

Flexure bearings provide the added advantage of centring, as mentioned, and thus provides a two-in-one solution. Flexure bearings are not readily available off the shelf, however, and most flexure bearings suffer from axial twist when flexing. Symmetrical designs such as the standard shaker (see Figure 2.8) do away with this problem.

A compression spring has the advantage of a large stroke given enough space in the linear direction, but has no centring effect. Additional space in the linear direction is preferred above space in the radial direction since, for a given operating

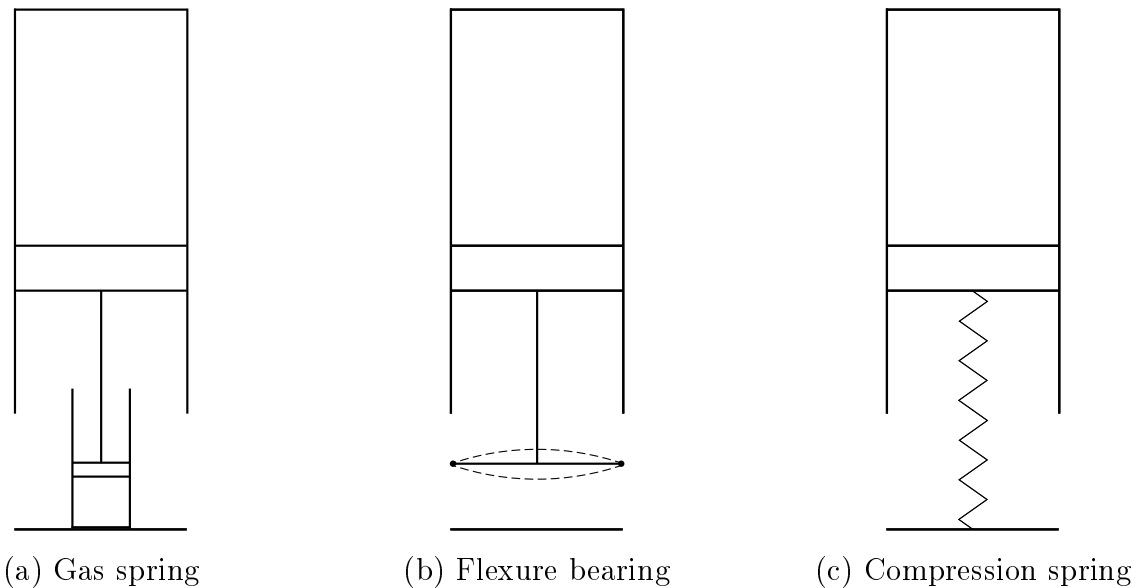


**Figure 2.9:** Three common methods of achieving a restoring force. (a) Gas spring, (b) Flexure bearing, (c) Compression spring.

pressure, the required wall thickness of a pressure vessel increases with diameter.



## 3 Theoretical simulation model

### 3.1 Introduction

This chapter describes the theoretical simulation model in detail. The theoretical simulation model is described prior to the design of the engine because the theoretical simulation model forms part of the chapter on design (Chapter 4).

The theoretical simulation presented in this study is a combination of a third-order and dynamic analysis. This provides the ability for it be expanded into a fully descriptive model that can be used for design and optimisation of the engine.

The first section describes how the piston and displacer motions were determined, as well as how contact events were handled. The cell and nodal networks are then explained, along with the solution of the system equations. A section is also used to describe the sequence of events and where the relevant equations were used. A discussion on how initialisation was done is then presented and the final section addresses more specific details with regard to programming language, simulation time and sample calculations.

The suitability of the theoretical simulation model was determined by comparing it to experimental test results, this comparison is provided in the final section.

### 3.2 Piston and displacer motion

The piston and displacer motions were solved by applying Newton's second law of motion to determine acceleration, which is integrated over the time step to obtain the new velocity and displacement.

The free body diagrams for the piston and displacer are shown in Figure 3.1. Forces on the piston include pressure forces from the compression space ( $p_c$ ) and bounce space ( $p_{bounce}$ ), which in this case is atmospheric pressure. The force from the compression spring is represented by  $Fk_p$  and that of the load by  $F_{load}$ , which in this case is from the electric generator. Frictional forces occur between the piston and sleeve ( $Ff_p$ ) and between the piston and displacer ( $Ff_{pd}$ ) because of their relative motion.

Forces on the displacer include pressure forces from the compression space ( $p_c$ ) and expansion space ( $p_e$ ), as well as from the bounce space ( $p_{bounce}$ ). The force from the compression spring is represented by  $Fk_d$ . Skin drag due to air in the annulus around the displacer, as well as the form drag of the displacer, are represented by  $Ff_d$ , and the same frictional force between the piston and displacer is again represented by  $Ff_{pd}$  but defined in the opposite direction.

The sum of the forces on the piston and on the displacer can thus be expressed as follows:

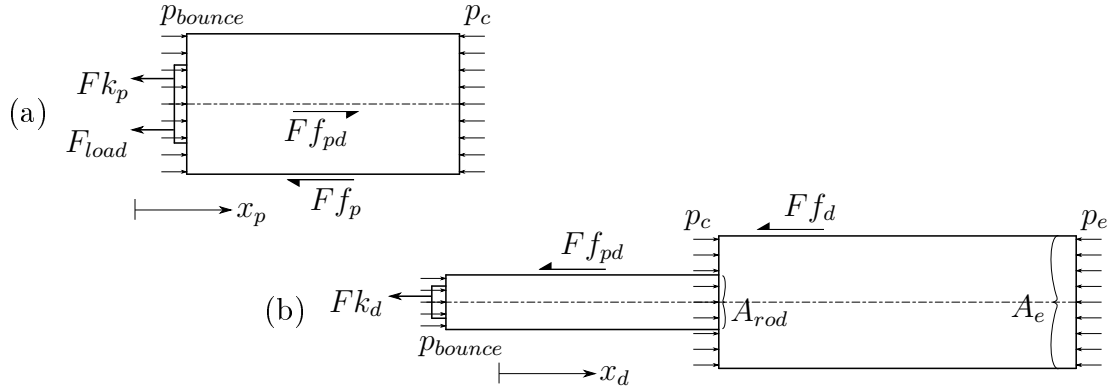


**Figure 3.1:** Free body diagrams. (a) Piston, (b) Displacer.

$$\sum F_p = (p_{bounce} - p_c)A_p - Fk_p - Ff_p - F_{load} + Ff_{pd} \quad (3.1)$$

$$\sum F_d = p_c(A_e - A_{rod}) - p_e A_e + p_{bounce}A_{rod} - Fk_d - Ff_d - Ff_{pd} \quad (3.2)$$

The acceleration of the piston and the displacer can then be expressed as:

$$\sum F_p = m_p \left( \frac{d^2 x_p}{dt^2} \right) \quad (3.3)$$

$$\sum F_d = m_d \left( \frac{d^2 x_d}{dt^2} \right) \quad (3.4)$$

In this case, however, certain simplifying assumptions are made. Firstly, the experimental test data used as comparison was that of a test done prior to the addition of the electric generator, thus  $F_{load} = 0$ . Furthermore, all frictional and dissipative forces were assumed to be zero, namely  $Ff_p$ ,  $Ff_d$  and  $Ff_{pd}$ . These frictional forces were neglected since there were no side forces on the piston or displacer. The spring forces were calculated as follows, with the measured values given in Appendix A:

$$Fk_p = k_p(x_p - x_{p0}) \quad (3.5)$$

$$Fk_d = k_d(x_d - x_{d0}) \quad (3.6)$$

With both the piston and displacer accelerations known and assumed to be constant, they can be integrated over the time step to determine the new velocity and displacement of the piston and the displacer, as follows:

$$v_p^{t+\Delta t} = v_p^t + \Delta t \left( \frac{d^2 x_p}{dt^2} \right)^t \quad (3.7)$$

$$v_d^{t+\Delta t} = v_d^t + \Delta t \left( \frac{d^2 x_d}{dt^2} \right)^t \quad (3.8)$$

$$x_p^{t+\Delta t} = x_p^t + (\Delta t) v_p^t + \frac{(\Delta t)^2}{2} \left( \frac{d^2 x_p}{dt^2} \right)^t \quad (3.9)$$

$$x_d^{t+\Delta t} = x_d^t + (\Delta t) v_d^t + \frac{(\Delta t)^2}{2} \left( \frac{d^2 x_d}{dt^2} \right)^t \quad (3.10)$$

Since the acceleration was different at each time step, this procedure had to be repeated for each time step. Before the velocity of the new time step could be calculated, however, a verification of contact between the piston and displacer had to be done and the relevant velocities had to be altered before proceeding to the next time step.

It was assumed that if there was contact between the piston and displacer, it would be elastic. In a linear elastic collision, momentum and kinetic energy of the system is conserved.

Momentum of the system:

$$m_p v_p^{old} + m_d v_d^{old} = m_p v_p^{new} + m_d v_d^{new} \quad (3.11)$$

Kinetic energy of the system:

$$\left( \frac{1}{2} m_p v_p^2 \right)^{old} + \left( \frac{1}{2} m_d v_d^2 \right)^{old} = \left( \frac{1}{2} m_p v_p^2 \right)^{new} + \left( \frac{1}{2} m_d v_d^2 \right)^{new} \quad (3.12)$$

The velocities after the collision can, therefore, be determined by solving Equations 3.11 and 3.12 simultaneously:

if  $(x_c < 0,001)$  &  $(v_c < 0)$ :

$$v_d^{new} = \frac{v_d^{old}(m_d - m_p) + 2m_p v_p^{old}}{m_d + m_p} \quad (3.13)$$

$$v_p^{new} = \frac{v_p^{old}(m_p - m_d) + 2m_d v_d^{old}}{m_d + m_p} \quad (3.14)$$

The distance between the front face of the piston and the rear face of the displacer is given by  $x_c$  and the accompanying velocity is represented by  $v_c$ . Collision is specified as when the piston and displacer are closer than 1 mm from each other, in order to avoid negative volumes. After collision it is possible that  $x_c$  could still

be less than 1 mm, hence a velocity check ( $v_c < 0$ ) has to be done to determine whether the given state was prior or subsequent to collision. This contact event was assumed to be elastic partly by inspection and partly since there is a rubber ring spacer around the displacer rod, which is assumed to cause an elastic contact event. The rubber spacer serves to prevent the faces of the piston and displacer making direct contact.

The other possibility for collision is between the displacer and the heater head end cap. This collision is assumed to be inelastic, since two hard metal faces are colliding:

if ( $x_e < 0,001$ ) & ( $v_e < 0$ ):

$$v_d = 0 \tag{3.15}$$

Here  $x_e$  represents the distance between the front face of the displacer and the heater head end cap, with the accompanying velocity represented by  $v_e$ . The condition for collision is again taken as less than 1 mm proximity of the faces. The collision is assumed to be inelastic and hence  $v_d$  is set to zero. Only the displacer is involved here, hence  $v_p$  remains unchanged.

### 3.3 Cell and nodal network

The theoretical model consists of a stationary one-dimensional network of cells and nodes as shown in Figure 3.2 (also see Figure 3.3). Cells are defined as control volumes that contain mass and where temperature and pressure are defined. Nodes are defined as the boundaries between cells and serve to define mass flow into and out of the cell.

A cell network and nodal network were defined for both the wall and the working space. The cells in the wall network are labelled from  $j = 1$  to  $j = N_{wall}$ . The cooler section of the engine is assumed to be a lumped mass ( $j = N_{wall}$ ) and all other cells were set to a width of 1 mm. The cells in the working space network are labelled from  $i = 1$  to  $i = N_{cell}$ . The compression space ( $i = 1$ ) and the expansion space ( $i = N_{cell}$ ) were taken as one cell each, with the intermediate cells all set to a width of 1 mm. These working space cells were placed directly opposite the wall cells to simplify the heat transfer calculation ( $dQ_i/dt$ ) between the wall and the working space.

The determination of the temperatures in the wall cells is discussed in Section 3.6 (page 34). The temperatures in the wall cells ( $j = 1$  to  $j = N_{wall}$ ) were assumed to remain constant and heat transfer between the wall cells was, therefore, not calculated. The working space nodes, are labelled from  $n_1$  to  $n_{N_{cell}+1}$ .

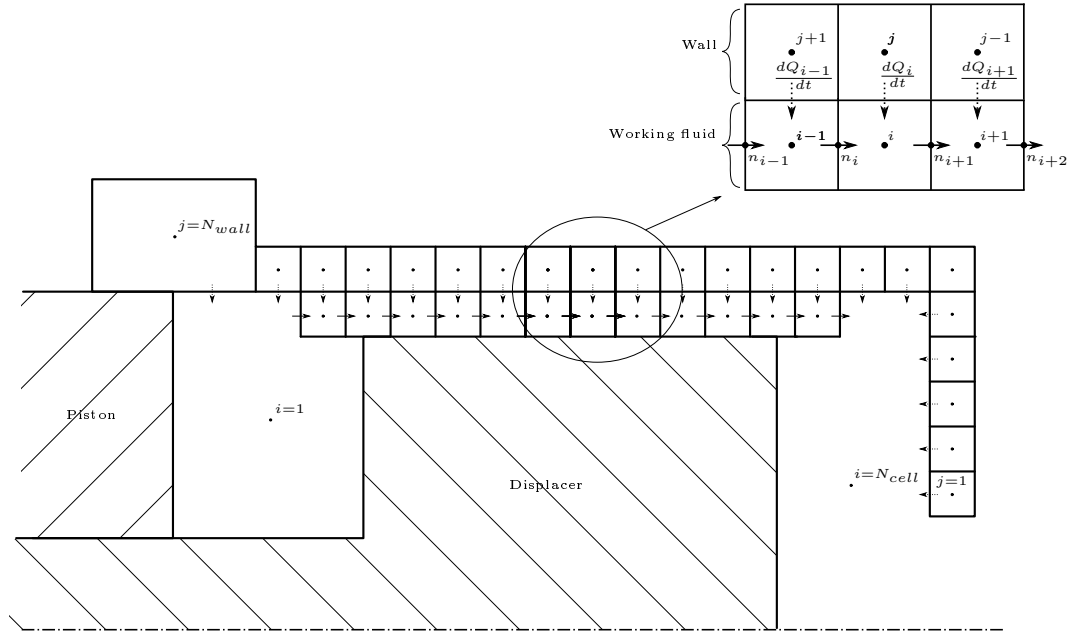


**Figure 3.2:** Cell and nodal networks.

### 3.4 Solution of system equations

An illustration of the properties in a cell and at the nodes is shown in Figure 3.3. As shown, heat transfer only occurred between the wall cell and the adjacent working space cell ( $dQ_i/dt$ ). It should also be noted that the wall cells and the working space cells run in opposite directions, thus indexing is done to select the correct pair of wall and working space cells.

If the ideal gas equation is differentiated with respect to time and rearranged, the rate of change of mass of the cell can be represented as follows:

$$\frac{\partial m_i}{\partial t} = m_i \left( \frac{1}{p_i} \frac{\partial p_i}{\partial t} + \frac{1}{V_i} \frac{\partial V_i}{\partial t} - \frac{1}{T_i} \frac{\partial T_i}{\partial t} \right) \quad (3.16)$$

The assumption that no leakage of the working fluid occurs can be mathematically expressed as follows:

$$\sum_{i=1}^{N_{cell}} \frac{\partial m_i}{\partial t} = 0 \quad (3.17)$$

Pressure is assumed to be equal throughout the working space and Equation 3.17 can be substituted into Equation 3.16 to produce the rate of change of pressure in the working space (note that the subscript is now dropped from the pressure term):

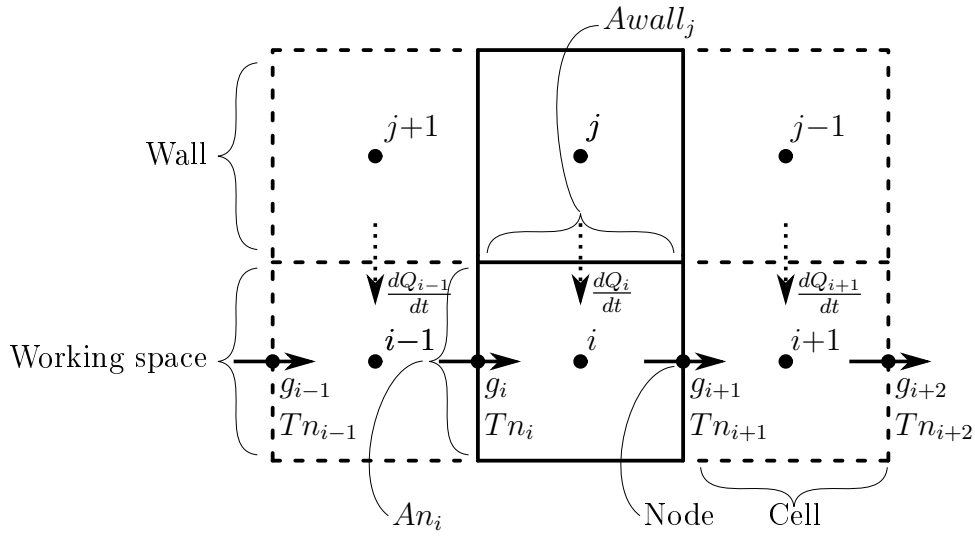


**Figure 3.3:** Cell and node interaction.

$$\frac{\partial p}{\partial t} = p \cdot \left[ \frac{\sum_{i=1}^{N_{cell}} m_i \left( -\frac{1}{V_i} \frac{\partial V_i}{\partial t} + \frac{1}{T_i} \frac{\partial T_i}{\partial t} \right)}{\sum_{i=1}^{N_{cell}} m_i} \right] \quad (3.18)$$

Assuming that pressure is equal throughout the working space greatly reduces the simulation time. In this case, the simulation time step was reduced by a factor of 1 000 (see Section 3.7, page 36). This is equivalent to not applying the conservation of momentum equation for the working fluid, as is explained in Appendix B. Although this assumption was not experimentally tested, Saturno (1994) predicted by theoretical simulation for similar conditions, a maximum pressure drop of about 35 Pa between the compression and expansion spaces for the Beale B-10B demonstrator engine. This was at a hot side temperature of 405 K and a cold side temperature of 300 K. This suggests that the pressure drop between the compression and expansion spaces is negligible if we consider the 50 kPa working space pressure variation seen in the experimental tests. This small pressure drop is expected since there are no complicated heat exchangers that would cause a large flow resistance.

Experimentally verifying this assumption is possible but an additional pressure sensor is needed at the hot side of the engine. Most pressure sensors have a relatively low maximum operating temperature, however.

In order to determine the rate of change of pressure of the working space, the rate of change of volume ( $\partial V_i/\partial t$ ) and the rate of change of temperature ( $\partial T_i/\partial t$ )

first needed to be determined for all working space cells. The rate of change of volume was confined to the compression space and expansion space, since the intermediate cells do not change volume. The rate of change of volume of each can be expressed as follows:

$$\frac{\partial V_c}{\partial t} = (-v_p + v_d)(A_e - A_{rod}) - v_p A_{annul} \quad (3.19)$$

$$\frac{\partial V_e}{\partial t} = -v_d A_e \quad (3.20)$$

Here,  $A_{annul}$  refers to the cross-sectional area of the annulus between the displacer and the cylinder. To determine the rate of change of temperature, the conservation of energy equation was used (see Appendix B):

$$\frac{\partial T_i}{\partial t} = \frac{T_i}{m_i} (An_{i+1}g_{i+1} - An_i g_i) + \frac{1}{m_i c_{v_i}} \left[ \frac{dQ_i}{dt} - \frac{dW_i}{dt} + c_{p_i} (An_i T n_i g_i - An_{i+1} T n_{i+1} g_{i+1}) \right] \quad (3.21)$$

At the nodes,  $g$ ,  $Tn$  and  $An$  represent the mass flux, upstream cell temperature and cross-sectional area respectively. The upstream cell temperature is a conditional temperature and is taken as the upstream cell temperature of its nearest neighbour, as follows:

if  $g_i \geq 0$ :

$$Tn_i = T_{i-1} \quad (3.22)$$

if  $g_i < 0$ :

$$Tn_i = T_i \quad (3.23)$$

Since volume change only occurs at the compression and expansion spaces, work also only occurs here:

$$\frac{dW_c}{dt} = p \left( \frac{\partial V_c}{\partial t} \right) \quad (3.24)$$

$$\frac{dW_e}{dt} = p \left( \frac{\partial V_e}{\partial t} \right) \quad (3.25)$$

Heat transfer to the cell is only considered from the adjacent wall cell, with heat transfer from the displacer wall neglected. As depicted in Figure 3.3, the heat transfer to the cell is expressed as follows:

$$\frac{dQ_i}{dt} = h_i A_{wall_i} (T_{wall_j} - T_i) \quad (3.26)$$

With:

$$h_i = \frac{Nu_i k_i}{D_h} \quad (3.27)$$

The heat transfer area between the wall and the working space cells is given by  $A_{wall_j}$  and the temperature of the adjacent wall cell is given as  $T_{wall_j}$ .

In order to obtain the heat transfer from the wall, the Nusselt number had to be determined. The size of the annulus indicated that the flow in the annulus could be approximated by flow between two parallel plates, since the ratio of the annulus inner diameter to the annulus outer diameter is near unity:

$$D_i/D_o = 0,944 \approx 1 \quad (3.28)$$

A smaller annulus thus provides a smaller hydraulic diameter (1,98 mm for the presented engine), which in turn provides a smaller Reynolds number and tends to confine flow to be laminar ( $Re < 2\,300$  (Çengel, 2006)):

$$Re = \frac{\rho \cdot v \cdot D_h}{\mu} \quad (3.29)$$

For fully developed laminar flow, the Nusselt number is constant. For flow between two parallel plates, with the inner wall insulated and the outer wall isothermal, the Nusselt number at the outer wall becomes (Mills and Ganesan, 2013):

$$Nu = 4,861 \quad (3.30)$$

In Stirling engines, however, the flow reverses many times a second and thus is never steady, which brings the assumption of fully developed flow into question. Furthermore, both the hydraulic and thermal boundary layer development need to be considered. This analysis is complicated, however, and not justified for a one-dimensional model. The Nusselt number was thus set as an independent variable to gain insight in this regard and also became a parameter for sensitivity analysis.

The Nusselt numbers used were taken as applicable throughout the engine and no local Nusselt numbers were defined. Turbulent flow was not considered, since it was found that the Reynolds numbers were always below 2 300.

Values for  $c_p$  were interpolated linearly from property tables for air at 101,325 kPa (Çengel, 2006). Values for  $c_v$ , in turn, were calculated from its ideal gas relationship with the specific gas constant:

$$c_v = c_p - R \quad (3.31)$$

Since  $\partial V_i/\partial t$  and  $\partial T_i/\partial t$  were now known,  $\partial p/\partial t$  could be determined by Equation 3.18, and then  $\partial m_i/\partial t$  could be determined from Equation 3.16.

All the rates of change were known by this point. The new pressure and mass were then calculated by Euler method integration for each cell, with the the new temperature determined by the ideal gas equation:



$$m_i^{t+\Delta t} = m_i^t + \Delta t \left( \frac{\partial m_i}{\partial t} \right)^t \quad (3.32)$$

$$p^{t+\Delta t} = p^t + \Delta t \left( \frac{\partial p}{\partial t} \right)^t \quad (3.33)$$

$$T_i = \frac{pV_i}{m_i R} \quad (3.34)$$

The new volume could be determined by numerical integration as well, but rather was determined by using the relative position of the piston and displacer with the accompanying areas:

$$V_c^{t+\Delta t} = V_{c0} - x_p^{t+\Delta t} A_p + x_d^{t+\Delta t} (A_e - A_{rod}) \quad (3.35)$$

$$V_e^{t+\Delta t} = V_{e0} - x_d^{t+\Delta t} A_e \quad (3.36)$$

The only variable left to be determined at the following time step was the mass flux at the nodes. Mass flux can be determined by rearranging the conservation of mass equation (see Appendix B):

$$g_i^{t+\Delta t} = \frac{1}{An_i} \left[ An_{i-1} g_{i-1}^{t+\Delta t} - \left( \frac{\partial m_{i-1}}{\partial t} \right)^{t+\Delta t} \right] \quad (3.37)$$

Since the first node was defined as being on the wall, i.e.  $g_1 = 0$ ,  $g_2$  could be calculated. This is also why the indices of the conservation of mass equation were shifted ( $i \rightarrow i - 1$ ):

$$g_2^{t+\Delta t} = \frac{1}{An_2} \left( - \frac{\partial m_1}{\partial t} \right)^{t+\Delta t} \quad (3.38)$$

Mass flux at the remaining nodes could then be determined sequentially. Since  $g_2$  was known,  $g_3$  could be calculated, and then  $g_4$  and so forth.

### 3.5 Program flow

The flow diagram given in Figure 3.4 summarises the sequence of events, which will now be explained.

The simulation parameters include the time step and cell width (1 mm for all cells), while the plotting parameters set the frequency at which values were written to file. The experimental data was imported and the engine parameters were set. The engine parameters included the piston and displacer masses,  $Nu$ , spring constants and so forth. The number of iterations ( $k_{end}$ ) was also included here, since the number of iterations can be set to span a desired number of measured

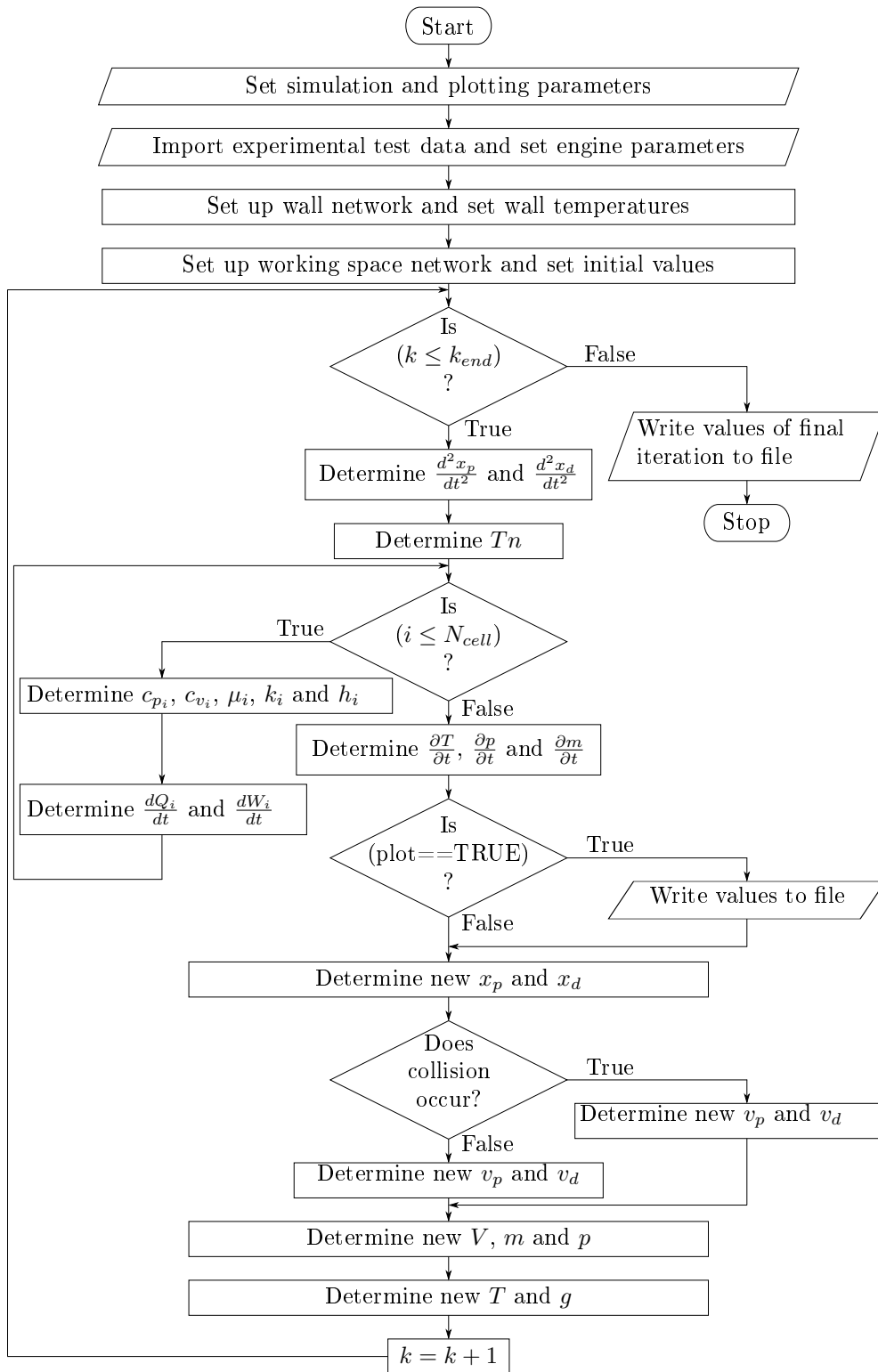


**Figure 3.4:** Theoretical simulation model flow diagram.

cycles that are only known after importing the experimental test data. Each iteration represents a time step, as iterations were used instead of time to simplify debugging.

Setting up the wall network included setting the cell temperatures ( $T_{wall}$ ) and the heat transfer areas ( $A_{wall}$ ). Setting up the working space network included setting up the nodal areas ( $A_n$ ) and initial values of the cells and nodes.

The iteration loop was then entered as  $k$  starts from 1 and ends at  $k_{end}$ . The acceleration of the piston and displacer first were calculated by Equations 3.3 and 3.4 respectively, and the conditional temperatures ( $T_n$ ) subsequently were calculated at all nodes by either Equation 3.22 or Equation 3.23. The temperature-dependent properties ( $c_{p_i}$ ,  $c_{v_i}$ ,  $\mu_i$ ,  $k_i$  and  $h_i$ ), as well as  $dQ_i/dt$  and  $dW_i/dt$ , were then calculated to be used in Equation 3.21. Equation 3.26 was used to determine  $dQ_i/dt$ , and Equations 3.24 and 3.25 were used to calculate  $dW_i/dt$ . The rate of change of temperature was then determined for each cell by Equation 3.21. The rate of change of pressure for the entire working space was determined by Equation 3.18, while the rate of change of mass was determined for each cell by Equation 3.16.

At this point, all the rates of change are known. It then was determined if the desired simulation variables should be written to file or not and, if so, were written to file.

The new piston and displacer positions were then determined by Equations 3.9 and 3.10 respectively and a check for collision was done. The new piston and displacer velocities were then changed accordingly, as discussed in Section 3.2 (page 24). The new volumes, which only changed for the compression and expansion spaces, were determined by means of the new piston and displacer positions (Equations 3.35 and 3.36 respectively), while the new masses and pressure were determined by Euler method integration (Equation 3.32 and 3.33 respectively). The new working space cell temperatures were then determined by the ideal gas law, as shown in Equation 3.34 and, finally, the new mass flux was determined by Equation 3.37.

The simulation then proceeded with the next iteration. This was done until the final iteration was reached, whereupon the final set of desired simulation variables were written to file and the simulation was ended.

### 3.6 Initialising

In order to minimise the settling time of the simulation, initial values were set to the experimental test results at the instance when the displacer reached its maximum displacement. The experimental data thus was imported from this point onward.

The measured values that were used as initial values included  $x_p$ ,  $x_d$  and  $p$ . The initial velocities ( $v_p$  and  $v_d$ ) were determined by fitting a sinusoidal curve to the measured  $x_p$  and  $x_d$  and taking each derivative at this instance. This was done

in favour of a numerical differentiation technique to overcome misrepresentation of the velocity brought on by spikes in the data for  $x_p$  and  $x_d$ . Setting values of  $v_p$  and  $v_d$  to zero did not seem to have a large effect, however, as was done with the simulations discussed in Section 4.6 (page 49).

The temperature of the cells in the working space were set to the temperature of its respective adjacent wall cell. The wall temperature profile was generated by linearly extrapolating the wall temperatures measured ( $T_{wall\_1}$ ,  $T_{wall\_2}$ ,  $T_{wall\_3}$  and  $T_{wall\_4}$ ) between the cooler section of the engine and the start of the heating wire (see Figure 3.5). The wall temperature beyond and including the electrical heating wire was taken as constant.

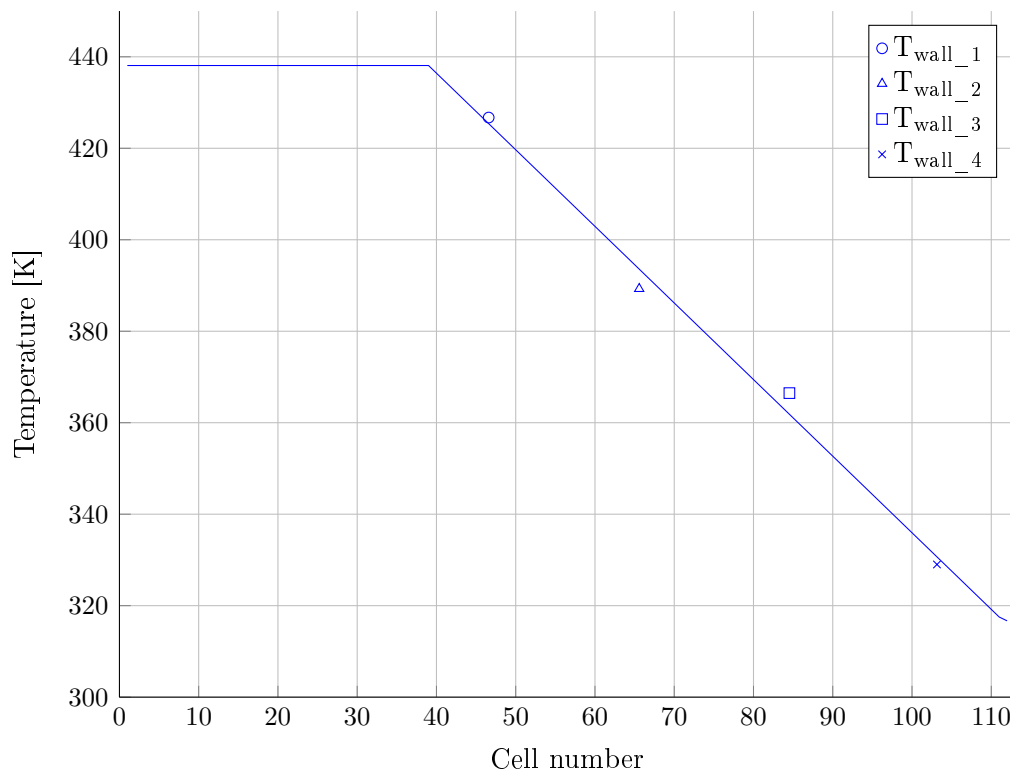


**Figure 3.5:** Extrapolated wall temperature profile.

### 3.7 Software and sample calculations

The code for the model was generated in MATLAB R2010b. MATLAB was used because of its ease of use in terms of developing code, debugging, processing data and generating graphs. MATLAB has a large library of predefined functions to perform operations such as curve fitting, matrix algebra and so forth.

Although the simulation model uses time steps of 0,00001 s, values were only recorded at intervals of 0,001 s. A time step of 0,00001 s was the largest time step that ensured simulation stability. Time steps were altered in factors of 10. Initially, the kinetic energy of the working fluid was included which required a time step of 0,00000001 s which would have increased simulation time by a factor of 1 000.

The simulation time was generally between 40 and 43 minutes for 80 000 iterations (800 ms), which could greatly be reduced by making use of C or FORTRAN.

Sample calculations are provided below for the first 10 iterations. It is not possible to show all variables, so instead, a selection of variables are given. These sample calculations serve as a means of verifying attempts to reproduce the code in an alternative programming language.

The sample calculations provided here, assume  $Nu = 50$ ,  $Cf_p = 6$  N s/m,  $v_p = 0$  and  $v_d = 0$ . The friction coefficient on the piston is given by  $Cf_p$ , which is explained in Section 4.6 (page 49).

The source code is provided in Appendix C.

**Table 3.1:** Sample calculations with  $Nu = 50$ ,  $Cf_p = 6$  N s/m,  $v_p = 0$  and  $v_d = 0$ .

Iteration	$x_p$	$x_d$	$p$	$T_1$
0	0,0896351352	0,0950380689	133686,396403497	316,6804722466
1	0,0896351323	0,0950380672	133686,396403497	316,6804901896
2	0,0896351233	0,0950380621	133686,370537506	316,6804940234
3	0,0896351083	0,0950380535	133686,315578723	316,6804793172
4	0,0896350874	0,0950380415	133686,232276213	316,6804448083
5	0,0896350604	0,0950380261	133686,120589476	316,6803916905
6	0,0896350275	0,0950380072	133685,980550078	316,6803194567
7	0,0896349886	0,0950379849	133685,812227269	316,6802283357
8	0,0896349437	0,0950379592	133685,61565894	316,680118302
9	0,0896348929	0,09503793	133685,390897658	316,6799894008
10	0,089634836	0,0950378975	133685,137989761	316,6798416632

### 3.8 Validation

The experimental test results used for initialising and comparison are from the test without the electric generator (see Chapter 6.2). Further testing of the model by means of changing input parameters was done in Section 4.6 (page 49) and in the sensitivity analysis provided in Appendix D.

It was found that the maximum Reynolds numbers encountered for  $Nu$  equal to 4,861, 20,0 and 50,0 were 1 447, 1 344 and 1 621 respectively, which indicates laminar flow ( $< 2\,300$  (Mills and Ganesan, 2013)).

The choice of 4,861 refers to fully developed laminar flow between two parallel plates where one wall is heated and one wall insulated (Mills and Ganesan, 2013). The other two values for  $Nu$  were set by trial and error as 20 and 50 respectively. Increasing  $Nu$  is equivalent to increasing the heat transfer ability of the engine, i.e. the heat transfer rates between the working space and wall for all cells. Values for  $Nu$  were increased since they are higher for undeveloped flow as opposed to fully developed flow (Kays *et al.*, 2005).

As shown in Figures 3.6, 3.7 and 3.8, the results approximate measured values more accurately with increasing  $Nu$ . This suggests that an isothermal analysis is suitable.

Piston motion is shown in Figure 3.6, where  $Nu = 4,861$  shows erratic behaviour but settles with time. This erratic behaviour is partly because of the collision between the piston and displacer, as explained below. It is evident that the approximation of the piston motion is more accurate with increasing  $Nu$ . Firstly, the stroke amplitude increases with increasing  $Nu$  and, secondly, the frequency increases with increasing  $Nu$ . A summary of the results is given in Table 3.2.

Displacer motion is shown in Figure 3.7. The sharp troughs seen for all  $Nu$  are characteristic of the elastic collision assumption. As the displacer moves down and makes contact with the much heavier piston it simply bounces back upward again. Nonetheless, the effect of the collision can be seen in the piston motion by the slight disruption of the smooth motion. This disruption is most noticeable (especially for  $Nu = 4,861$ ) between 600 and 700 ms. However, the experimental data shows smoother troughs than those produced by the elastic collision assumption.

The shape of the peaks for all  $Nu$  (barring  $Nu = 4,861$ ) is characteristic of the inelastic collision condition. The displacer moves up rapidly, makes contact with the heater head end cap, where the velocity goes to zero momentarily, and the displacer then moves down rapidly. The displacer stroke is also more accurately approximated with increasing  $Nu$ .

The resultant pressure curves are shown in Figure 3.8. Here it is seen that, for  $Nu = 50$ , the pressure approximates the measured values very closely. The pressure is highly influenced by the piston. This is evident when one notices that the jumps in the pressure curves and piston motions (collisions) happen simulta-

neously.

A summary of the results is given in Table 3.2. The wall temperature as extrapolated beyond the heating wire was 438,1 K, while  $T_{hot}$  was measured to be 446,2 K. The temperature of the cooler section was extrapolated as 316,7 K, while  $T_{cold}$  was measured to be 305,4 K. The measured temperatures on the hot and cold sides were compared to the expansion space and compression space temperatures respectively.

It is seen that the highest  $Nu$  provides the most accurate results in almost every aspect, except the phase between the piston and displacer and the indicated power. Although the indicated power increases with increasing  $Nu$ , as expected, the indicated power is overestimated for both  $Nu = 20$  and  $Nu = 50$ . The indicated power should increase since the heat transfer rates between the working fluid and wall increase. The cause of error in the prediction of the phase between the piston and displacer is not easily identifiable, however. There is also no increasing or decreasing trend. It is assumed that the contact between the piston

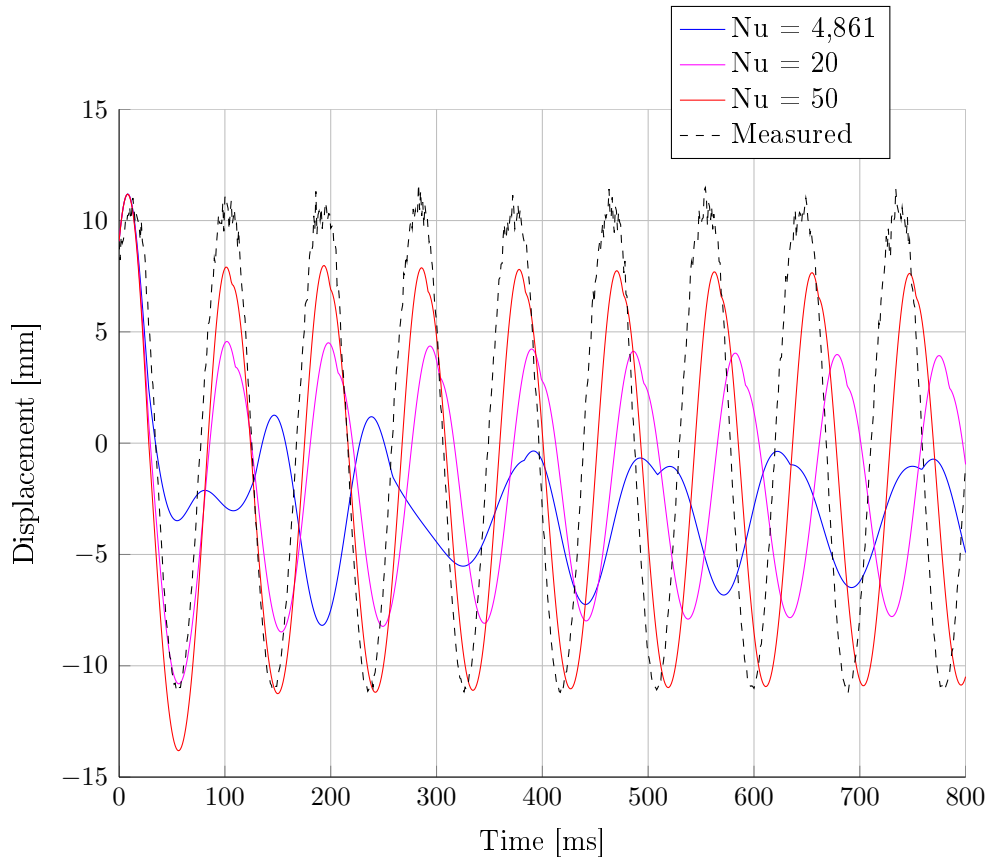


**Figure 3.6:** Piston motion.

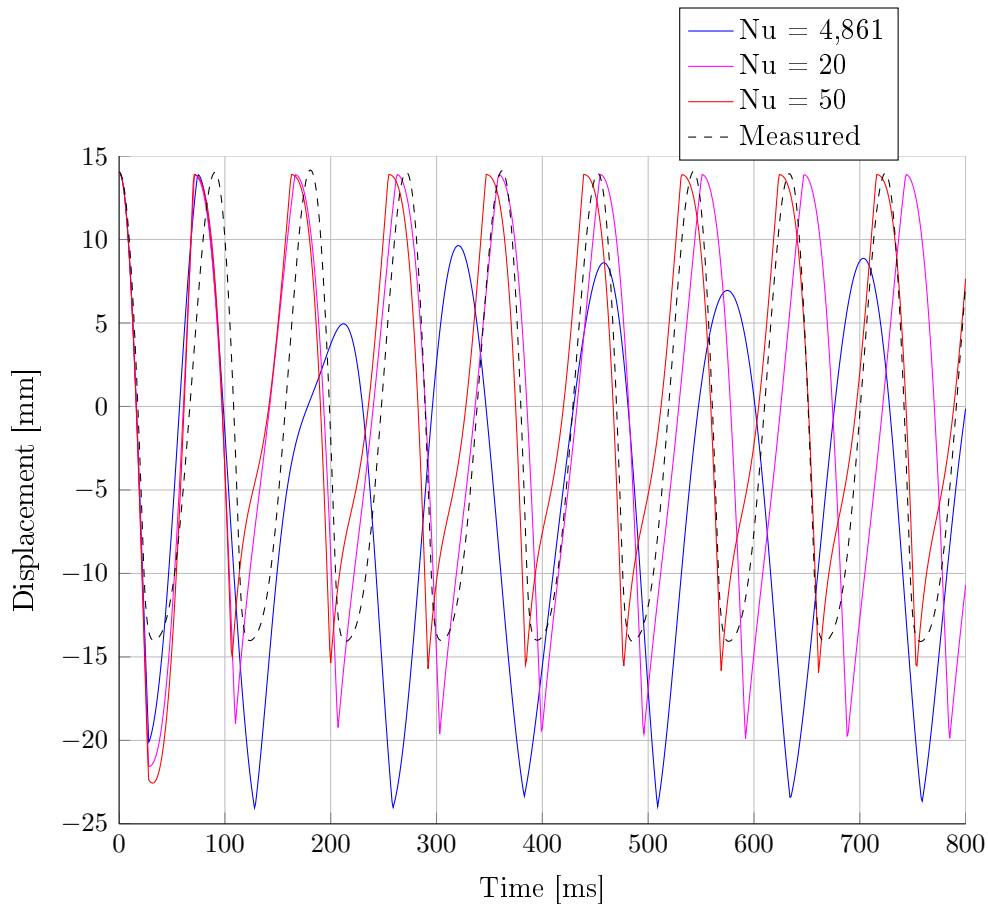


**Figure 3.7:** Displacer motion.

and displacer is a major cause. Contact between the piston and displacer altered the motion of both the piston and displacer. As seen in Figure 3.6, the motion of the piston is most affected when  $Nu = 4,861$ . This is shown by the sudden bumps (change of direction) caused in the piston motion. Contact also had a different effect on each of the cases.

After many attempts, it was not possible to conduct an experimental test without contact being present, however. This is assumed to be because of the reactivity of the displacer caused by its large displacer rod diameter. This is further discussed in Section 4.6 (page 49). The addition of load might have had an effect and was to be added by means of the electric generator, but the addition of the electric generator was not successful as discussed in Section 6.3 (page 69).

Since there was no load added to the piston for this experimental test, the piston and displacer should be in phase. In all cases, however, the piston and displacer are not in phase. The simulation thus takes account of energy consumption during



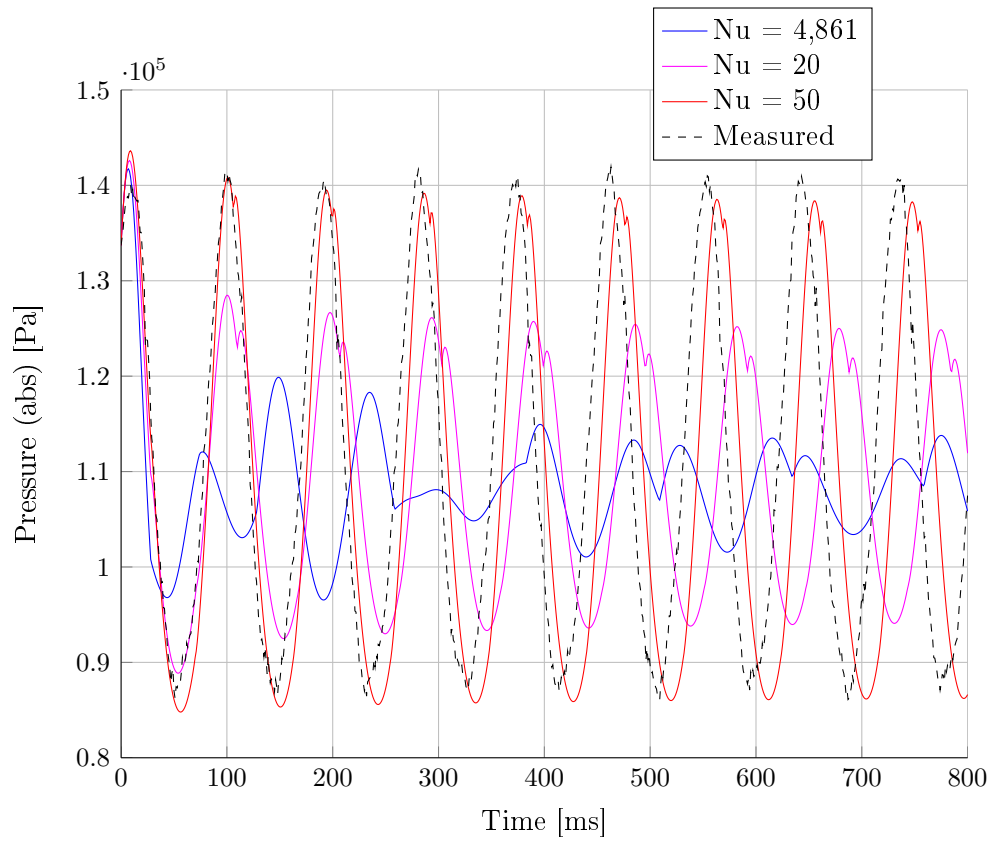


**Figure 3.8:** Pressure curves.

contact events, since the friction on the piston was assumed to be zero.

Although the variation of  $Nu$  forms part of the sensitivity analysis, further sensitivity analysis was done as described in Appendix D.

**Table 3.2:** Summary of theoretical simulation results.

<b>Test results</b>	$Nu = 4,861$	$Nu = 20$	$Nu = 50$	Measured
Piston stroke amplitude (peak-to-peak)	6,4 mm	11,8 mm	18,6 mm	22,2 mm
Displacer stroke amplitude (peak-to-peak)	32,3 mm	33,6 mm	29,8 mm	28,1 mm
Frequency	7,81 Hz	10,42 Hz	10,87 Hz	10,99 Hz
Phase angle between piston and displacer	132,2°	116,3°	121,3°	40,6°
$T_{hot}$ (average)	411,0 K	426,1 K	431,1 K	446,2 K
$T_{cold}$ (average)	349,0 K	324,6 K	315,2 K	305,4 K
Average pressure	108,029 kPa	108,829 kPa	109,128 kPa	111,969 kPa
Indicated power	0,098 W	1,100 W	1,818 W	0,659 W

## 4 Design

### 4.1 Introduction

A beta configuration was chosen as the design of choice, mostly because of its higher specific power as outlined in Section 2.3.4 (page 16). Originally, the development of a 3 kWe FPSE was the aim of this study but efforts were redirected to design an experimentally testable engine, which finally culminated in a redesign of the Beale B-10B demonstrator engine.

This chapter starts by describing the initial design challenges of the first experimental engine and the redirection to the redesign of the Beale B-10B demonstrator engine, referred to as the *presented engine*. The presented engine is described and compared to the Beale B-10B demonstrator engine.

Although the electric generator became over-specified after the objectives of this study were altered, it is included here, largely due to the manufacturing contribution that is made by this study. The electric generator is thus subsequently described and a section is also dedicated to the importance of the annulus size in the design. The annulus size was important since it served as an effective heat exchanger, which was found to be an important factor in the design of an FPSE.

The final section presents the results of a parametric study that was done to gain insight into the effect of input parameters on engine operation.

### 4.2 Initial design challenges

The first experimental engine that was manufactured was not functional. Firstly, a smooth running piston and displacer that could seal effectively were not attained with the initial engine. An internal and external Teflon (PTFE) bush was fitted to a stainless steel 316 piston. These bushes created the bearing and sealing surfaces between the displacer rod and piston (internal bush) and piston and cylinder (external bush). Teflon has a high thermal expansion coefficient compared to stainless steel 316, as well as a tendency to flow and change shape. Although both bushes were located at the cold side of the engine, the Teflon expansion was too large and caused temporary seizing of the piston and displacer rod.

The piston of the Beale B-10B demonstrator engine presumably is stainless steel, but is coated with a substance that allows the smooth motion necessary and that does not affect the clearance of the piston by means of its own expansion, since it is applied as a very thin layer. The sealing achieved between the piston and displacer rod of the Beale B-10B demonstrator engine is also very effective.

There are, in general, many more design challenges for an FPSE when compared to a kinematic Stirling engine. Apart from the stability issues that are addressed in Section 4.6 (page 49), the design of gas bearings and flexure bearings are challenges

on their own. A beta configuration FPSE generally necessitates the addition of both flexure bearings and gas bearings.

At the outset, flexure bearings of the standard shaker type (see Figure 2.8, page 21) were manufactured. These flexure bearings were chosen since they do not suffer from axial twist. No design information was attainable and samples had to be manufacture and tested to determine their characteristics. This process was very time consuming and similar processes would have been needed for the design of gas bearings. Internally charged gas bearings would have been used to negate the need for an additional compressor. The operation of internally charged gas bearings are also influenced by the operation of the engine, since the pressure required by the gas bearings is provided by the engine itself.

It therefore was decided to adapt the design of the Beale B-10B demonstrator engine to produce an experimentally testable engine and to, initially, avoid the design challenges mentioned.

The validation of the theoretical simulation model is particularly important for an FPSE because of the unpredictable behaviour of moving parts. Having a basic laboratory unit will allow the validation of the theoretical simulation model and serve to allow investigation to the addition of components such as flexure bearings and gas bearings, for example.

The development of a 3 kWe FPSE will thus require the development of all the supporting technology as well. This includes a control system for the control of moving parts, as well as matching the electric generator.

### 4.3 Design description

The Beale B-10B demonstrator engine shown in Figure 4.1 (a) consists of a piston and displacer, each connected to a compression spring. The engine is exposed to the atmosphere and orientated vertically to minimise friction in the form of side forces acting on the piston. Heating and cooling are achieved by making the displacer diameter slightly less than that of the cylinder to create a small annulus for air to flow between the compression and expansion spaces. This small annulus allows effective heat transfer between the wall and working fluid (see Section 4.5, page 48). Heat input to the engine is delivered by a heating ring that fits around the top end of the heater head. The upper part of the heating ring contains a groove and an integrated metal mesh. Fuel is added into this groove onto the metal mesh. As the fuel burns, it heats the part of the heater head above this ring.

The presented engine is shown in Figure 4.1 (b) and takes on the basic dimensions, as well as the piston and displacer, of the Beale B-10B demonstrator engine. The basic dimensions of the Beale B-10B demonstrator engine include the heater head internal diameter (35,98 mm) and length, as well as its wall thickness (0,5 mm). This leaves an annulus thickness of 0,99 mm between the displacer

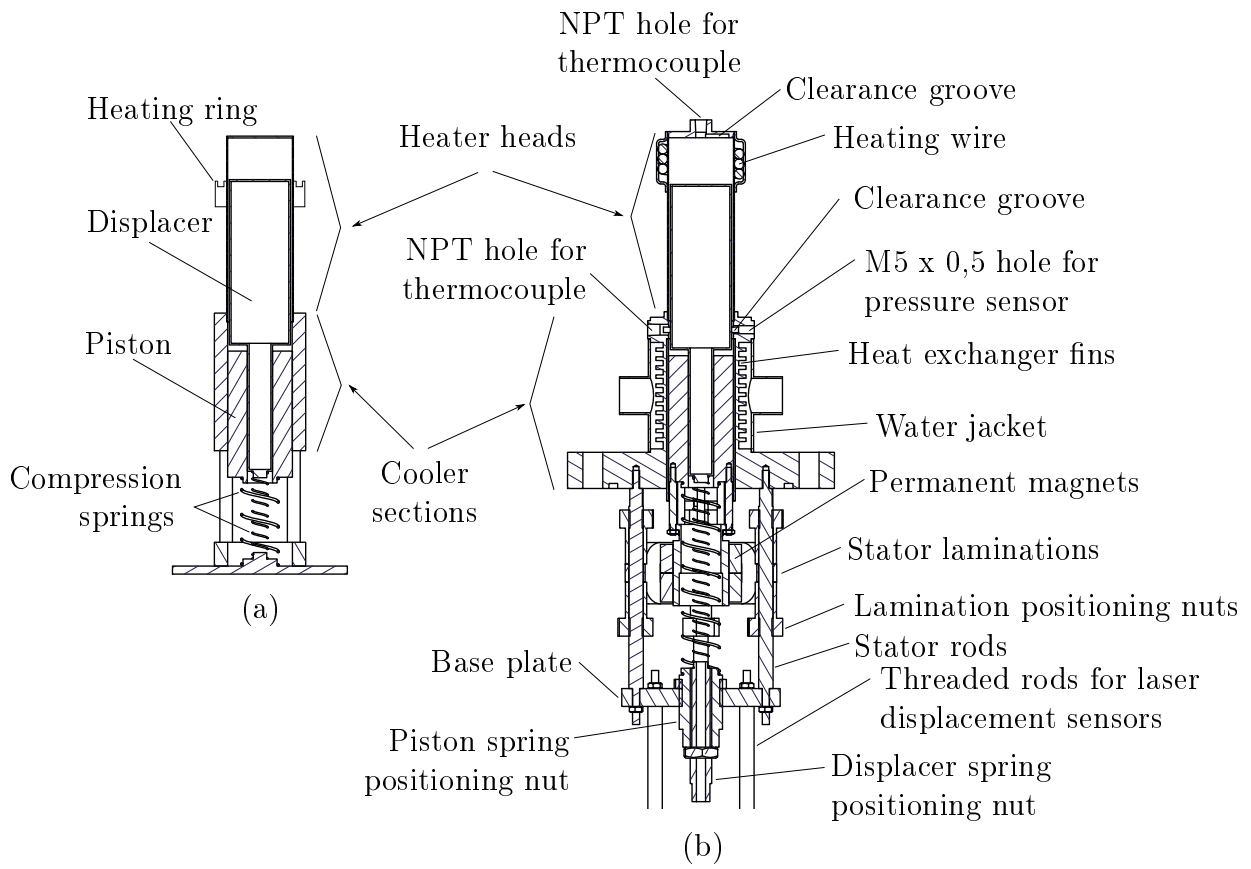


**Figure 4.1:** Engine comparison. (a) Beale B-10B demonstrator engine (Sunpower Inc.), (b) Presented engine.

and the heater head wall. The presented engine is also orientated vertically to eliminate side forces acting on the piston.

Design changes made specifically to accommodate the measuring equipment include three threaded holes. Two holes are NPT holes to accommodate compression fittings for thermocouple probes, and the other hole is a fine thread metric hole for a pressure sensor.

Two clearance grooves were added to allow the thermocouple probes to be inserted further into the engine. This improves the accuracy in reading the actual temperature of the desired location, since thermocouple probes consist of a steel sheath that conducts heat. One clearance groove is situated at the top of the heater head and the other at the cooler section (these clearance grooves are shown more clearly in Figure 5.2, page 57).

Heat input was provided by an electrical heating wire covered in ceramic beads, which was wrapped around the top end of the heater head and held in place by

four tabs lightly welded to the end of the heater head. A water jacket is located at the cooler section of the engine and serves to cool the engine. The heat exchanger fins improve heat transfer to the cooling water.

The piston runs inside a cast iron sleeve that was pressed into the cooler section of the engine by means of a mechanical press. The cast iron sleeve was only machined to specifications subsequent to being inserted into the cooler section of the engine. This is to ensure that a close tolerance fit was achieved between the piston and the sleeve, which is needed to effectively seal the working space of the engine.

The majority of the engine is made out of stainless steel 316; this includes the heater head and cooler sections of the engine. Stainless steel was chosen due to its favourable high temperature characteristics, availability and corrosion resistance, since the engine operates in air.

Compression springs are connected to the piston and displacer respectively. In the case of the piston, the compression spring is connected between the piston and the piston spring positioning nut. In the case of the displacer, the compression spring is connected between the displacer and the displacer spring positioning nut. These positioning nuts make it possible to alter the equilibrium positions of the piston and displacer independently. The piston positioning nut turns into the base plate while the displacer positioning nut turns into the piston positioning nut (Figure 4.1). The positioning nuts are metric bolts that have had their flats machined down to be smaller than the minor thread diameter.

Similar components were designed to allow variable positioning of certain other components. These include eight lamination positioning nuts for the positioning of the electric generator stator and four threaded rods for the positioning of two laser displacement sensors.

#### **4.4 Electric generator**

The electric generator is shown in Figure 4.2 and consists of (a) a stator assembly made up of coils and a stack of laminations and (b) a set of moving permanent magnets. The magnets are glued in a Halbach configuration onto a hollow shaft called the magnet holder. The magnet holder was attached to the piston by eight studs that contain thread and an accompanying shoulder at each end. The studs were turned into the piston first and then the magnet holder was attached to the studs by eight nuts. The magnet holder was only machined to specifications subsequent to being attached to the piston to ensure its geometry relative to the piston. The attachment of the magnet holder to the piston was very challenging and would be greatly simplified by manufacturing the piston and magnet holder monolithically. The addition of the magnet holder also results in the need for longer compression springs than those used in the Beale B-10B demonstrator engine.

The lamination positioning nuts position the stator by means of locating the

lamination stack. The lamination stack is essentially squeezed between two sets of four positioning nuts (see Figure 4.2).

The manufacture of the electric generator consisted of magnets and laminations that were externally manufactured and copper coils that were wound. The lamination stack was stacked to a thickness of 10 mm and contained 16 laminations. The laminations were stacked by being pushed onto the four stator rods protruding from the cooler section of the engine. The lamination positioning nuts serve to hold the lamination stack in place. The copper coils were then glued onto the lamination stack and connected in series.

The copper coils consisted of 167 turns each and were wound from 0,355 mm copper wire. The copper coils were potted in varnish to avoid the wires from moving due to magnetic forces during operation. Also, it was necessary to insert an intermediate material between the coils and the lamination stack. The lamination stack had some sharp edges and, when the coils were pushed onto the lamination stack, the insulation on the copper wires was compromised and caused a short-circuit. The intermediate material protected the copper wires from being cut by the lamination stack.

Arguably the greatest manufacturing challenge was the attachment of the magnets to the magnet holder. A jig made out of PVC had to be manufactured to accommodate difficulties brought on by the Halbach configuration. The configuration of the magnets, as well as the magnetisation of the magnets, is shown in Figure 4.3 (a).

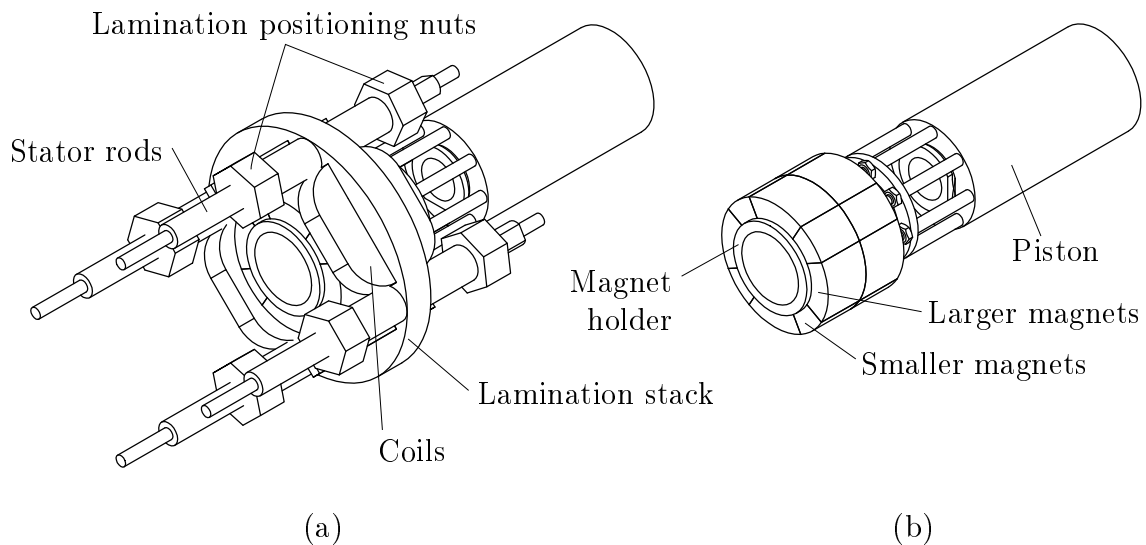


**Figure 4.2:** Electric generator assembly. (a) Stator assembly, (b) Magnet assembly.

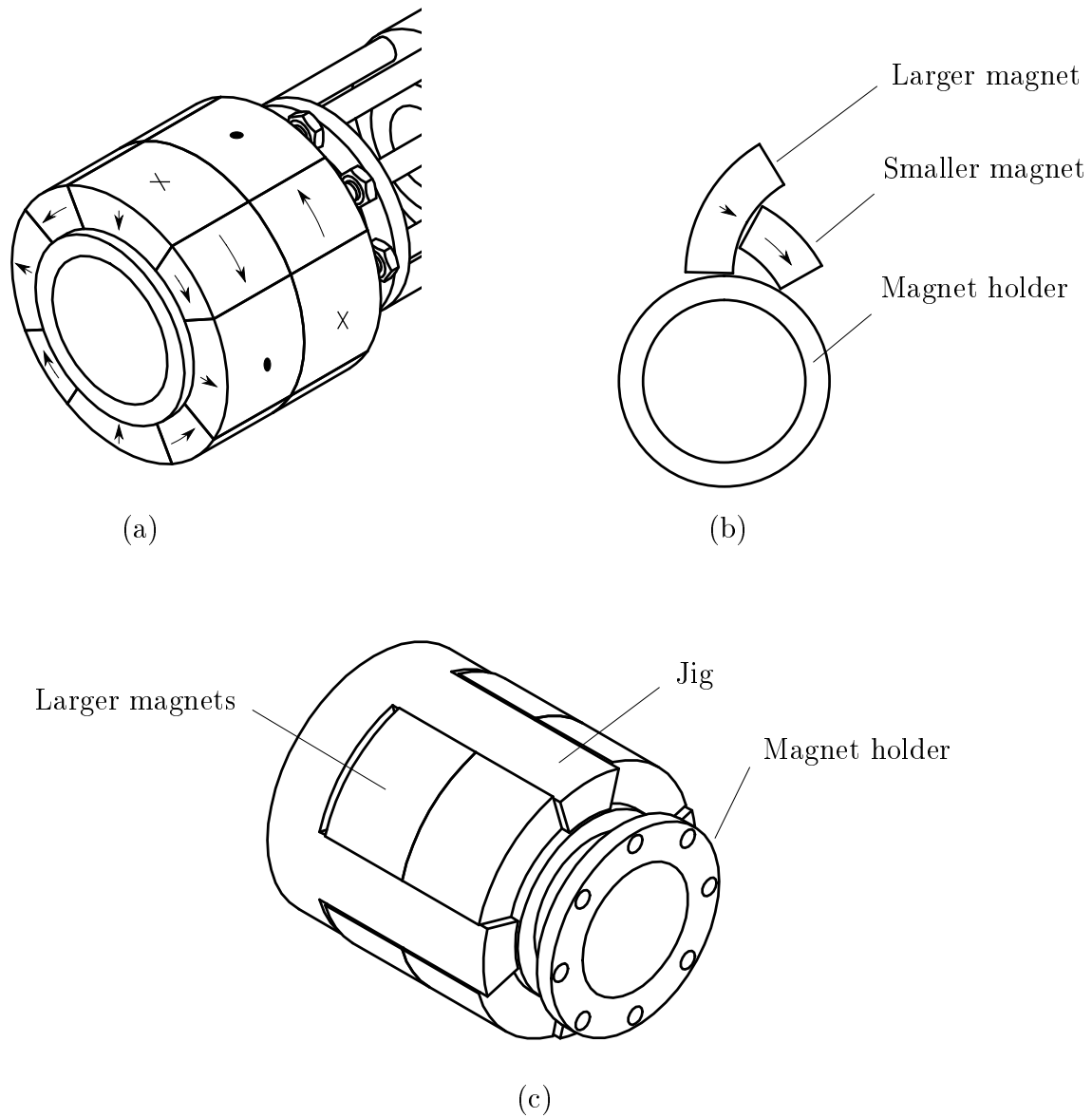


**Figure 4.3:** Attachment of magnets in a Halbach configuration. (a) Magnet configuration and magnetisation, (b) Tendency of adjacent magnets to move away from the magnet holder, (c) Assembly jig.

There are two rows of magnets alongside each other, with four pairs of larger magnets spaced equally around the magnet holder perimeter. The larger magnets are separated by four sets of smaller magnets. The larger magnets are radially magnetised either inward or outward. The smaller magnets are circumferentially



magnetised either clockwise or anticlockwise.

The major difficulty with regard to the attachment of the magnets to the aluminium (non-ferromagnetic) magnet holder was that they could not be glued on sequentially because of the repulsive and attractive forces brought on between adjacent magnets. Since the magnetic fields of adjacent magnets want to line up, the smaller magnets essentially want to creep underneath the larger magnets and hence push them upward, as shown in Figure 4.3 (b). To solve this difficulty, the sets of larger magnets were glued on first with the jig serving as a spacer, i.e. taking up the space of the smaller magnets (see Figure 4.3 (c)). A temporary mild steel rod was inserted inside the magnet holder to draw magnets onto the magnet holder to aid in the bonding process. The addition of the mild steel rod considerably simplified the attachment of the magnets, since there was no need to physically hold down the magnets while the glue was drying.

Once the larger magnets had been attached, the jig was removed and the smaller magnets were glued onto the magnet holder. Since the larger magnets on either side of a smaller magnet are magnetised in opposite directions, the smaller magnet has an equal tendency to creep under each of the larger magnets. The result is that the smaller magnet is pulled down onto the magnet holder and thus did not need to be held down by external means.

#### 4.5 Annulus size

The annulus size was found to be an important design consideration. The two main reasons are that a smaller annulus decreases dead volume and serves as a more effective heat exchanger. The decrease in dead volume increases the rate at which pressure changes, as was illustrated in Section 2.4.2 (page 18).

The other consequence of a smaller annulus is providing a more effective heat exchanger. Firstly, the Nusselt number at the outer wall of an annulus is expressed by means of the hydraulic diameter as (Çengel, 2006):

$$Nu = \frac{h \cdot D_h}{k} \quad (4.1)$$

Making  $h$  the subject of the formula:

$$h = \frac{Nu \cdot k}{D_h} \quad (4.2)$$

With the hydraulic diameter of an annulus defined as:

$$D_h = D_o - D_i \quad (4.3)$$

Assuming  $Nu$  to be constant, a smaller annulus thickness provides a smaller  $D_h$ , which in turn provides a larger  $h$  and thus an increased convection heat transfer rate. The assumption that  $Nu$  is constant is not necessarily valid, however,

since it depends on the state of the flow, i.e. laminar or turbulent, developed or undeveloped and so forth.

For the sake of convenience, if laminar fully developed flow is assumed then the Nusselt number becomes constant for flow in an annulus, but depends on the ratio  $D_i/D_o$ . As  $D_i/D_o$  increases from near 0,00 (flow in a pipe) to 1,00 (flow between two flat plates),  $Nu$  increases from 3,66 to 4,86 (Çengel, 2006). This then suggests that the effect of a smaller annulus on  $h$  is compounded and hence is further increased.

However, flow in a Stirling engine reverses many times a second, which produces a complicated analysis. Instead of further theoretical investigation of the flow regimes that occur, an experiment was conducted with two different heater heads to verify the assumption that a smaller annulus will produce more effective heat transfer.

The two heater heads were manufactured with the same wall thickness (0,5 mm) as that of the Beale B-10B demonstrator engine, but were slightly shorter. The inner diameters were made different to provide different annulus sizes. The resultant annulus sizes were 2,00 mm and 0,99 mm respectively. Although the first heater head (2,00 mm) did not provide any motion of the piston and displacer, the second heater head did.

The operation was not as convincing as that of the Beale B-10B engine. The stroke and frequency were evidently smaller. This added to the decision to take on the dimensions of the Beale B-10B demonstrator engine instead. The heater head was then lengthened and the performance of the engine was improved. This is assumed to be because of the improved separation of the hot and cold sides of the engine, and hence a greater temperature variation of the working fluid was realised.

## 4.6 Design by simulation

The theoretical simulation model was used to give insight into the effect that changing certain input parameters would have on engine operation. Parameters such as reaction under load, displacer rod diameter, mass of moving parts and so forth. The theoretical simulation model can thus serve as a very useful design tool. The theoretical simulation model can also be further validated in this manner. Although none of these outcomes have been experimentally verified, they provide a direction for future research.

The effect of a load on the piston was firstly investigated. The piston and displacer were given initial velocities of zero, and  $Nu$  set to 50. Other initial conditions such as temperatures, piston and displacer positions and so forth, remained unchanged as described in Section 3.6 (page 34). A load was added to the piston by means of a dynamic friction coefficient ( $Cf_p$ ):

$$Ff_p = Cf_p \cdot v_p \quad (4.4)$$

Values for  $Cf_p$  were taken from 0 to 10 N s/m. Maximum output power was around 168 mW as shown in Figure 4.4. Output power increases rapidly between zero load and  $Cf_p = 5$  N s/m. Output power then seems to plateau and the maximum output power is reached between  $Cf_p = 5$  N s/m and  $Cf_p = 8$  N s/m. Output power then slowly decreases with a further increase in load. An interesting outcome here is that output power seems to be near constant after a load of 5 N s/m, which relates to a constant output power over a range of loads.

The effect on other engine parameters are shown in Figure 4.5. The most interesting outcome is that the frequency seems to remain nearly constant with increasing load. This suggests that electric power should be able to be supplied at nearly a constant frequency and output power, independent of load. The addition of a well matched electric generator will allow this to be experimentally validated.

The piston stroke amplitude, however, seems to be the affected the most. The piston stroke decreases rapidly with increasing load but then seems to plateau. The opposite is true for the displacer, where the displacer stroke increases rapidly

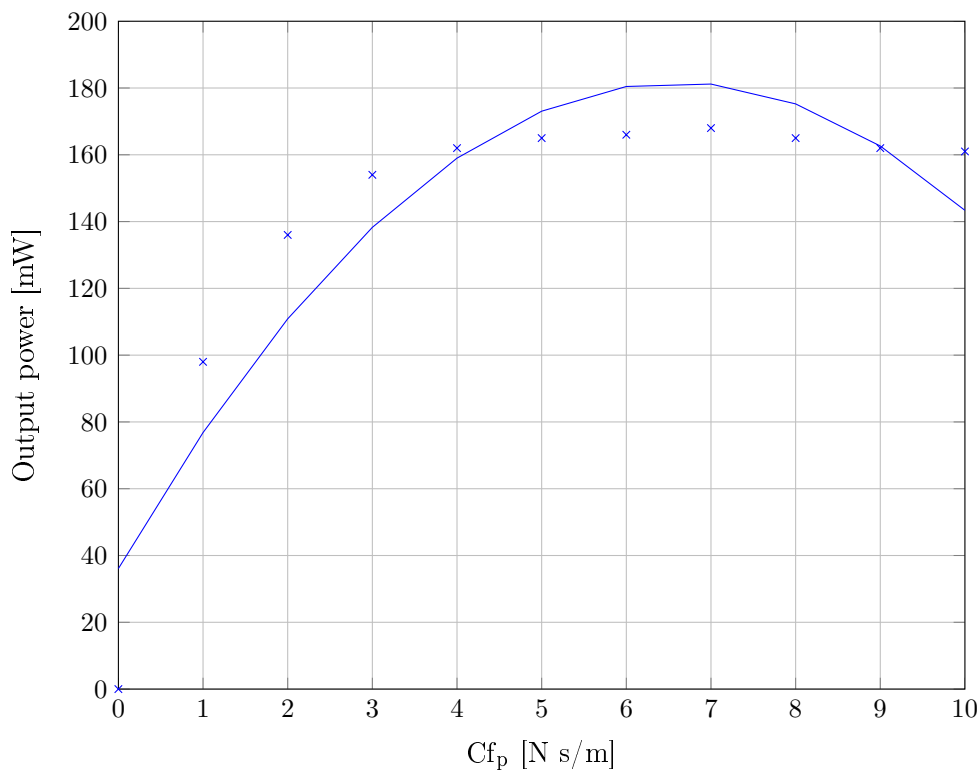


**Figure 4.4:** Output power versus load added to piston.

with increasing load but also seems to plateau. The phase shift between the piston and displacer also decreases with increasing load.

These outcomes suggest that an FPSE has a natural tendency to deliver a constant output power at a constant frequency, which is possible since the piston and displacer are uncoupled. With a control system, this tendency could be further exploited. On the contrary, however, the displacer makes contact with both the piston and heater head end cap in all cases. This shows that if unforeseen circumstances occur during operation and the piston and displacer are not adequately controlled, collision of these moving parts is very possible.

This led to the investigation of decreasing the displacer rod diameter since the displacer reacts less actively with a smaller rod diameter. This can be explain by simplifying Equation 3.2. If the working space pressure is assumed to be equal throughout the working space (specified here as  $p$ ) and frictional forces ignored, Equation 3.2 simplifies to:

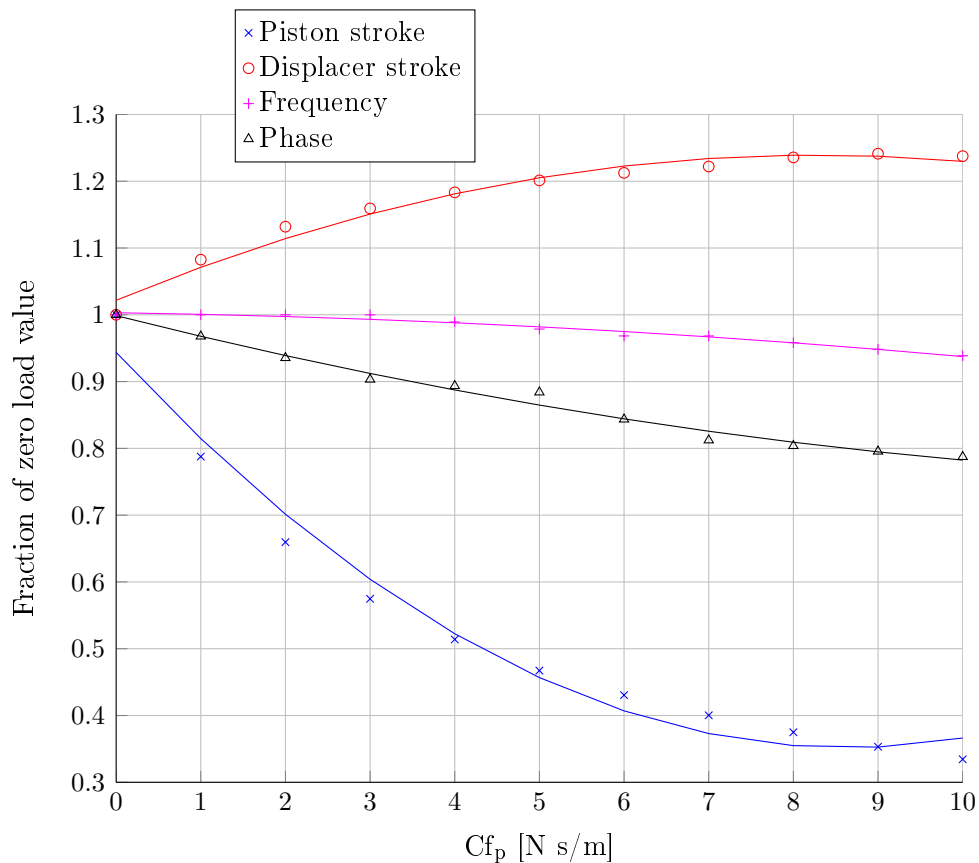


**Figure 4.5:** Effect on engine operation as piston load is increased.

$$\sum F_d = A_{rod}(p_{bounce} - p) \quad (4.5)$$

The rod diameters used in these simulations, were used as fractions of the original displacer rod diameter of the Beale B-10B demonstrator engine. The fractions investigated were 1/2, 1/4 and 1/8 (see Figure 4.6).

As was expected, no contact occurred between the piston and displacer (not shown). This is true for all the cases investigated. Contact was still present, however, between the displacer and heater head end cap.

As shown in Figure 4.6, phase, frequency and displacer stroke all decrease with decreasing displacer rod diameter. The piston stroke and output power, however, reach a maximum below the original displacer rod diameter and then start to decrease as the displacer rod diameter is further decreased. This indicates that there is a point of maximum power with regard to the displacer rod diameter and that it is an important design parameter, not only for displacer behaviour.

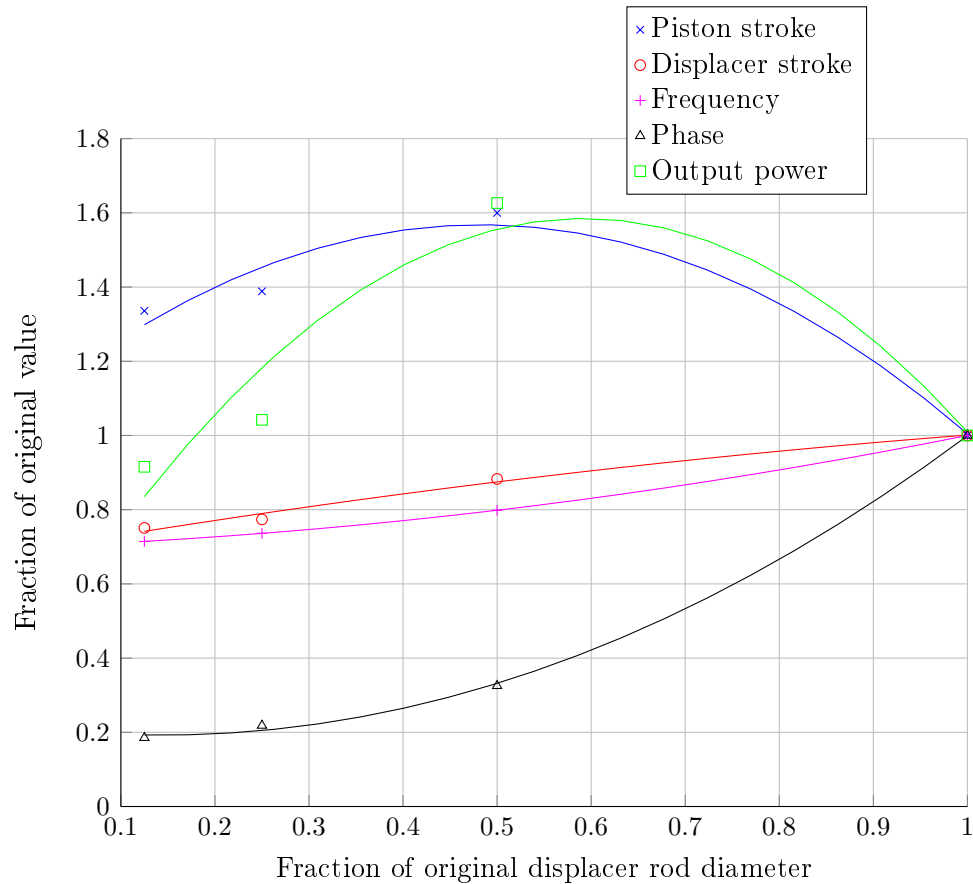


**Figure 4.6:** Effect on engine operation as displacer rod diameter is decreased.

The final set of simulations were done with respect to the piston and displacer masses and spring stiffnesses. The results are shown in Figure 4.7. In all cases, the original spring stiffness or mass was increased in fractions of 1,25, 1,50, 1,75 and 2,00.

The effect of varying the spring stiffnesses are shown in Figure 4.7 (a) and (b). An increase in the piston spring stiffness causes a decrease in piston stroke, displacer stroke, phase, output power and, to a lesser degree, frequency. A decrease in piston stroke would be expected with increased stiffness of the piston spring, but the effect on other parameters is not intuitive.

When the displacer spring stiffness is increased, however, almost the opposite happens. Here, phase, output power and frequency all increase, while the piston and displacer strokes seems to slightly increase or decrease but return to the original values. The output power is also seen to be a maximum near a fraction of 1,75.

The effect of increasing the masses of the piston and displacer is shown in Figure 4.7 (c) and (d).

As the piston mass is increased, the piston stroke amplitude increases as is expected. The rate of increase is exponential. As the piston mass increases by a factor of 2, the output power increases by a factor of 11,5.

This seems like an uncomplicated manner of increasing output power. It should be noted, however, that a greater reciprocating mass generates a new set of challenges. Firstly, the spring might be damaged with the greater mass and secondly, any stability problems or collisions would create a higher risk of failure. The possible stroke that is allowed by a flexure bearing is generally quite limited as well. Furthermore, it must also be possible for the existing heat exchangers to supply the increased heat transfer to the working fluid.

When the displacer mass is increased, piston and displacer strokes first increase and then decrease and seem to return to their original values, similarly to when the displacer spring stiffness was increased. The frequency and phase seem to decrease but then tend to plateau.

The most important outcome here, however, is the decrease of output power. This supports the idea that the displacer mass should be kept as low as possible, as is always advised in the literature. The displacer is simply a component needed to move working fluid between the hot and cold sides of the engine. Friction between the piston and displacer is also indicated to have a debilitating effect on engine operation as shown in Appendix D.

Although this study did not attempt to provide an optimum design, the theoretical simulation model was used to gain insight into the effect that the changing of certain input parameters would have on engine operation and showed challenges beyond that of optimum performance. Challenges that relate to whether there will

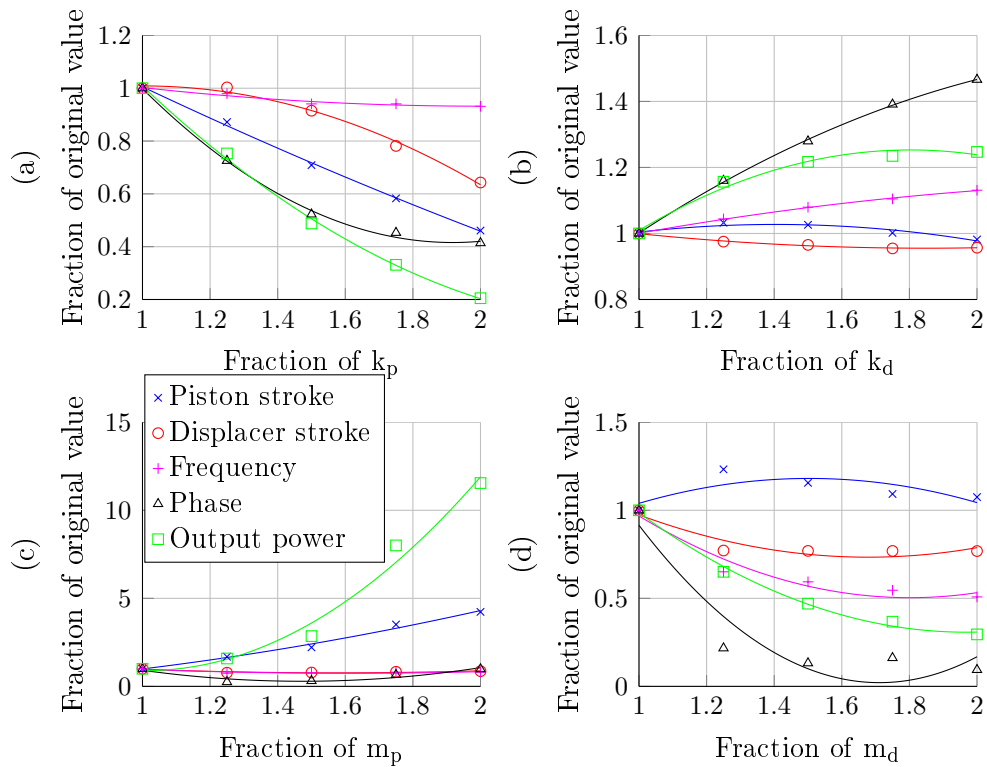


**Figure 4.7:** Effect on engine operation. (a) Increasing piston spring stiffness, (b) Increasing displacer spring stiffness, (c) Increasing piston mass, (d) Increasing displacer mass.

be contact between moving parts and whether the engine will be functional at all when referring to ineffective heat exchangers. With further development, this simulation model can be used to perform a parametric study to achieve an optimum design. It should also be noted that the design of the engine and electric generator should be done in parallel since the electric generator itself, must also be optimised.

## 5 Experimental test setup

This chapter describes the design of the experimental test setup and measuring equipment used to acquire the experimental test data. The insertion of the hot side and cold side thermocouples provided the greatest challenge in terms of the installation of measuring equipment.

### 5.1 Experimental test setup design

The experimental test setup is shown in Figure 5.1. A variable transformer was used to provide voltage to the electrical heating wire to supply heat input to the engine. A variable resistor was used as a load for the electric generator and the output voltage ( $G$ ) was measured.

Two K-type thermocouple probes were used to measure the hot side ( $T_{hot}$ ) and cold side ( $T_{cold}$ ) temperatures respectively. The compression fittings used were 1/16 inch NPT compression fittings.

The heater head was made out of solid round bar which was parted and machined into a tube and an end cap. Each was machined independently and located relative to the other by means of a recess in the end cap to provide a male-female fit, and subsequently was welded. The end cap was machined to include a clearance groove for the hot side thermocouple probe and a hole was tapped to allow the insertion of the compression fitting (see Figure 5.2 (a)).

The cooler section of the engine was also independently machined and located relative to the heater head by means of a recess and subsequently welded. The clearance groove for the thermocouple was machined internally (see Figure 5.2 (b)).

The insertion of thermocouples in the clearance grooves is illustrated in Figure 5.3. In each case, the compression fitting was loosely slipped on and the thermocouple was bent to the required shape. The compression fitting was then turned into the engine, the thermocouple was moved into the correct position and the ferrule was compressed onto the thermocouple.

The required shape was determined by repeatedly bending a wire of similar diameter to the thermocouple probe. The wire was then inserted to firstly see if it would fit into the engine through the hole tapped for the compression fitting, and secondly to ensure that the shape fitted the contour of the groove. It was challenging to avoid damaging the thermocouples by the sharp bends required. It was found the probes should only be bent once since they have a great tendency to crack if they are bent one way and then the other. A radius was included in the end cap to allow for a gradual 90° bend.

Although attempts were made to avoid welding, it was unavoidable in certain instances. Welding was considered undesirable because of thermally induced



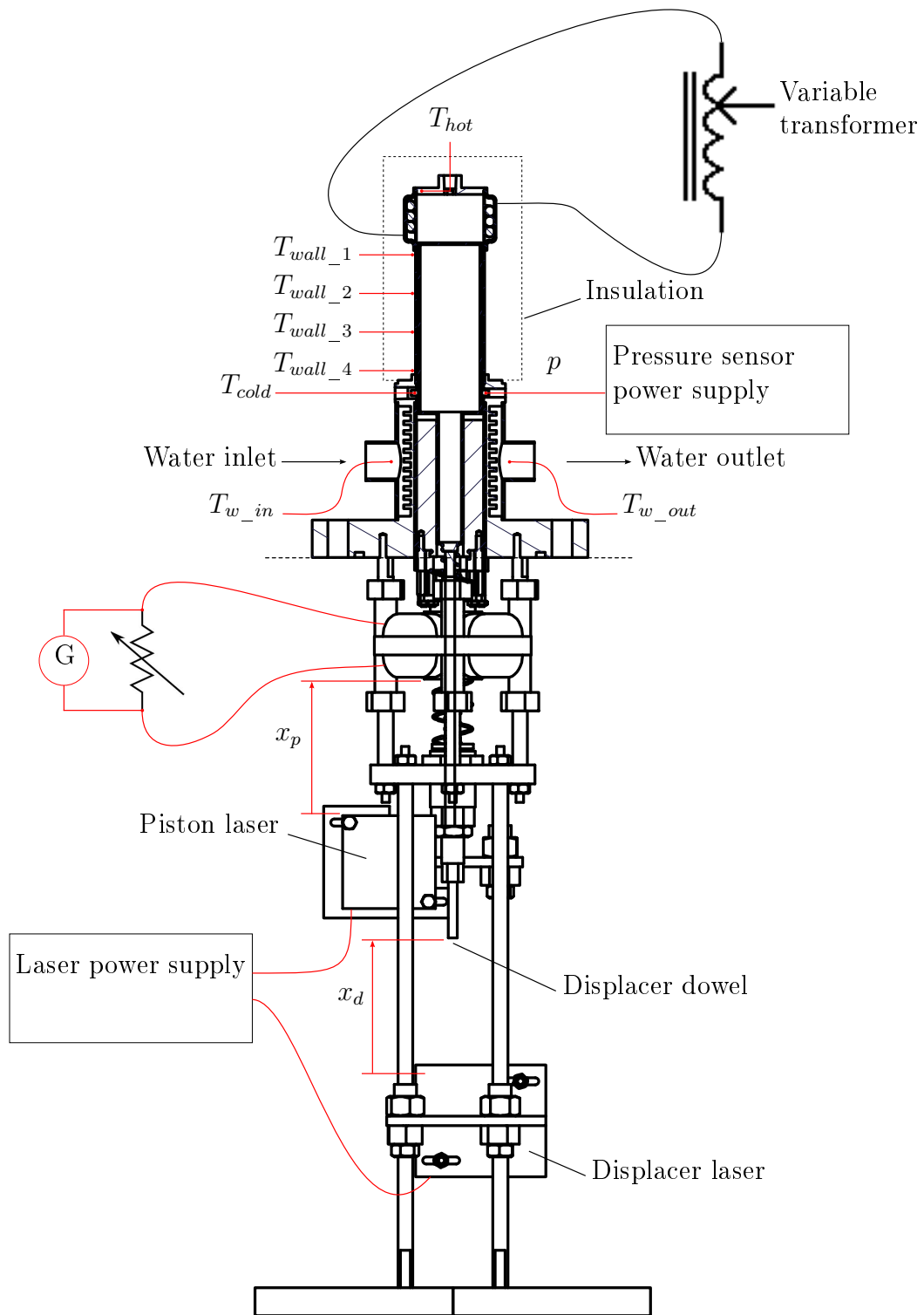
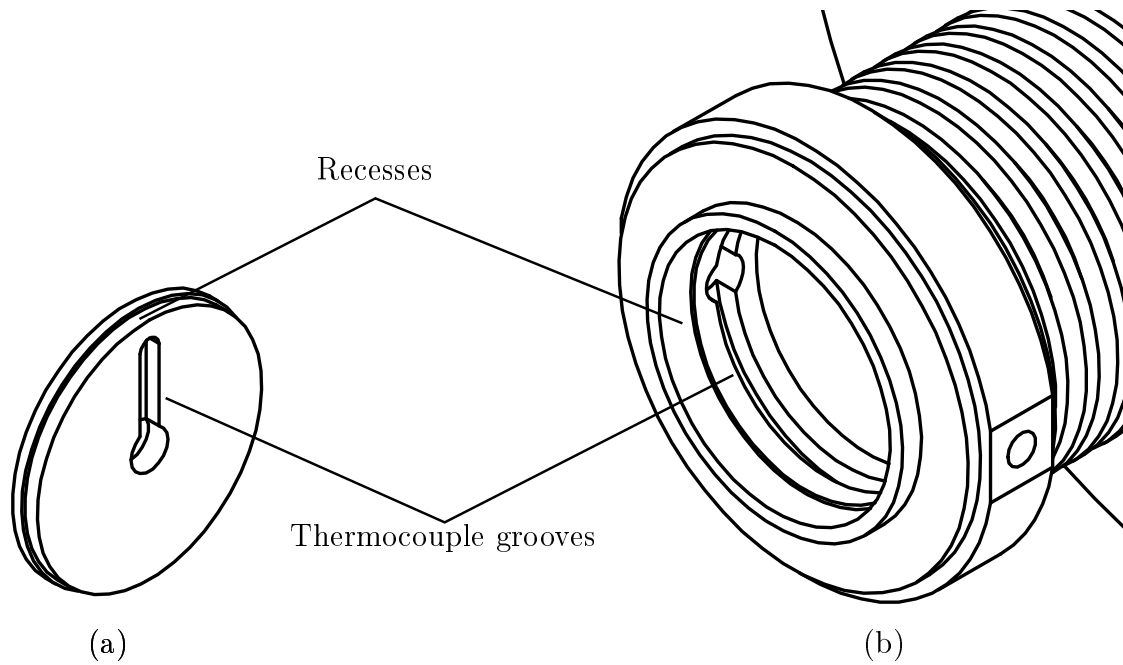
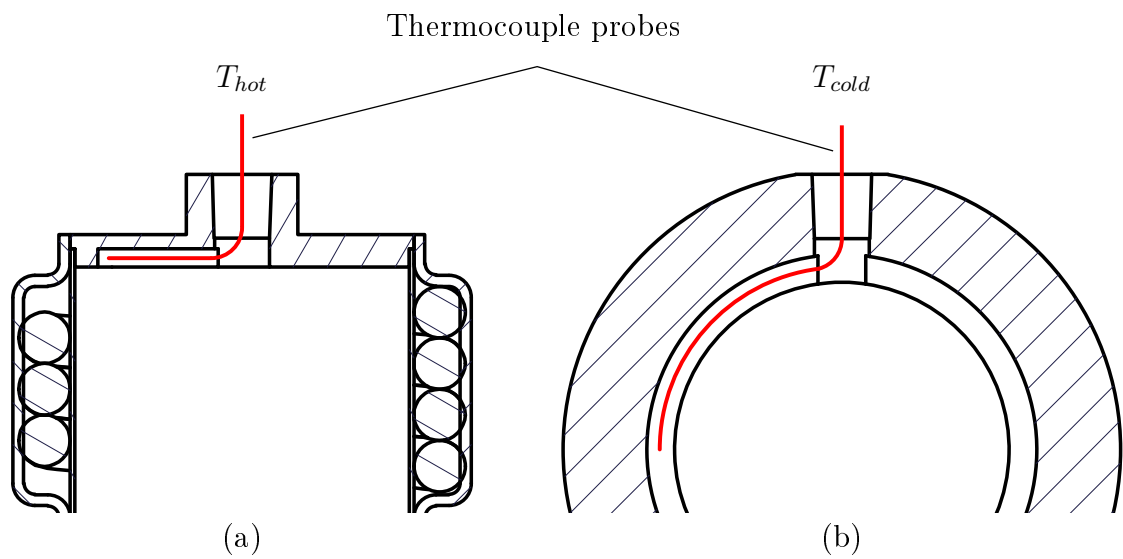


Figure 5.1: Experimental test setup.



**Figure 5.2:** Recesses and thermocouple clearance grooves. (a) Heater head end cap, (b) Cooler section.



**Figure 5.3:** Thermocouple insertion. (a) Cross-section of end cap groove, (b) Cross-section of cooler section groove.

stresses and deformation of components, especially the thin heater head wall. It is possible to machine the heater head out of one piece of solid round bar, but the machining of the groove in the end cap would be very challenging.

Four K-type wire thermocouples ( $T_{wall\_1}$ ,  $T_{wall\_2}$ ,  $T_{wall\_3}$  and  $T_{wall\_4}$ ) were fixed along the length of the heater head with stainless steel wire to provide data on the wall temperature (see Figure 5.4). The stainless steel wire was placed over the thermocouple wire and tightened by twisting the two ends of the stainless steel wire over each other at the opposite end of the heater head diameter.

Two K-type thermocouple probes were inserted into the water stream to mea-

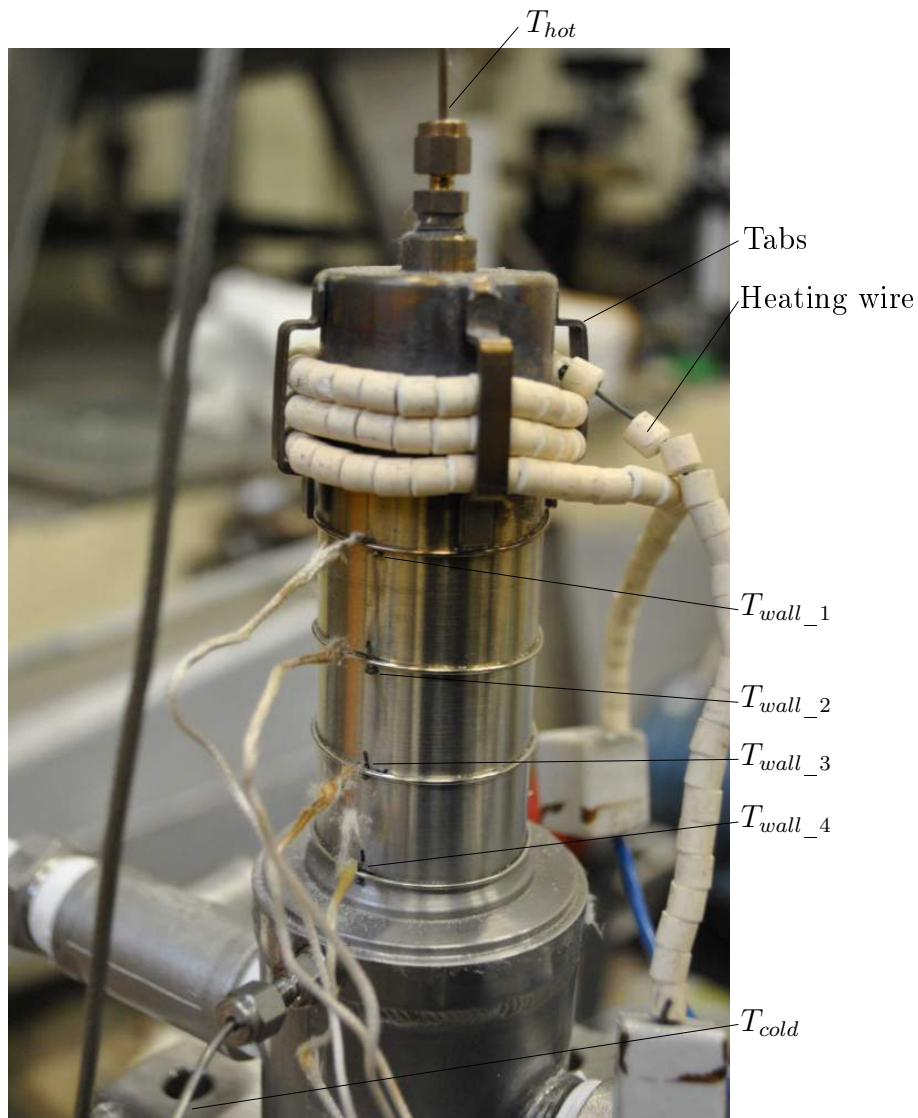


**Figure 5.4:** Heater head prior to insulation addition.

sure the inlet ( $T_{w\_in}$ ) and outlet ( $T_{w\_out}$ ) temperatures of the water jacket to determine the heat rejection of the engine. The thermocouples used were inserted by means of a 1/8 inch NPT fitting turned into a T-piece connected to the water jacket on both sides. The water flow rate was determined by running the outlet into a bucket of known volume and recording the filling time.

The water jacket was made by rolling sheet metal with two pre-cut holes and welding it to the cooler section. After welding, the two holes of the water jacket sit directly opposite each other. Two stainless steel nipples (external thread) were then parted and machined to fit over these holes and welded. The nipples allow the attachment of piping for the water supply to the water jacket.

Ceramic wool insulation was wrapped around the heater head to minimise heat loss to the environment. The pressure ( $p$ ) was measured opposite  $T_{cold}$  at the cold side of the engine to avoid temperature effects on the measurements.

Laser displacement sensors were used to measure the displacement of both the piston ( $x_p$ ) and the displacer ( $x_d$ ), mainly because laser displacement sensors do not interfere in the movement of an object and have short response times. Enough exposure of the measuring surface must be achieved, however, since laser displacement sensors have an emitter and pick-up situated alongside each other and neither the outgoing nor incoming wave may be blocked. A slot was drilled to allow enough exposure of the piston, while a dowel was stuck onto the displacer to provide a clear measuring surface.

The dowel protruded through the displacer spring positioning nut, which had a hole through its centre. The dowel thus served to extend the measuring surface of the displacer. Two circular disks were cut from rigid plastic and attached to the end of the magnet holder and displacer dowel respectively. The circular disks provided a greater surface area to which the lasers could be aimed.

## 5.2 Measuring equipment

An Optrand AutoPSI-S fibre-optic pressure sensor was used to measure pressure because of its small size and short response time (frequency range of 0,1 Hz to 20 kHz). The sensor consists of a measuring tip, which is a M5 x 0,5 fitting, and a fibre optic wire that runs to the sensor electronics.

Wenglor laser displacement sensors (YP11MGV80 and YP11MGVL80) were used to measure  $x_p$  and  $x_d$  respectively. These sensors are reasonably small (50 mm x 50 mm x 20 mm), with a response time of 500  $\mu$ s, but can only measure in a range of between 50 mm and 100 mm away from the laser.

The thermocouple probes were all K-type probes with a sheath diameter of 1,5 mm. The thermocouple wire used was K-type thermocouple wire of 0,25 mm diameter with the tips connected by means of a spot-weld.

A National Instruments data logger was used. A National instruments cDAQ-9172 chassis was used together with National instruments data cards to take ther-

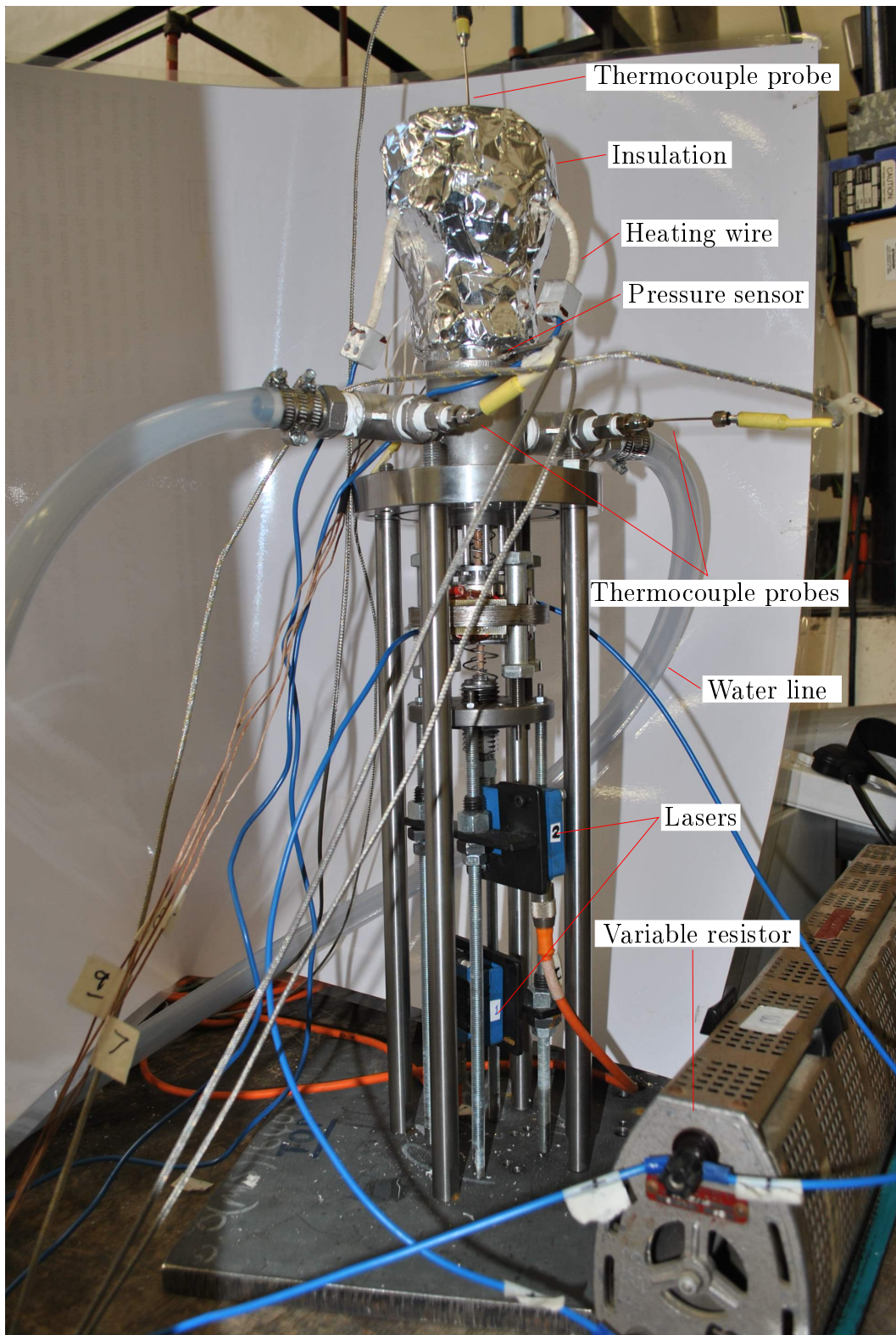


Figure 5.5: Photo of experimental test setup.

mocouple readings (NI 9213), and to measure laser and pressure sensor output voltages (NI 9215) and the electric generator output voltage (NI 9221).

A photo of the test setup is shown in Figure 5.5, and more information as well as the calibration of the equipment is provided in Appendix A.

## 6 Results and discussion

Two sets of experimental tests were conducted on the engine, the first test being conducted prior to the addition of the electric generator and the second test conducted subsequent to the addition of the electric generator. This was done to determine the influence of the electric generator assembly.

### 6.1 Setting equipment references

This section refers specifically to relating the piston and displacer positions to determine the compression and expansion space sizes. Before heat was applied to the engine, two references were determined, one for the piston laser and one for the displacer laser, as follows (Figure 6.1):

$$x_e = x_{d\_ref} - x_d \quad (6.1)$$

$$x_c = L_{c\_ref} - (x_p - x_{p\_ref}) - x_e \quad (6.2)$$

Here,  $x_{d\_ref}$  represents the position of the displacer when pushed up as high as possible, i.e. pushed against the heater head end cap. Similarly,  $x_{p\_ref}$  represents the position at which the bottom of the piston was held flush with the bottom of the cast iron sleeve. The length of the compression space when the piston was held at position  $x_{p\_ref}$  and the displacer was held at position  $x_{d\_ref}$  (i.e.  $x_e = 0$ ) is represented by  $L_{c\_ref}$  and calculated as follows:

$$L_{c\_ref} = L_{measured} - L_p - L_d \quad (6.3)$$

The value for  $L_{measured}$  was determined theoretically from the design drawings and verified by physical measurement with a vernier caliper.

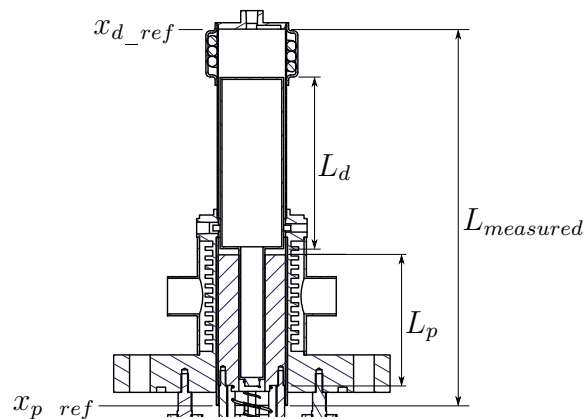


Figure 6.1: Reference positions.

## 6.2 Engine test without electric generator

The first test conducted was of the engine being operated before the addition of the stator assembly and the addition of the magnets to the magnet holder. Although unstable operation was unavoidable, steady operation (i.e. repeating motion) was achieved at  $T_{hot} = 446,2$  K with an operating frequency of 10,99 Hz. There was no measurable change in the cooling water temperature because of the low heat input and hence output. The water jacket failed in this instance as a means of calculating heat output, but did serve to cool the cooler section of the engine adequately by keeping  $T_{cold} = 305,4$  K while  $T_{w\_in} = 291,5$  K.

Figure 6.2 shows the piston and displacer motion. All curves were adjusted to have a zero offset to emphasise the stroke of the piston and displacer.

The displacer curve was seen to lead the piston curve by  $40,6^\circ$ , while the stroke (peak-to-peak) of the piston and displacer was 22,2 mm and 28,1 mm respectively. The erratic behaviour seen at the peaks of the piston motion was assumed to be slip-stick effects, since this was where the piston came to zero velocity and then changed direction. Slip-stick is characterised by a transition between static and dynamic friction. This was not seen at the troughs, however, since a greater portion of the piston protruded out of the cast iron sleeve. Less surface area is exposed to friction by means of contact with the cast iron sleeve, resulting in smoother motion.

When looking at the variation in the compression and expansion space volumes in Figure 6.3, it is evident that there was contact between the piston and displacer. The compression space is seen to rapidly tend to zero and then abruptly change direction, unlike its corresponding peaks, which show a much smoother transition. A rubber spacer prevents the compression space to reach zero, while the abrupt change of direction shows how the displacer essentially bounces off the piston, suggesting an elastic collision condition.

Contact was also evident between the displacer and the heater head end cap by a distinct metal-on-metal knocking sound. This was not as clear when referring to the variation in expansion space volume, since the displacer already was in the process of decelerating before collision.

Figure 6.3 is slightly misleading, however, since it provides the volume of the compression and expansion spaces. The actual minimum distance between the piston and the displacer ( $x_c$ ) was measured to be 3,1 mm, while the minimum distance between the displacer and heater head end cap ( $x_e$ ) was measured to be 0,5 mm. Theoretically, however,  $x_c$  should be less than the rubber spacer diameter (1,75 mm) and  $x_e$  should be 0 mm. This shows measurement errors of 1,35 mm and 0,5 mm respectively.

The measured pressure curve is given in Figure 6.4, which shows an average pressure of 111,378 kPa while the atmospheric pressure was 99,519 kPa. Operation



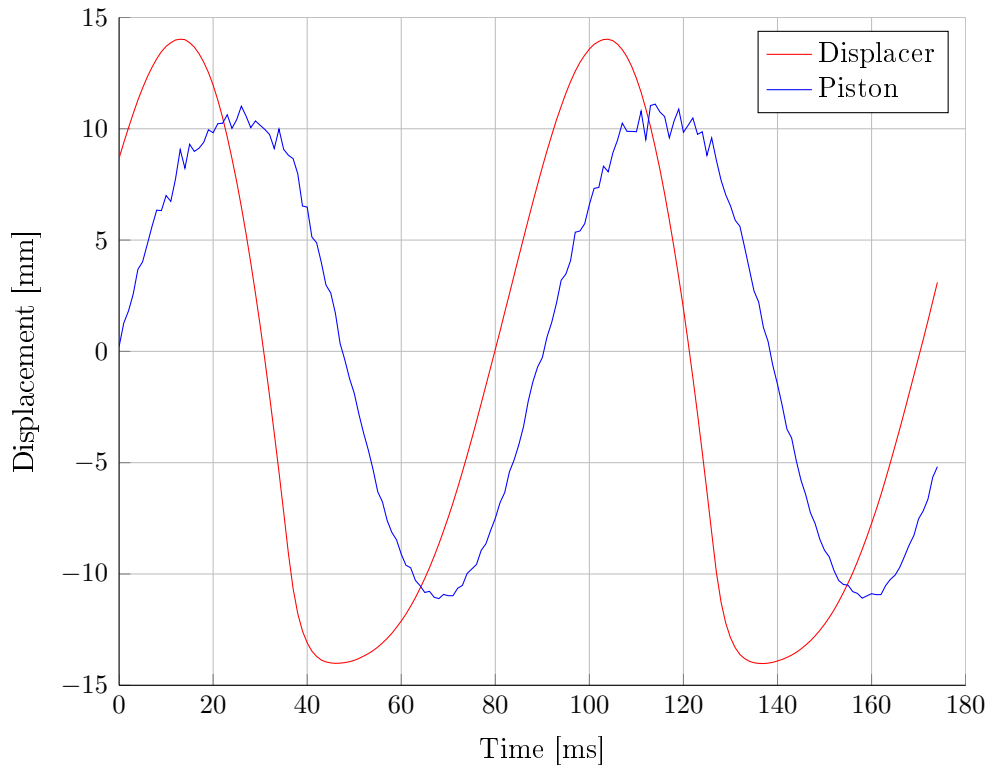


**Figure 6.2:** Piston and displacer motions.

was thus at an average greater than atmospheric pressure.

The resultant p-V diagram in Figure 6.5 shows an indicated power of 0,659 W. A positive value for power was expected since the displacer leads the piston. If the piston and displacer were in phase, then the pressure and volume curves would be in phase and no power would be produced.

Although the indicated power theoretically should be zero in this case since there was no load, dissipative effects still were present and the indicated power thus was the power needed to overcome these. Dissipative effects could include any of the following: energy consumption during contact events, sliding friction, skin drag acting on the displacer and so forth.

With regard to the repeatability of experimental results. This was challenging to accomplish. For the test setup presented here, it was difficult to achieve the same flow rate over the water jacket, as well as achieving the same hot side temperature. The temperature of the water was also something that could not be controlled. The water flow rate was determined by a tap that was operated by hand, while the voltage variation over the heating wire was provided by a variable transformer. The variable transformer output voltage could be changed by hand to achieve the

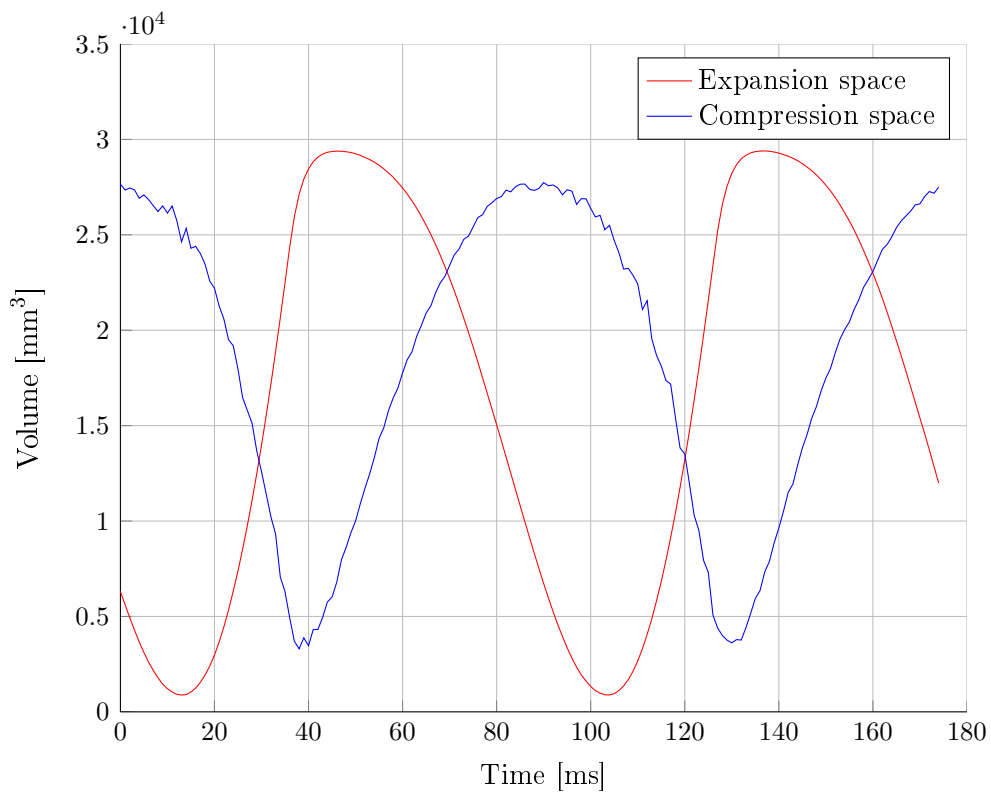


**Figure 6.3:** Variations in volume of compression and expansion space.

desired hot side temperature, but this would not be practical.

In order to make this experiment more repeatable, a control system will be needed for the water flow velocity and temperature, and a control system for the voltage over the heating wire to ensure the same hot side temperature. The piston and displacer positions, at stand still, will also have to be verified. The piston and displacer positions can easily be adjusted by hand before operation, however.

A summary of the results and engine parameters is given in Table 6.1.

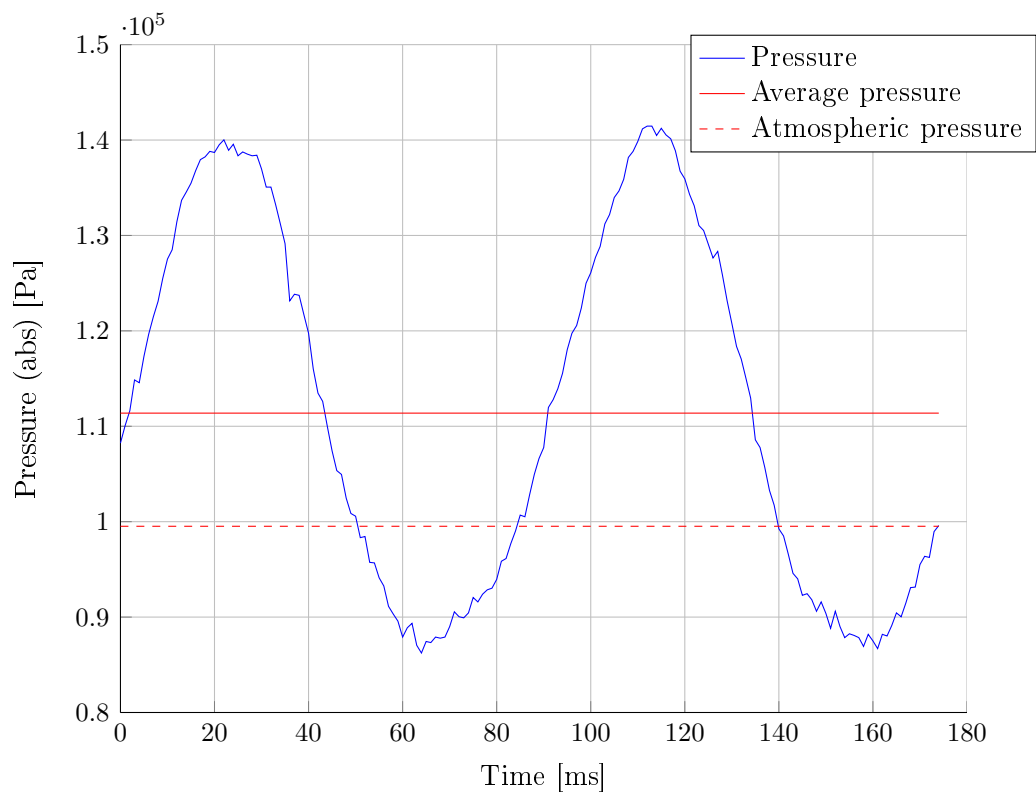


**Figure 6.4:** Pressure curve.

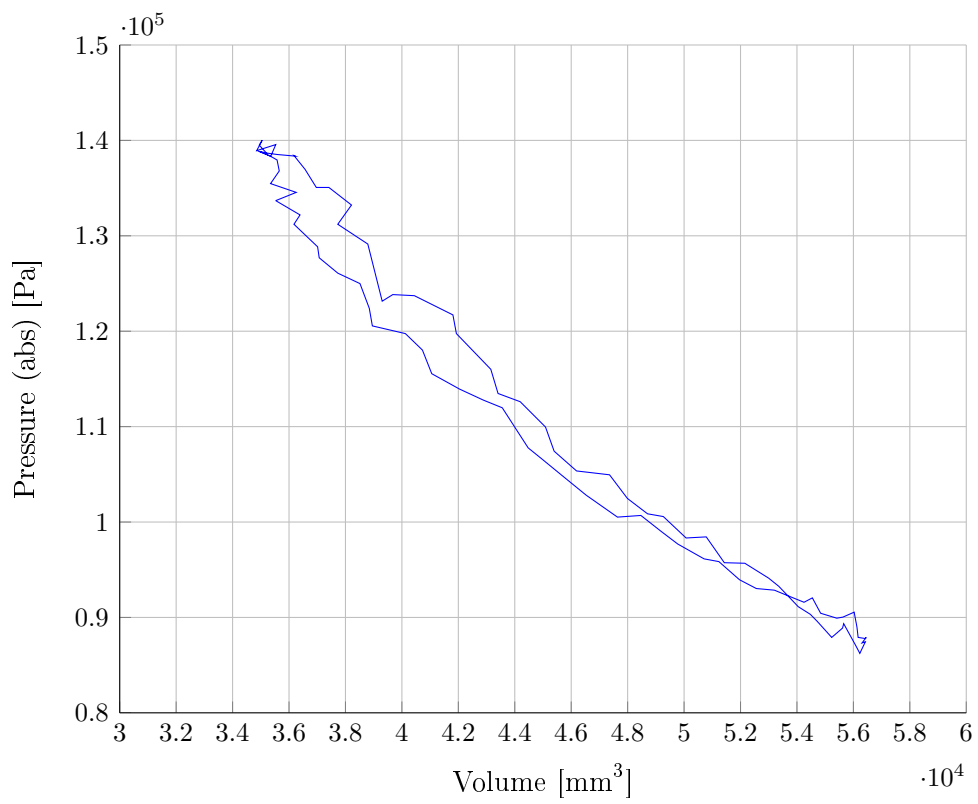


**Figure 6.5:** Resultant pressure-volume curve.

**Table 6.1:** Summary of the experimental test of the presented engine without electric generator.

<b>Engine parameters</b>	
Displacer mass	76,3 g
Piston mass	511,0 g
Displacer spring constant	162,9 N/m
Piston spring constant	270,9 N/m
<b>Test results</b>	
Frequency	10,99 Hz
Average pressure	111,378 kPa
Atmospheric pressure	99,519 kPa
$T_{hot}$	446,2 K
$T_{cold}$	305,4 K
Displacer stroke (peak-to-peak)	28,1 mm
Piston stroke (peak-to-peak)	22,2 mm
Phase angle between piston and displacer	40,6°
Indicated power	0,659 W

### 6.3 Engine test with electric generator

The second test conducted was of the engine being operated subsequent to the addition of magnets to the magnet holder and the addition of the stator assembly. The addition of the electric generator proved to be a source of challenges, however. Although reciprocating motion was achieved above about 673 K, it was discontinuous. The hot end temperature was limited to below 773 K to prevent damage to any equipment.

The first test was done with no electrical load (i.e. open-circuit) to determine the effect of the electric generator on the frequency of operation of the engine. When being operated as an open circuit, the electric generator should act as a magnetic spring.

Subsequent to the open-circuit test, the variable resistor was attached to the electric generator to induce a load, and samples of differing electrical load were taken.

The piston and displacer motions for the open-circuit test are shown in Figure 6.6. The piston motion approaches a square wave form with shorter stationary periods at its upper limit and longer stationary periods at its lower limit. Velocity thus is only seen when transition occurs from the upper limit to the lower limit or vice versa, as is evident from the sudden voltage peaks in the electric generator output shown in Figure 6.7, which coincide with these transition periods.

It is also clear from Figure 6.6 that the addition of the magnets dominates the resultant motion of the piston and displacer. As was mentioned, the addition of the magnets should only alter the spring constant of the piston when operated as an open circuit, when the expected motion would be similar to the test without the electric generator. Instead, the magnets have a tendency to assume one of two positions and not to return to their central position. The cause is assumed to be the high strength of the magnets used (N35).

Furthermore, contact between the piston and displacer was again present, as seen in the sudden jump of the displacer in Figure 6.6, as well as the compression space shown in Figure 6.8. The sudden jump was not seen in the piston, since its mass was 6,7 times that of the displacer. The influence of the attached magnets was also assumed to contribute to the resultant piston motion.

When looking at Figure 6.8 it is again seen that the compression space did not go to zero as it theoretically should have. Here, the minimum value of  $x_c$  is  $-2,6$  mm. More investigation is needed to determine the source of this error. The laser sensors were calibrated as shown in Appendix A, and references were set as explained in Section 6.1 (page 62) to ensure that there was no offset error. It is possible that the offset error could be because of the vibration of the plastic disks that were attached to the magnet holder and displacer rod to provide clearer measuring surfaces for the lasers. The vibration of the laser displacement sensors

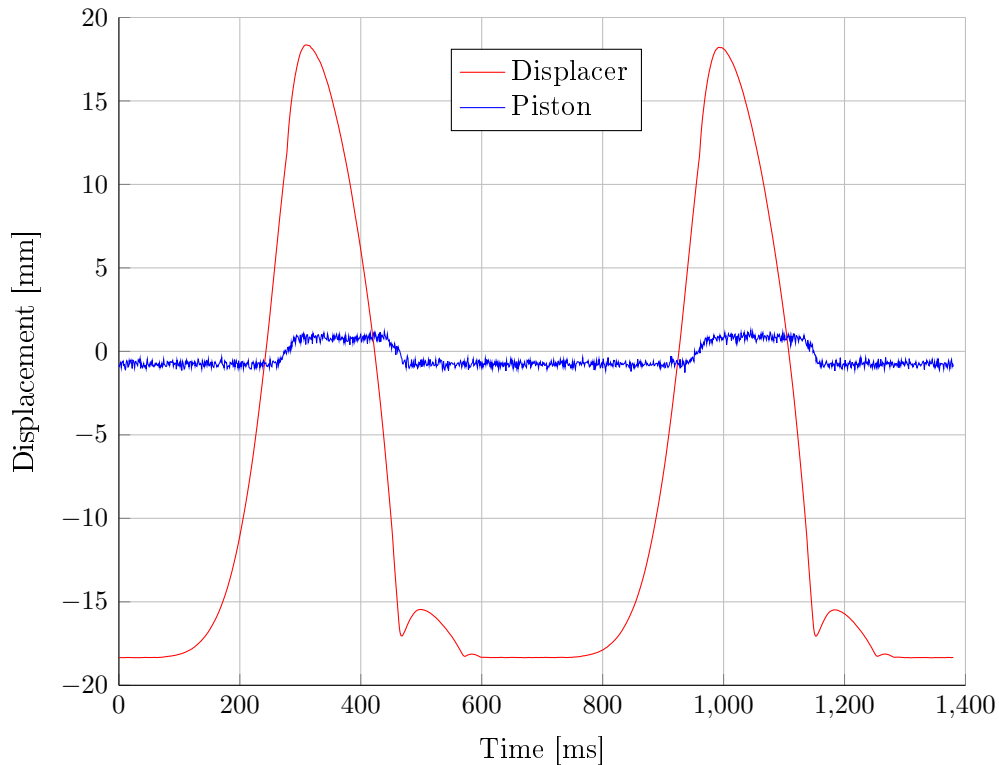


**Figure 6.6:** Piston and displacer motions.

themselves caused by engine operation was another possible source of error.

The pressure curve is shown in Figure 6.9. Periods of high pressure were more prolonged than low pressure periods and hence the piston was pushed downward for longer than upward. As the displacer descended and made contact with the piston, it bounced off and subsequently moved back to the piston and both sat stationary. The pressure was then at its maximum, since the majority of working fluid was in the expansion space. The pressure then gradually reduced with a staggered motion, which eventually caused the displacer to be forced away slightly from the piston, upon which the pressure was reduced further since working fluid was pushed into the compression space and a type of chain reaction occurred. The average pressure was calculated as 107,752 kPa.

The closed-circuit tests produced similar results, since the magnets of the electric generator dominated the motion of the piston. These results are summarised in Table 6.2.

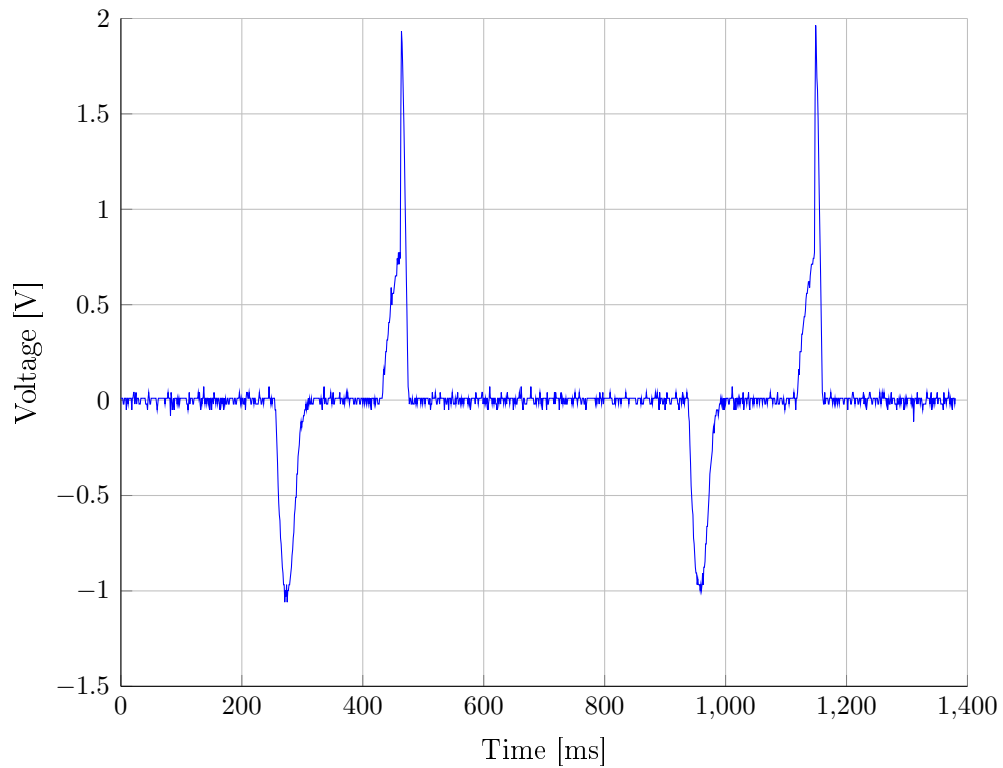


**Figure 6.7:** Electric generator output voltage.

**Table 6.2:** Summary of the experimental test of the presented engine with electric generator.

Test results	Open circuit	$R = 10,7 \Omega$	$R = 34,0 \Omega$
Frequency	1,47 Hz	1,29 Hz	1,40 Hz
Average pressure	107,752 kPa	108,343 kPa	107,896 kPa
$T_{hot}$	672,4 K	680,2 K	674,9 K
$T_{cold}$	297,6 K	298,1 K	297,8 K
Indicated power	0,144 W	0,138 W	0,141 W
Electrical power	-	1,79 mW	1,23 mW



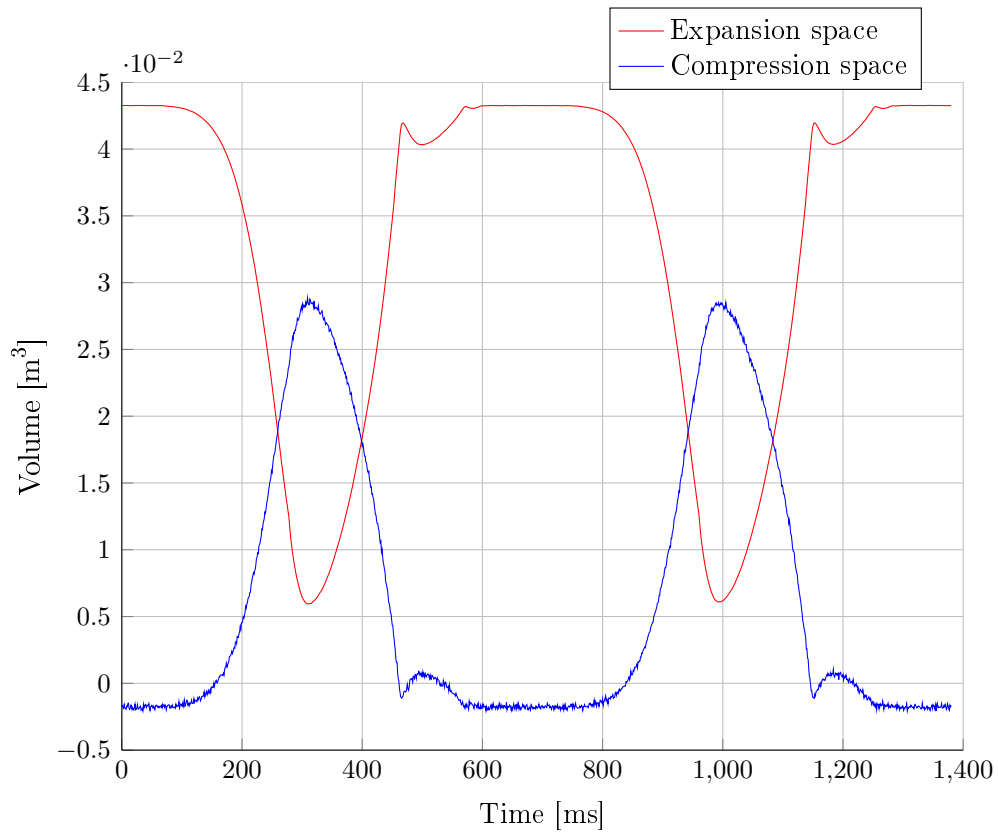


**Figure 6.8:** Variations in the volume of the compression and expansion space.

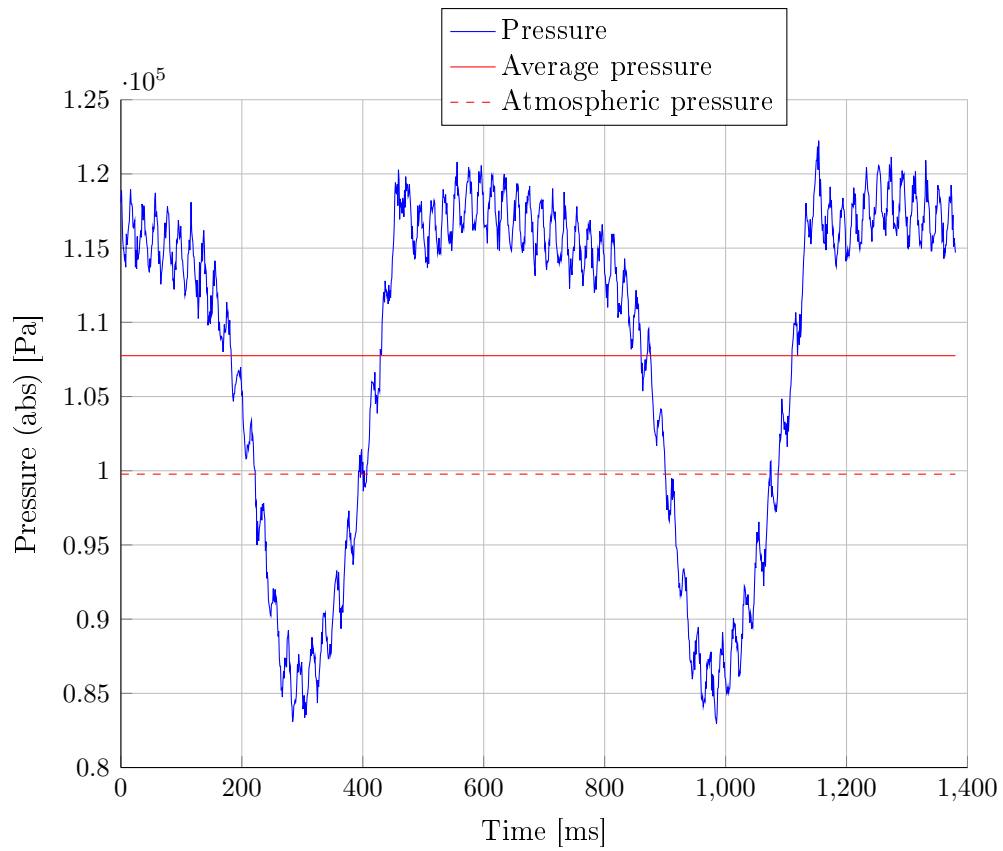


**Figure 6.9:** Pressure curve.

## 7 Conclusions

Although the FPSE was already invented in 1964 and has the possibility of having many significant advantages over other types of heat engines, it has not seen commercial success. Advantages include the possibility of extremely long operating life, high efficiency, zero maintenance, no need for lubrication and multi-fuel capability.

It is believed, however, that a 3 kWe FPSE solar concentrating dish for rural off-grid electric power supply could be a suitable application for an FPSE and this study forms part of this ultimate aim. In order to design an FPSE, however, a theoretical simulation model first needs to be developed and validated to be used for its design.

The limited availability of experimental data and high cost of attaining a laboratory FPSE unit necessitated the design and manufacture of an experimental FPSE that could produce experimental test results. These test results would be used to validate a theoretical simulation model that would be developed to design the desired 3 kWe unit.

The development of a linear electric generator that is being done at the Department of Electrical and Electronic Engineering at Stellenbosch University (Joubert *et al.*, 2012) also forms part of this effort.

The objectives of this study were to design and manufacture an experimentally testable FPSE, including a linear electric generator; to develop and validate a theoretical simulation model; to identify problem areas pertaining to its manufacture; and finally to assess the work undertaken, to lay out the groundwork for the future development of a 3 kWe FPSE suitable for incorporation in a solar Stirling dish power generator.

The literature study provided in Chapter 2 was used to identify the different theoretical simulation methods, to compare the different engine configurations, to determine basic performance parameters and to identify physical considerations that are unique to FPSEs. It was also used to provide a background on Stirling engines and to illustrate the advantages of an FPSE over a kinematic Stirling engine.

This led to the choice of a beta configuration FPSE, mostly because of its higher specific power. The theoretical simulation that was developed, is a combination of a third-order and dynamic analysis to allow it to be expanded into a fully descriptive model.

The theoretical simulation was presented in Chapter 3 and the simulation results were compared with experimental test results. The theoretical simulation applied the conservation of mass and energy equations for a one-dimensional dis-

cretised model of the engine. The assumption that there was no pressure drop in the working space negated the need for the application of the conservation of momentum equation. The omission of the conservation of momentum equation provided much shorter simulation times, in the order of 1 000 times. Rewriting the theoretical simulation model in C or FORTRAN should greatly improve the achieved simulation times of between 40 and 43 minutes.

The theoretical simulation model that was developed, provided satisfactory results. The pressure curve and motions of the piston and displacer were well predicted when compared to experimental test results. The use of higher Nusselt numbers for heat transfer relations produced greater accuracy in most cases. Higher accuracy was attained in the prediction of piston and displacer strokes, frequency, average pressure and hot and cold side temperatures. However, lower accuracy for increased Nusselt numbers was seen for the phase angle between the piston and displacer, as well as for the indicated power.

This is assumed to be true, only for the case at hand, however. Improved relations for heat transfer between the working space and wall should be developed to make the theoretical simulation model more generally applicable.

The design of the engine was provided in Chapter 4, as well as reasons for the redirection to the final design. The initial attempt at manufacturing an experimental engine was unsuccessful and many of the design challenges were mitigated by a redesign of the Beale B-10B demonstrator engine. A large scope of experimental test results was achieved by designing the engine for experimentation. The scope of experimental test results achieved was greater than generally available in the literature. Measurements include piston and displacer motions, hot side and cold side temperatures, working space pressure, electric generator output, as well as heat rejection via a water jacket.

Design knowledge of certain components such as flexure bearings and gas bearings was difficult to attain and had to be generated. A number of flexure bearings were manufacture and tested at the beginning stages of this study, but such development requires the dedication of an independent study. The development of the design knowledge of these components should be developed in parallel with engine design, as well as the design of the electric generator. In terms of the design of the engine and electric generator, the engine is the more complex of the two and the design should be centred around the engine.

Although the objectives of the design and manufacture of an experimentally testable FPSE were achieved, the inclusion of a linear electric generator was not. The electric generator and engine were not well matched. The engine parameters that the electric generator was designed for (that of the first experimental engine), were not achieved because of the redirection to the design based on the Beale B-10B demonstrator engine.

The manufacture of the engine did not pose any major difficulty. This was largely because no complicated heat exchangers or gas bearings were included in the design. The only major difficulty was the assembly of the electric generator. The attachment of the permanent magnets to the magnet holder necessitated the design and manufacture of an assembly jig. The jig provided a very effective solution that can be used for future assemblies, which has been a challenge in past attempts.

A parametric investigation was done in Section 4.6 to gain insight into the effect of input parameters on engine operation. Arguably the most interesting outcome was the prediction that a constant output power would be delivered at nearly a constant frequency over a range of piston loads. This investigation also showed that the design of an FPSE is very complex when compared to a kinematic Stirling engine. The motion of the moving parts are not constrained and a well designed engine and control system will be required to ensure safe operation. In a kinematic Stirling engine, the motion of the moving parts can only be influenced in terms of frequency. In an FPSE, the motion of moving parts can be influenced by frequency, stroke, phase between the moving parts, as well as the stability of moving parts. If contact between moving parts does occur, however, failure could become a great risk and be catastrophic.

This also adds to the advantage of FPSEs, however, since a well designed control system could take advantage of the fact that these parameters could be changed dynamically.

Collision of the displacer with both the piston and heater head end cap was present with most simulations and with experimental tests. The displacer used from the Beale B-10B engine seems to have a rod diameter that is too large. This large rod diameter causes the displacer to be very reactive, which made it very difficult to avoid contact on its upward and downward strokes. The variation of the displacer rod diameter provided interesting results in simulations, however. By decreasing the displacer diameter, contact with the piston was avoided.

It was also seen that a change in output power was predicted for changes in the displacer rod diameter, as well as changes in the piston and displacer masses and spring stiffnesses.

An accurate theoretical simulation model is, therefore, shown to be imperative to the design of an FPSE to predict the behaviour of moving parts, as well as predicting the outcomes of changes to a design. Careful design of an FPSE is not only required to design an optimised engine, but also required to design an engine that will function at all.

The experimental test setup was provided in Chapter 5 and the results of the experimental tests were provided in Chapter 6. The evaluation of the performance of the engine was not included as an objective, but instead left for future research.

The main purpose of this experimental engine was to provide a means of validating the theoretical simulation model and to provide a laboratory unit for further study and development. Experimental tests were conducted before the addition of the electric generator and subsequent to the addition of the electric generator. The experimental test results that were produced prior to the addition of the electric generator were used to validate the theoretical simulation.

These test results showed an indicated power of 0,659 W at a frequency of 10,99 Hz for hot side and cold side temperatures of 446,2 K and 305,4 K. Although the test results produced after the addition of the electric generator were discontinuous, the results produced an indicated power of between 0,138 W and 0,144 W for different loads on the electric generator, while the electrical output power ranged from 1,23 mWe to 1,79 mWe. These results were produced at a hot side temperature of about 675 K and a cold side temperature of about 298 K.

The displacer rod diameter is assumed to be the major cause of unavoidable collision of the displacer on its upward and downward strokes. This should be investigated, as well as the addition of a well matched electric generator so that differing piston loads can be applied. This would allow the verification of the prediction of the theoretical simulation model that constant output power will be delivered over a range of piston loads. The investigation of differing displacer rod diameters, will require the design of a smooth running piston and displacer that can seal effectively.

The objective to assess the work undertaken to lay out the groundwork for the future development of a 3 kWe FPSE was achieved in terms of providing a theoretical simulation model and the identification of the components that will have to be developed to realise this aim. The development of a 3 kWe FPSE will require many parties with specific knowledge. These parties will have to work in parallel and members of the design team will have to address the design of the engine itself, the design of flexure bearings and gas bearings, and the design of the electric generator and control system.

With respect to the control of the engine. It should be decided how the engine is to be controlled, i.e. will only the piston be controlled or the displacer as well, and how will this be achieved.

This study has met most of its objectives, although they differ from those that were set out originally. This study has provided the platform and direction of future study for the development of a 3 kWe FPSE and has shown that the design of an FPSE is a complicated undertaking.

# Appendices

## A. Calibration

This appendix starts by describing the methods used for calibrating the equipment and also how measurements were converted. The data logging equipment is then described, followed by the calibration of all the equipment described individually.

### A.1 Method

All measuring equipment and components that were calibrated produced a linear relationship between the inputs and outputs. Each calibration consisted of plotting a set of known values on the  $x$ -axis, referred to as the inputs, and values that were measured from the measuring device or component that were plotted on the  $y$ -axis, termed the outputs. A linear curve fit (method of least squares) was then performed to obtain the relationship between the inputs and outputs as follows:

$$y_{output} = a \cdot y_{input} + b \quad (\text{A.1})$$

Now, in order to determine the actual value when taking a reading, Equation A.1 is rearranged and transformed as follows:

$$y_{input} = \frac{(y_{output} - b)}{a} \quad (\text{A.2})$$

$$y_{actual} = \frac{(y_{measured} - b)}{a} \quad (\text{A.3})$$

Here,  $y_{measured}$  is the measured value, which is converted to give  $y_{actual}$ , the correct value in the desired units.

All measuring equipment and components have linear characteristics and the coefficient of determination ( $R^2$ ) was calculated in each case to substantiate this. The coefficient of determination is a measure of the goodness of fit, which in this case always was a linear fit performed by the method of least squares.

### A.2 Data-logging equipment

A National Instruments cDAQ-9172 chassis was used together with data cards from National Instruments to read the different output signals. The data cards used, as well as the signals they were used to measure, are given in Table A.1.

The compression springs were included in Table A.1, since laser 1 was used to calibrate them as explained in Section A.3 (page A.2). It should also be noted that experimental testing makes use of the NI 9215 data card (greater resolution) to measure signals for pressure, laser 1 and laser 2 instead of the NI 9221 data card. The NI 9215 was acquired subsequent to when calibration was done.



**Table A.1:** Data-logging card details (National Instruments).

	<b>NI 9221</b>	<b>NI 9215</b>	<b>NI 9213</b>
Description	$\pm 60$ V, 12-bit analogue input module	$\pm 10$ V, 16-bit analogue input module	24-bit ADC (up to 0,02 °C measurement sensitivity) thermocouple input module
Signals measured	Pressure (before experimental testing), laser 1, laser 2, compression springs	Pressure (after experimental testing)	$T_{hot}$ , $T_{cold}$ , $T_{w\_in}$ , $T_{w\_out}$ , $T_{wall\_1}$ , $T_{wall\_2}$ , $T_{wall\_3}$ , $T_{wall\_4}$

### A.3 Compression springs

Two similar rigs were designed and manufactured to calibrate the piston compression spring and displacer compression spring respectively. The rig for the displacer compression spring is shown in Figure A.1. The only difference between the rig for the piston compression spring and that for the displacer compression spring is the plunger rod diameter and hence the hole diameter in the base. The diameters are different since the spring diameters are different. However, the length of both springs was the same (106 mm).

Now, as seen in Figure A.1, a plunger protrudes through the base and is free to run in the vertical direction. The plunger is held up by a compression spring that sits between the head of the plunger and the top of the base. Weights are placed on top of the head of the plunger to cause a deflection of the spring.

The laser displacement sensor is then aimed at the bottom of the plunger that protrudes through the base. The length of the plunger rod is represented by  $L_{plunger}$  (not shown), while  $L_{base}$  must be measured after the rig has been set up, since it depends on where the laser is situated. The plunger and base were designed so that a vernier caliper could easily be used to measure the spring length ( $x_1$ ). The spring length can also be obtained by relating it to the distance measured by the laser ( $x_2$ ), as follows:

$$x_1 = L_{plunger} + x_2 - L_{base} \quad (\text{A.4})$$

Although this was intended to measure both  $x_1$  and  $x_2$ , it was found to be inconvenient when weights with a large diameter were used that impeded the vernier caliper. Therefore only the laser (laser 1) was used to measure the deflection of the springs. The laser was calibrated beforehand.

### A.2

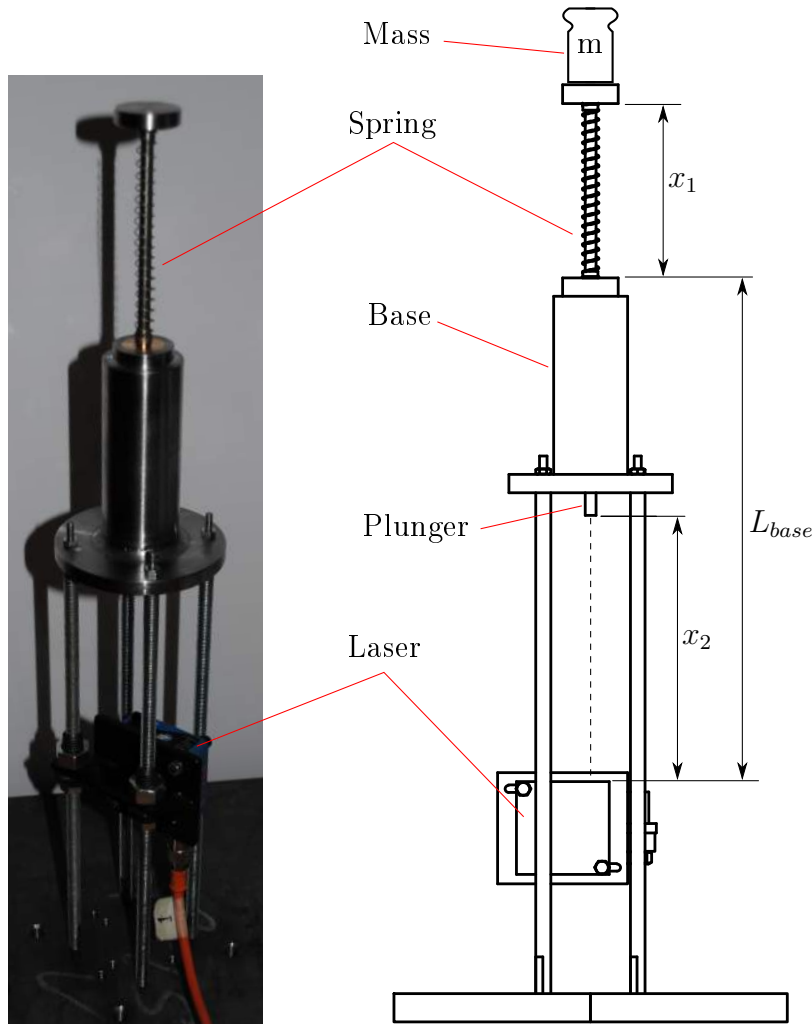


**Figure A.1:** Spring calibration rig.

Now, with regard to the calibration of the springs, the input was taken as the weight in Newtons of the weights placed on the plunger, as well as the weight of the plunger itself, represented by  $F_{mass}$  and calculated as follows:

$$y_{input} = g_{grav}(m_{weights} + m_{pluger}) \quad (\text{A.5})$$

The weights used were calibrated and the gravitational acceleration ( $g_{grav}$ ) was taken as  $9,81 \text{ m/s}^2$ .

The output was taken as the spring length:

$$y_{output} = x_1 \quad (\text{A.6})$$

### A.3

The calibration curves for the piston and displacer compression springs are shown in Figure A.2 and A.3 respectively. The coefficients of the fitted curves are given in Table A.2.

These results produced the following (as used in Chapter 3):

$$Fk_p = k_p(x_p - x_{p0}) \quad (\text{A.7})$$

$$Fk_d = k_d(x_d - x_{d0}) \quad (\text{A.8})$$

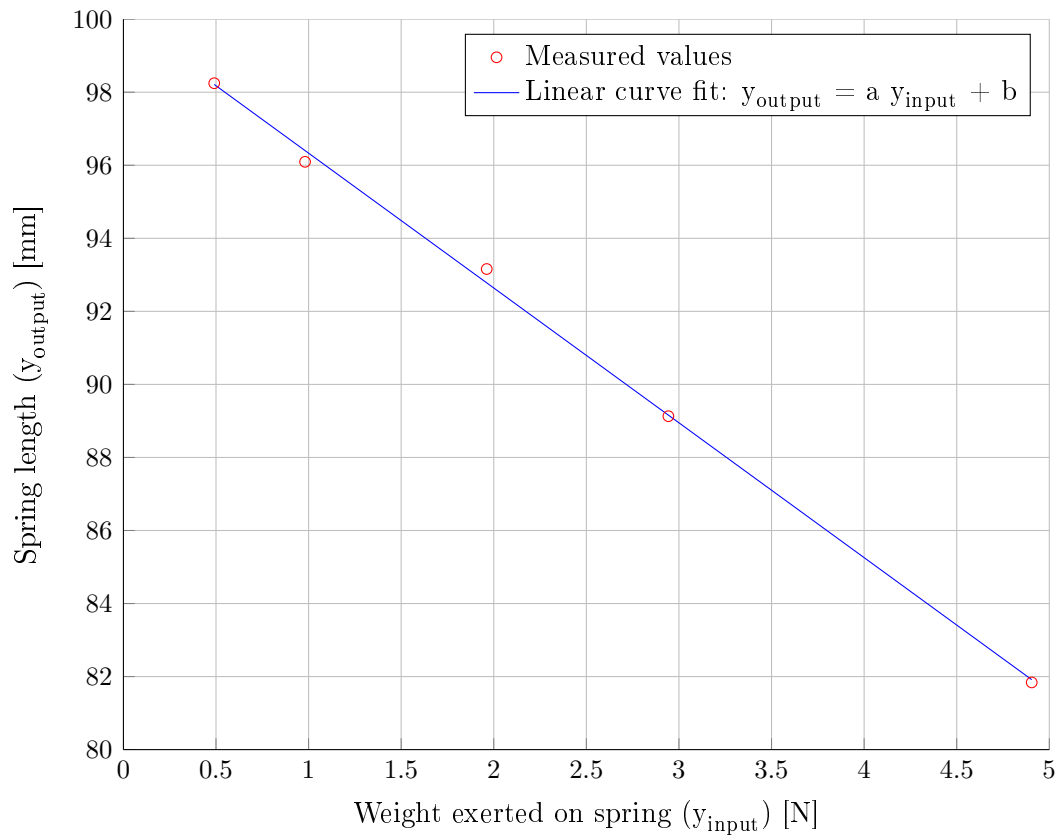


**Figure A.2:** Calibration curve for piston compression spring.

**Table A.2:** Linear curve fit results for compression spring calibration.

	<b>a [mm/N]</b>	<b>b [mm]</b>	<b>R<sup>2</sup></b>
Piston compression spring	-3,691546	100,0229	0,9985373
Displacer compression spring	-6,140086	96,77493	0,9967283

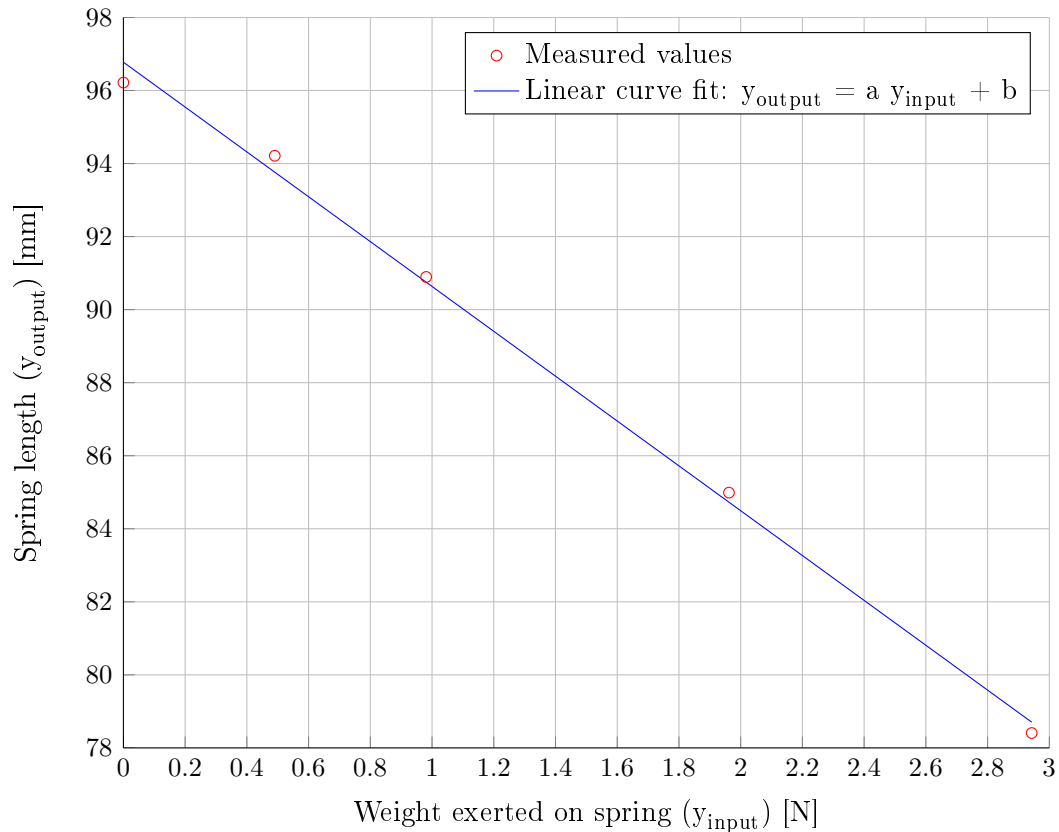


**Figure A.3:** Calibration curve for displacer compression spring.

With  $k_p$  and  $k_d$  calculated to be the following [N/m]:

$$k_p = 270,8892 \quad (\text{A.9})$$

$$k_d = 162,8642 \quad (\text{A.10})$$

#### A.4 Laser displacement sensors

The laser sensors that were used can measure in a range of between 50 mm and 100 mm away from the laser. The intention initially was to use differing weights on the plunger to obtain a distribution of points in this range, but this was found to be inconvenient. Instead, the plunger was clamped manually at different positions. The variables referred to in this section remain the same as in Figure A.1.

The laser produced an output voltage of between 0 V and 10 V. Inputs ( $x_2$ ) were obtained by measuring  $x_1$  with a vernier caliper and relating its position by rearranging Equation A.4:

$$x_2 = x_1 + L_{base} - L_{plunger} \quad (\text{A.11})$$

#### A.5

The calibration curves for laser 1 (used to measure displacer motion) and laser 2 (used to measure piston motion) are shown in Figures A.4 and A.5 respectively. The coefficients of the fitted curves are given in Table A.3.

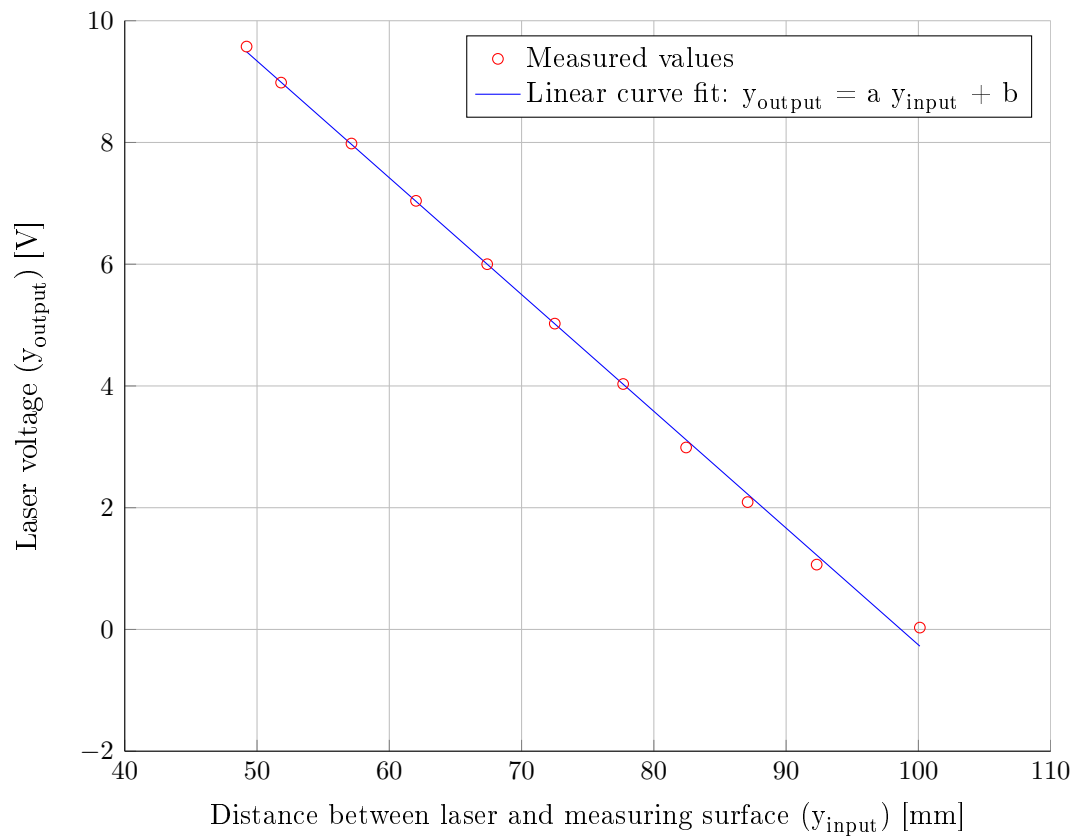


**Figure A.4:** Calibration curve for laser 1.

**Table A.3:** Linear curve fit results for laser 1 and laser 2 calibration.

	<b>a [V/mm]</b>	<b>b [V]</b>	<b>R<sup>2</sup></b>
laser 1	-0,1918363	18,93033	0,9984857
laser 2	-0,1835365	18,09776	0,9992317

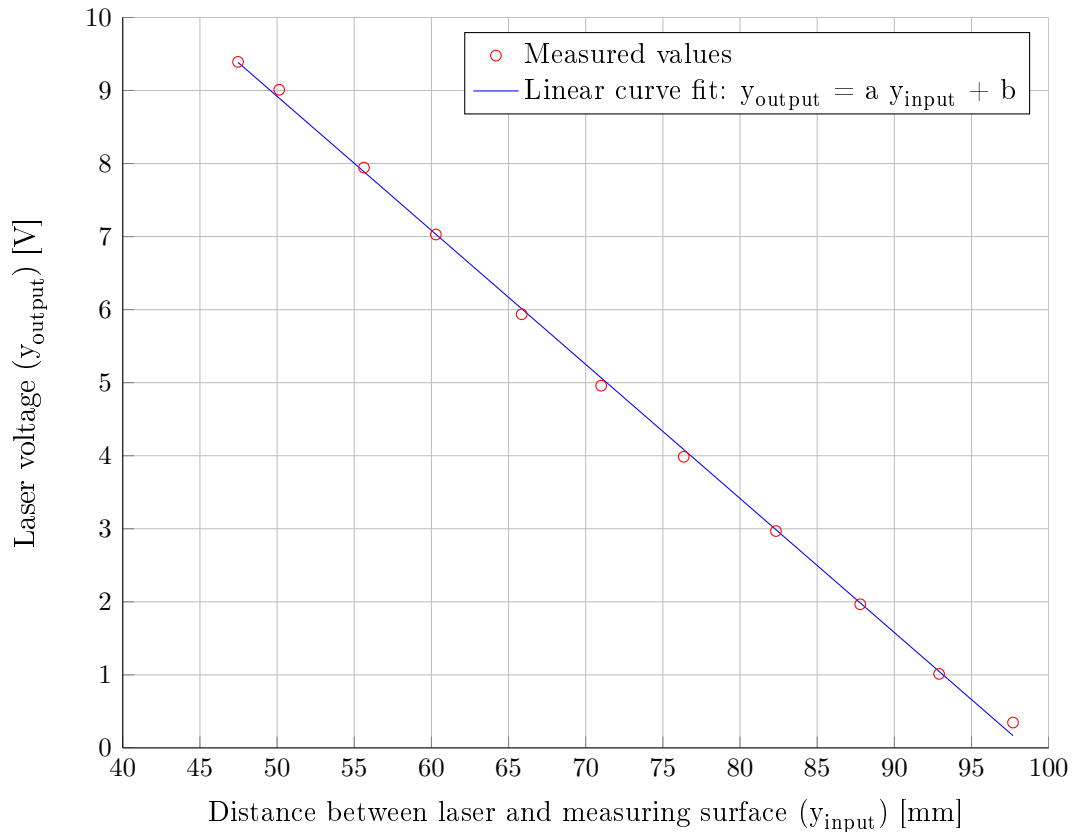


**Figure A.5:** Calibration curve for laser 2.

## A.5 Pressure sensor

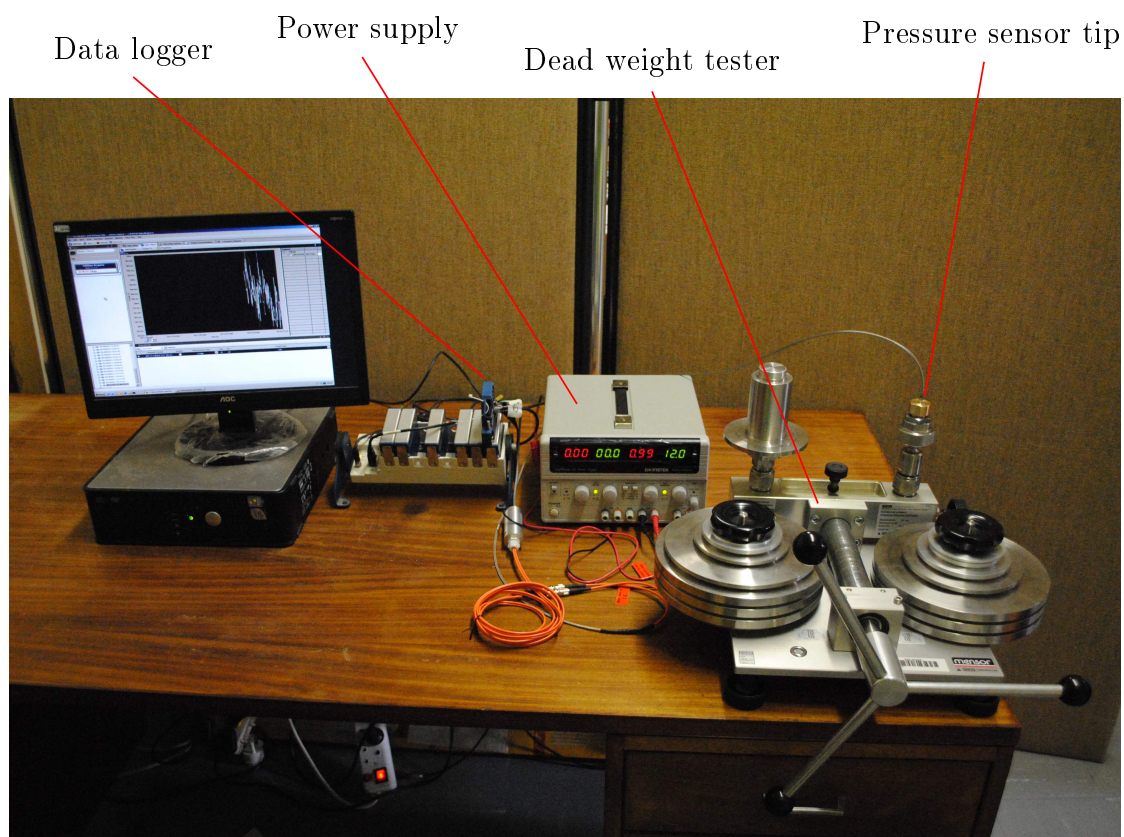
The pressure sensor used was calibrated with a dead weight tester. The dead weight tester was a Wika Pressure Balance CPB 3000 (S/N: 30285), calibrated by Wika prior to purchase in November 2012. The specifications of the pressure sensor are given in Table A.4 and the setup is shown in Figure A.6.

Although the pressure sensor is designed to measure differential pressure, it can also be connected to measure static pressure by connecting a potentiometer between its diagnostic wire and the ground. When calibrated statically, the minimum pressure that can be read is dependent on the potentiometer setting and will relate to 0,52 V. For pressures below this minimum pressure, the voltage will remain at 0,52 V, while pressures above this minimum pressure will produce a linear relation to voltage, as shown by the static calibration in Figure A.7. The potentiometer also determines the gradient of this linear relationship.

Although the sensor voltage does not drop below 0,52 V during static calibration, this is possible during dynamic operation. More generally, the pressure sensor

**Table A.4:** Pressure sensor specifications.

Manufacturer	Optrand
Model	AutoPSI-S
Type	Fibre optic
Model number	C12394-4
Pressure range	0 to 7 bar (0 to 700 kPa)
Response frequency	0,1 Hz to 20 kHz
Non-linearity and hysteresis	$\pm 0,5\%$ of full scale (non-combustion conditions, constant temperature), $\pm 1\%$ of full scale (combustion conditions, varying temperature within one combustion cycle).

**Figure A.6:** Pressure calibration setup.

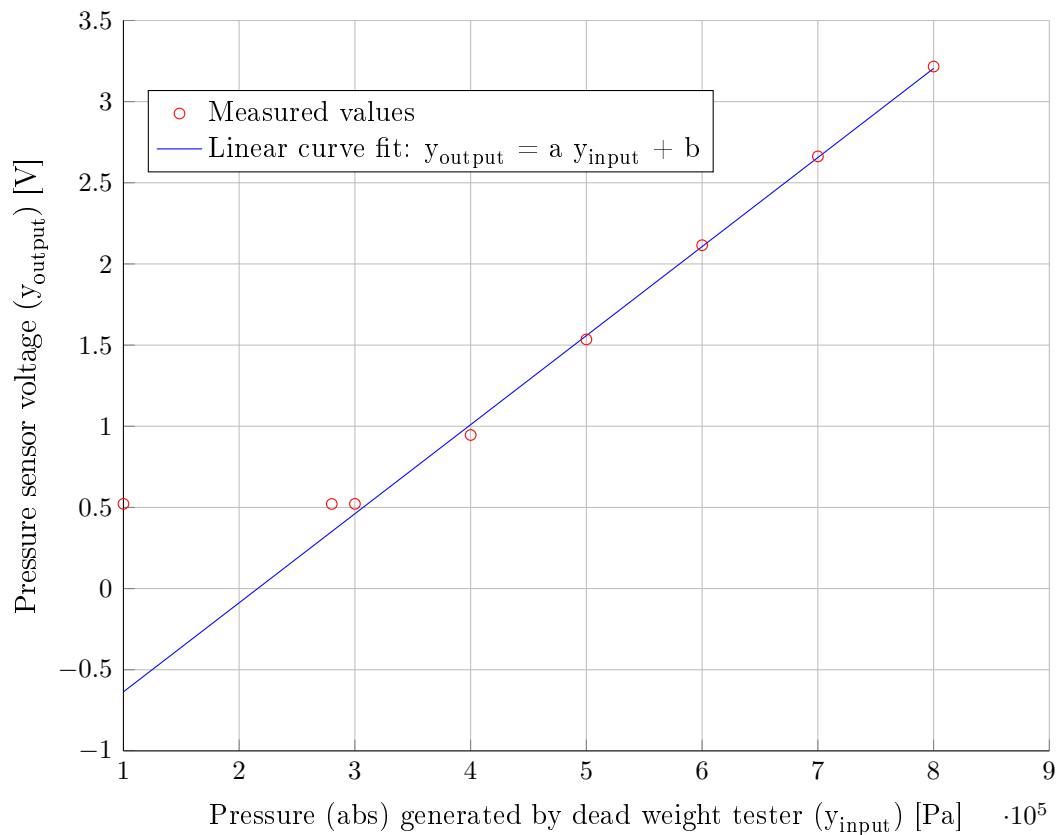


**Figure A.7:** Calibration curve for pressure sensor.

will react to any pressure change, be it positive or negative, and will follow the linear relation determined by the static calibration. The calibration of the sensor is thus done only to determine the gradient of the linear relationship.

A vacuum test was done in order to verify the characteristics of the sensor. As shown in Figure A.8, a PVC rod was inserted into the bottom of the fitting used for calibration with the dead weight tester. The pressure sensor was inserted at the top of the fitting as usual (not shown). The PVC rod did not create an air-tight seal and so the internal pressure settled at atmospheric pressure subsequent to the insertion of the PVC rod.

The PVC rod was then rapidly pulled out of the fitting to cause the pressure first to drop below atmospheric and then to jump back to atmospheric as the rod exited the fitting. The results shown in Figure A.9 show how the voltage of the pressure sensor dropped below 0,52 V as the PVC rod was pulled out and the voltage then subsequently returned to near 0,52 V as the rod exited the fitting. A similar test was done for verification, with the PVC rod being inserted rapidly to



produce the expected results.

Owing to this characteristic of the pressure sensor, the calibration curve was modified as follows:

$$y_{output} = a \cdot y_{input} + b \quad (\text{A.12})$$

$$b = V_{atm} - a \cdot p_{atm} \quad (\text{A.13})$$

The atmospheric pressure is represented by  $p_{atm}$ , while the voltage at atmospheric pressure is represented by  $V_{atm}$ .

The static calibration of the pressure sensor is given in Figure A.7, and the coefficients of the fitted curve are given in Table A.5.

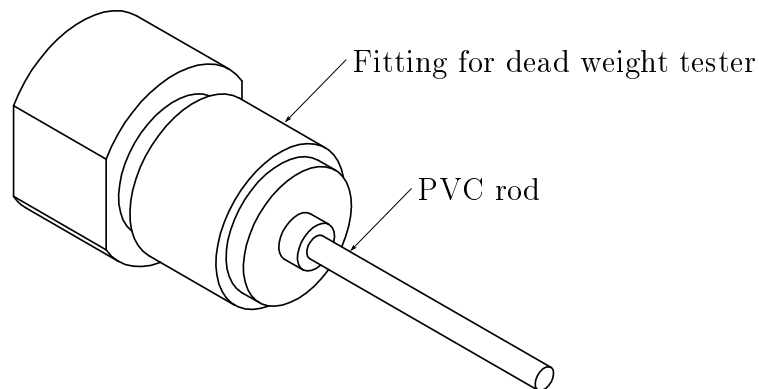


**Figure A.8:** Vacuum test setup.

**Table A.5:** Linear curve fit results for pressure sensor calibration.

	<b>a [V/Pa]</b>	<b>b [V]</b>	<b>R<sup>2</sup></b>
Pressure sensor	5,485996e-06	-1,184759	0,9983826

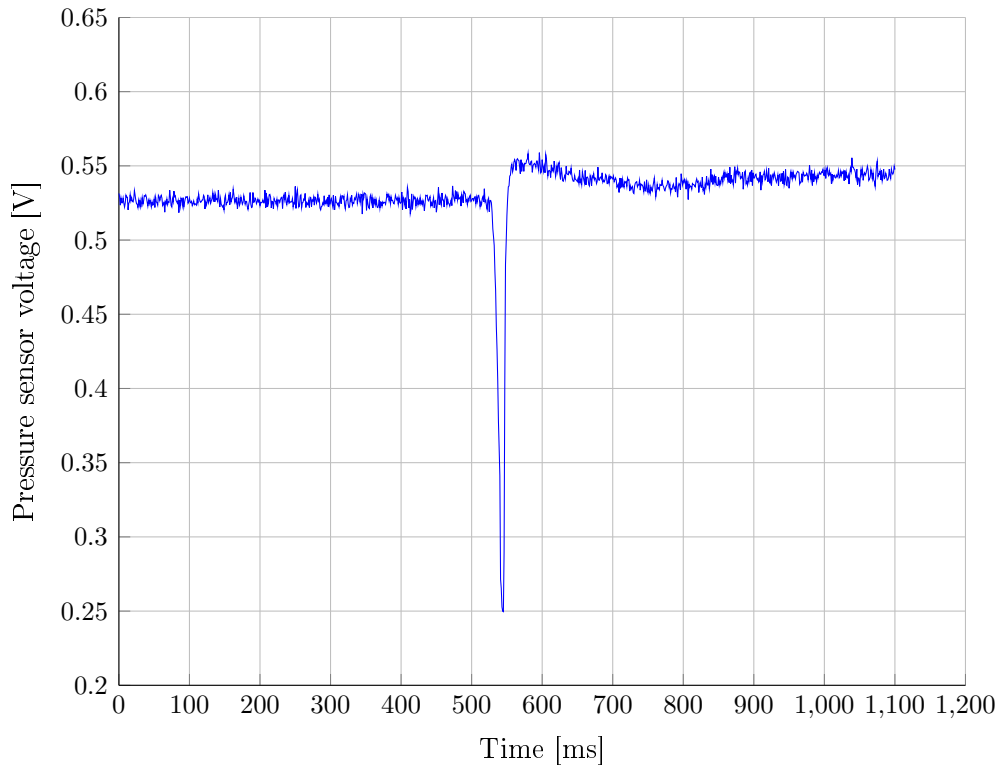


**Figure A.9:** Vacuum test results.

## A.6 Multimeter

A multimeter was used to measure the electric resistance of the variable resistor used as a load for the electric generator (see Chapter 5).

Resistors with a 1% tolerance were used as a reference for electrical resistance. The electrical resistance of each resistor was then measured by the multimeter and plotted against the electrical resistance of the resistors, as shown in Figure A.10. The coefficients of the fitted curve are given in Table A.6.

**Table A.6:** Multimeter calibration.

	<b>a</b> [ $\Omega/\Omega$ ]	<b>b</b> [ $\Omega$ ]	<b>R</b> <sup>2</sup>
Multimeter	1,001310	0,08137785	0,9999400

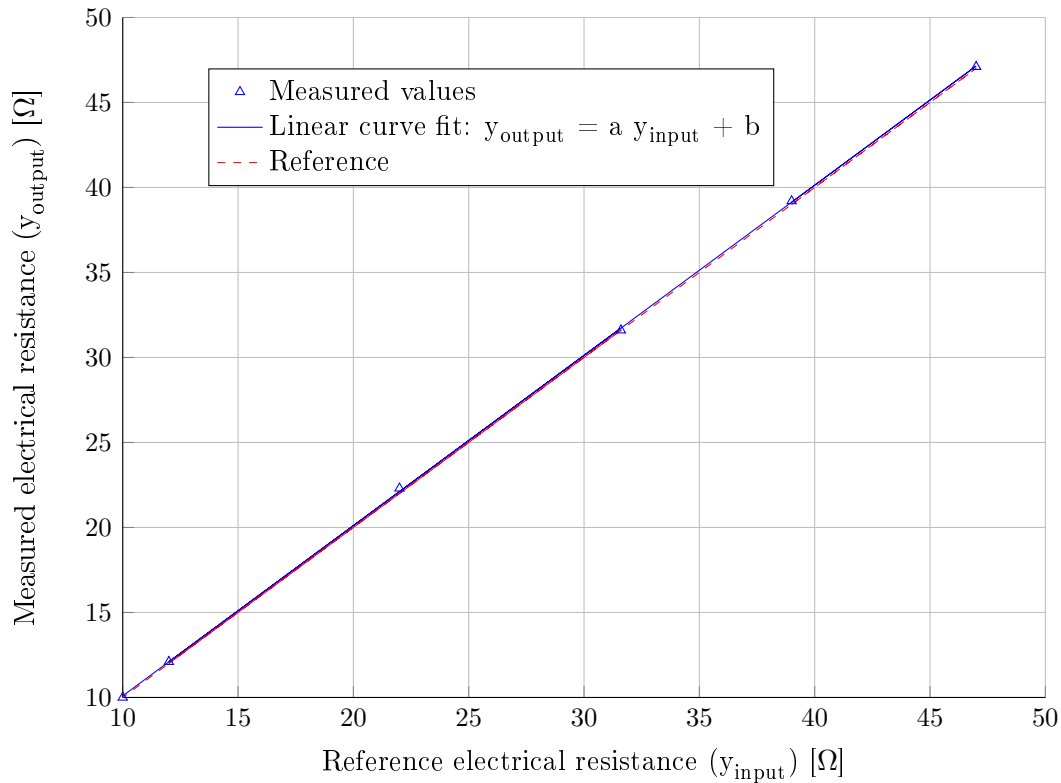


**Figure A.10:** Calibration curve for multimeter.

## A.7 Thermocouples

All tests were performed by allowing ample time for the temperatures to reach equilibrium. Equilibrium was verified by recording the temperature change over a 1 min interval.

### A.7.1 Calibration equipment

Three sets of calibration equipment were used to generate reference temperatures. The capabilities of each are summarised in Table A.7. Here,  $T_{atm}$  refers to the atmospheric temperature.

The Fluke field metrology well was used to calibrate the low-temperature thermocouple probes (up to 423,15 K), the JMM thermal well was used to calibrate all the wire thermocouples (up to 773,15 K) and the aluminium billet was used to calibrate the high-temperature probes (up to 773,15 K).

The aluminium billet was designed and manufactured to allow for high temperature calibration with a shorter settling time than the JMM thermal well. The JMM thermal well was used for the wire thermocouples, since a larger number could be calibrated at the same time.

**Table A.7:** Temperature-generating equipment.

Equipment description	Temperature range [K]	Thermocouples
JMM thermal well (S/N: 4736)	$T_{atm} \rightarrow 1373,15$	$T_{wall\_1}$ , $T_{wall\_2}$ , $T_{wall\_3}$ and $T_{wall\_4}$
Aluminium billet (self-designed and manufactured)	$T_{atm} \rightarrow 773,15$	$T_{hot}$
Fluke 9142 field metrology well (S/N: B29291)	$248,15 \rightarrow 423,15$	$T_{cold}$ , $T_{w\_in}$ and $T_{w\_out}$

An illustration of the aluminium billet is provided in Figure A.11. On one side of the aluminium billet there is a hole (10 mm diameter) for an electric heating element (500 W Watlow St. Louis Firerod), and at the opposite end there are two holes, one hole (1,5 mm diameter) for the thermocouple being calibrated (test specimen) and one hole (3,0 mm diameter) for the reference it is being calibrated against. All holes are 60 mm in depth and the length of the aluminium billet is 80 mm.

In order to create a situation similar to a thermal well-type calibrating device, where a billet is thermally isolated from the atmosphere by insulating it, the aluminium billet was completely surrounded by ceramic wool and placed inside a pipe section (150 mm length, 108 mm inner diameter). This is why the aluminium billet floats at the centre of the pipe section, as is suggested by Figure A.11. The diameter of the aluminium billet is 61 mm, with both off-centre holes drilled 9,79 mm apart at a radius of 27 mm.

### A.7.2 Temperature references

The devices used for temperature references comprised a platinum resistance thermometer and a 3,0 mm K-type thermocouple probe. Both of these sub-standards were calibrated in a laboratory and the details are given in Table A.8. The platinum resistance thermometer was used as the reference for the Fluke field metrology well, while the K-type thermocouple probe was used as the reference for both the aluminium billet and the JMM thermal well.

### A.7.3 Results

The calibration curves for thermocouples calibrated with the Fluke field metrology well are shown in Figure A.12. The calibration curve for the thermocouple calibrated with the aluminium billet is given in Figure A.13, while the calibration curves for the thermocouples calibrated with the JMM thermal well are given in Figure A.14. The coefficients of the fitted curves are given in Table A.9.

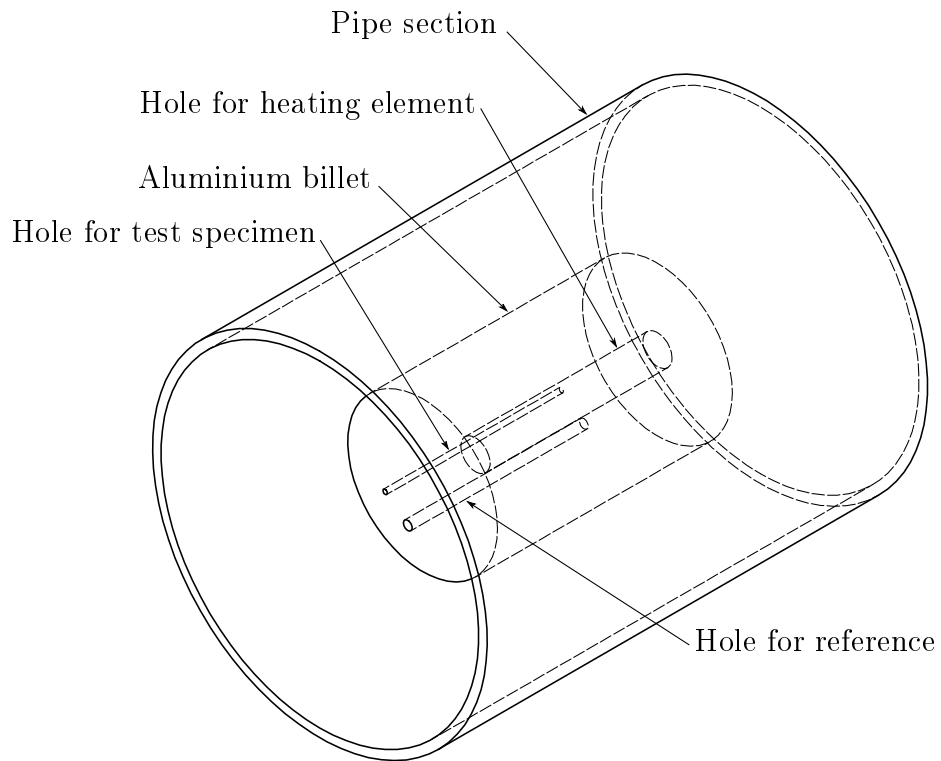


**Figure A.11:** Aluminium billet calibrating device.

**Table A.8:** Sub-standard calibration.

Device	Calibrated temperature range [K]	Laboratory	Date
ISOTECH platinum resistance thermometer (S/N: 191069)	273,15 → 573,15	Rapid instrumentation cc (SANAS-accredited laboratory number 366)	04/02/2013, certificate number: RAP15738
Temperature Controls (PTY) LTD, 3mm K-Type thermocouple probe (S/N: CT22303/1)	373,15 → 873,15	Calibration certificate was issued using equipment certified by a SANAS laboratory.	11/12/2012, certificate number: 12L007

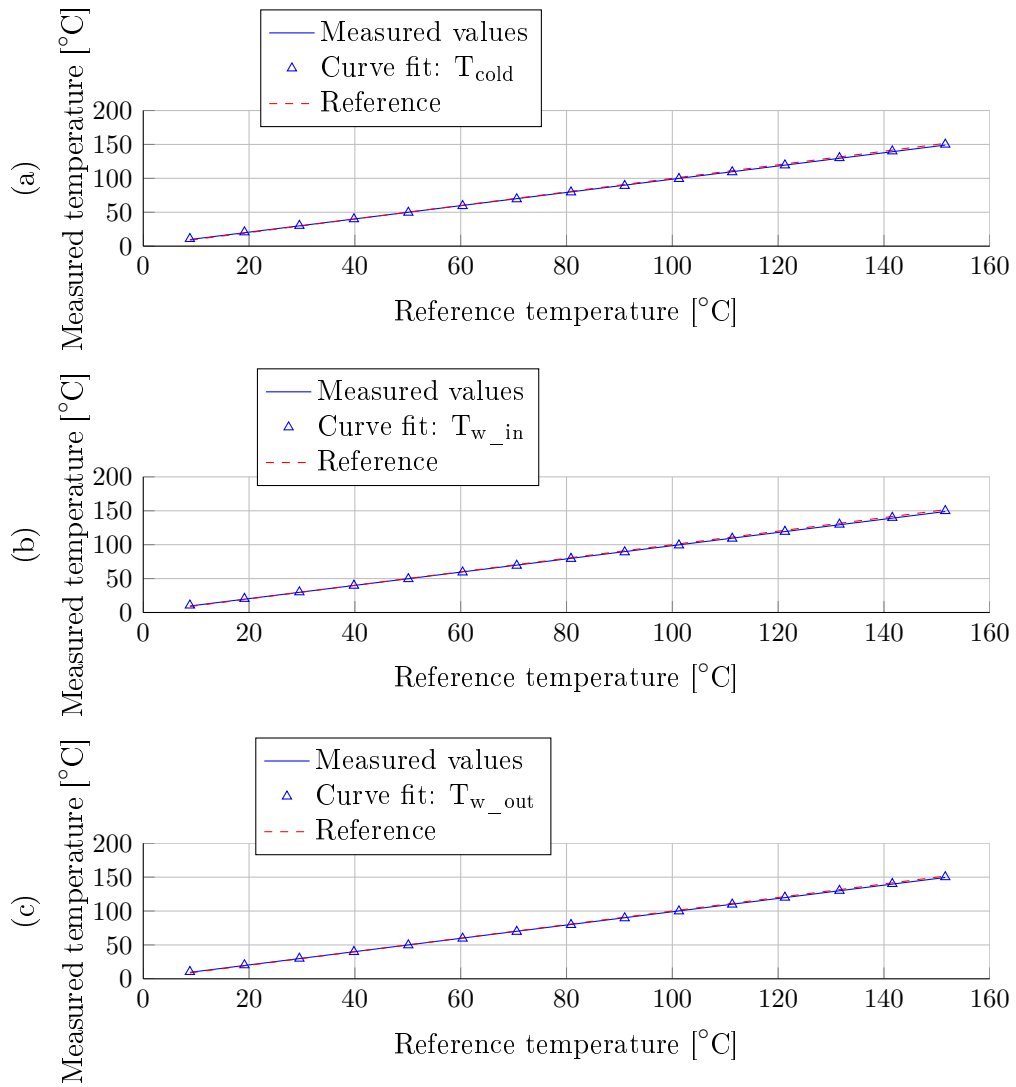


**Figure A.12:** Calibration curves for thermocouples calibrated with Fluke field metrology well. (a)  $T_{cold}$ , (b)  $T_{w\_in}$ , (c)  $T_{w\_out}$ .

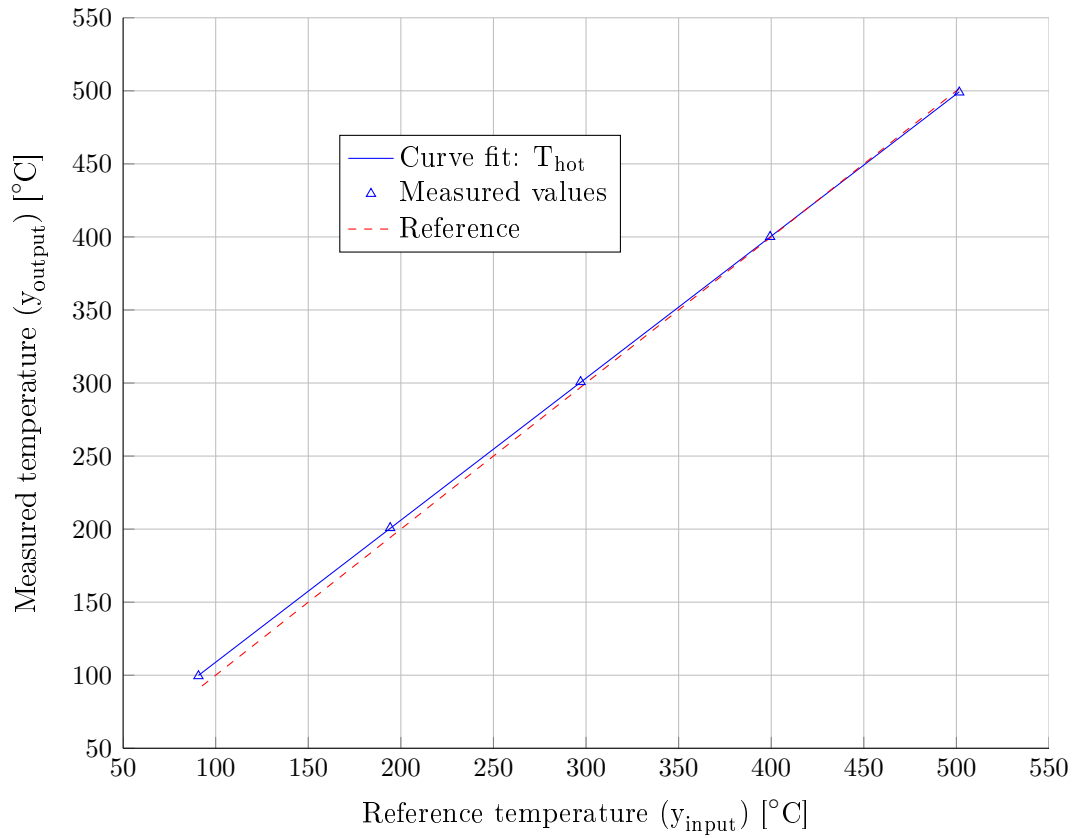


**Figure A.13:** Calibration curve for  $T_{hot}$ .

**Table A.9:** Thermocouple calibration.

	<b>a</b> [°C/°C]	<b>b</b> [°C]	<b>R<sup>2</sup></b>
$T_{cold}$	0,9754539	1,168219	0,9997765
$T_{w\_in}$	0,9758301	0,9712489	0,9998008
$T_{w\_out}$	0,9799413	0,9464574	0,9998871
$T_{hot}$	0,9722297	11,67225	0,9999957
$T_{wall\_1}$	0,9730552	11,67225	0,9999607
$T_{wall\_2}$	0,9746303	11,27551	0,9999856
$T_{wall\_3}$	0,9736718	11,02107	0,9999509
$T_{wall\_4}$	0,9732761	11,03132	0,9999563

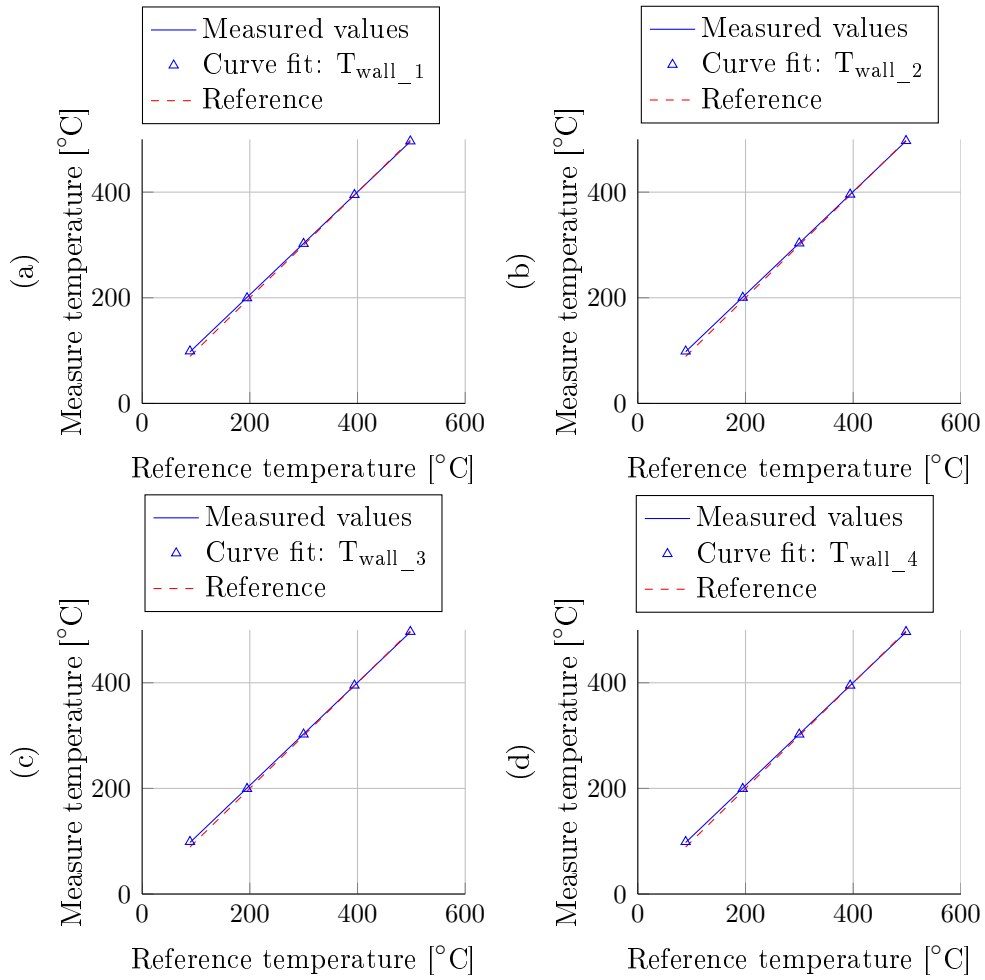


**Figure A.14:** Calibration curves for thermocouples calibrated with JMM thermal well. (a)  $T_{wall\_1}$ , (b)  $T_{wall\_2}$ , (c)  $T_{wall\_3}$ , (d)  $T_{wall\_4}$ .



## B. Theoretical simulation equations

This appendix shows how the differential equations for the conservation of mass, momentum and energy were taken from first principles and simplified. It is then shown how the differential equations were discretised, barring the conservation of momentum equation, which will be shown to fall away. The discretised equations form the expressions used in the theoretical simulation model described in Chapter 3.

The definitions of the conservation of mass, momentum and energy equations are taken from Urieli (1977).

### B.1 Fundamental equations

Consider the arbitrary stationary control volume given in Figure B.1. The Eulerian description is followed and the control volume is defined as stationary by having one point of the control surface that does not change position, i.e.  $v = 0$ . All other points on the control surface may move position and thus the control volume can do work on the environment or work can be done on it by the environment. Work is represented by  $W$  and heat that is transferred to the control volume across the control surface is represented by  $Q$ . An over-line indicates a vector.

Matter enters the control volume through the control surface. The divergence theorem is used in order to describe the effect that the transport of a property

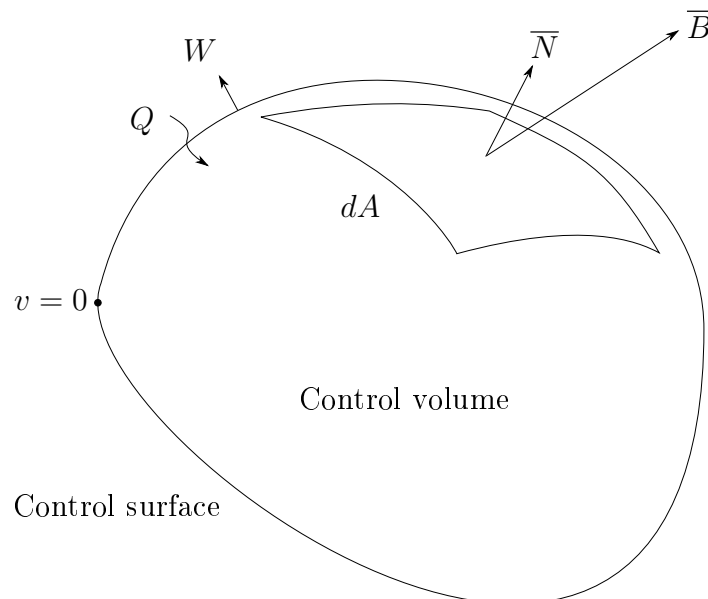


**Figure B.1:** Control volume and control surface illustration.

into a control volume has on that property contained in the control volume.

The divergence theorem states that the volume integral of the divergence of a vector  $\bar{B}$  is equal to the integral of the net outward flux of this vector over the control surface. Flux is defined as time rate per area. The control surface is a closed area that encompasses the control volume. The divergence theorem is mathematically expressed as follows:

$$\int_V (\nabla \cdot \bar{B}) dV = \oint_A (\bar{B} \cdot \bar{N}) dA \quad (\text{B.1})$$

This can be expressed more intuitively as follows: the rate of decrease of  $\bar{B}$  contained in a control volume is equal to the net flow of  $\bar{B}$  out of the control volume through the control surface.

Now, with regard to describing flow, it can be described by the laws of the conservation of mass, the conservation of momentum and the conservation of energy. The description of each law is provided below as each is derived from first principles. Since these laws are defined in the Lagrangian description (fixed mass), they are expressed in the Eulerian description by means of applying the Reynolds transport theorem. The definition of each law is given in the Eulerian description, i.e. after the application of the Reynolds transport theorem.

Lastly, the working fluid is air and is assumed to be an ideal gas.

### B.1.1 Mass

The conservation of mass is based on the principle that matter cannot be created or destroyed.

$$-\left\{ \begin{array}{l} \text{Rate of increase of mass in} \\ \text{the control volume} \end{array} \right\} = \left\{ \begin{array}{l} \text{Net rate of mass flow out of} \\ \text{the control volume through} \\ \text{the control surface} \end{array} \right\}$$

$$-\frac{\partial}{\partial t} \int \rho dV = \oint (\rho \bar{v}) \cdot \bar{N} dA \quad (\text{B.2})$$

$$\rho \bar{v} = \bar{g} \quad (\text{B.3})$$

$$\frac{\partial}{\partial t} \int \rho dV + \oint (\bar{g} \cdot \bar{N}) dA = 0 \quad (\text{B.4})$$

Applying the divergence theorem to Equation B.4 leads to the following:

$$\frac{\partial}{\partial t} \int \rho dV + \int (\nabla \cdot \bar{g}) dV = 0 \quad (\text{B.5})$$

Integrating and reducing this equation to the one-dimensional case in terms of  $x$  we get the following:

## B.2

$$\frac{\partial}{\partial t}(\rho V) + V \frac{\partial g}{\partial x} = 0 \quad (\text{B.6})$$

$$\frac{\partial m}{\partial t} + V \frac{\partial g}{\partial x} = 0 \quad (\text{B.7})$$

### B.1.2 Momentum

The conservation of momentum is based on Newton's second law of motion, which states that the rate of change of momentum of a particle is equal to the vector sum of the forces acting on that particle. If there is no net force acting on that particle, the momentum will not change and hence is conserved.

The momentum equation falls out, as will be shown, but its derivation is provided here for completeness and for future attempts to develop the code.

$$\begin{aligned} & \left\{ \begin{array}{l} \text{Rate of increase of momen-} \\ \text{tum in the control volume} \end{array} \right\} = \\ & - \left\{ \begin{array}{l} \text{Net rate of momentum trans-} \\ \text{ported out of the control volume} \\ \text{through the control surface} \end{array} \right\} + \left\{ \begin{array}{l} \text{Net force acting on the} \\ \text{control surface of the} \\ \text{control volume} \end{array} \right\} \\ & \frac{\partial}{\partial t} \int \bar{g} dV = - \oint (\bar{g}\bar{v}) \cdot \bar{N} dA + \left( - \oint p \cdot \bar{N} dA - \bar{F} \right) \end{aligned} \quad (\text{B.8})$$

$$\bar{v} = \bar{g}\nu \quad (\text{B.9})$$

$$\frac{\partial}{\partial t} \int \bar{g} dV + \oint \bar{g}(\bar{g}\nu) \cdot \bar{N} dA + \oint p \cdot \bar{N} dA + \bar{F} = 0 \quad (\text{B.10})$$

After applying the divergence theorem:

$$\frac{\partial}{\partial t} \int \bar{g} dV + \int (\nabla \cdot (\bar{g}^2\nu)) dV + \int (\nabla \cdot p) dV + \bar{F} = 0 \quad (\text{B.11})$$

Integrating and reducing this equation to the one-dimensional case in terms of  $x$  we get the following:

$$\frac{\partial}{\partial t}(g_x V) + V \frac{\partial}{\partial x}(g_x^2 \nu) + V \frac{\partial p}{\partial x} + F_x = 0 \quad (\text{B.12})$$

As will be shown in Section B.1.3, if the kinetic energy is taken as negligible with regard to the internal energy of the working fluid, the momentum equation reduces to the following:

$$V \frac{\partial p}{\partial x} + F_x = 0 \quad (\text{B.13})$$

If the pressure drop due to friction is also assumed to be negligible, as is assumed here, the momentum equation falls out completely.

## B.3

### B.1.3 Energy

The conservation of energy principle is based on the first law of thermodynamics, which states that energy cannot be created or destroyed.

This section firstly derives the equation for the conservation of energy from the assumption that the kinetic energy of the working fluid is not negligible with regard to its internal energy. Another derivation is then done on the assumption that the kinetic energy of the working fluid is negligible with regard to its internal energy. These two derivations are then compared and show the effect on the equation for the conservation of momentum. This was also outlined by Urieli (1977). However, the potential energy of the working fluid is always neglected.

$$\left\{ \begin{array}{l} \text{Rate of increase of energy in} \\ \text{the control volume} \end{array} \right\} =$$

$$- \left\{ \begin{array}{l} \text{Net rate of energy transported} \\ \text{out of the control volume through} \\ \text{the control surface} \end{array} \right\} - \left\{ \begin{array}{l} \text{Net flow work done in moving the} \\ \text{working fluid out of the control} \\ \text{volume through the control sur-} \\ \text{face} \end{array} \right\} +$$

$$\left\{ \begin{array}{l} \text{Rate of heat transfer to the} \\ \text{the control volume through} \\ \text{the control surface} \end{array} \right\} - \left\{ \begin{array}{l} \text{Rate of boundary work done} \\ \text{by the control volume on} \\ \text{the environment} \end{array} \right\}$$

$$\frac{\partial}{\partial t} \int \left( u + \frac{1}{2} \bar{v}^2 \right) \rho dV = - \oint \left( u + \frac{1}{2} \bar{v}^2 \right) \rho \bar{v} \cdot \bar{N} dA - \oint (p \bar{v}) \cdot \bar{N} dA + \frac{dQ}{dt} - \frac{dW}{dt} \quad (\text{B.14})$$

**Including kinetic energy of the working fluid**

$$\bar{v} = \bar{g}\nu \quad (\text{B.15})$$

$$\frac{\partial}{\partial t} \int \left( u + \frac{1}{2} (\bar{g}\nu)^2 \right) \rho dV = - \oint \left( u + \frac{1}{2} (\bar{g}\nu)^2 \right) \bar{g} \cdot \bar{N} dA - \oint (p(\bar{g}\nu)) \cdot \bar{N} dA + \frac{dQ}{dt} - \frac{dW}{dt} \quad (\text{B.16})$$

$$\frac{\partial}{\partial t} \int u \rho dV + \frac{\partial}{\partial t} \int \frac{1}{2} \bar{g}^2 \nu dV = - \oint \left( (u + p\nu) + \frac{1}{2} (\bar{g}\nu)^2 \right) \bar{g} \cdot \bar{N} dA + \frac{dQ}{dt} - \frac{dW}{dt} \quad (\text{B.17})$$

The relationship between the specific enthalpy and the specific internal energy of the working fluid is expressed as follows:

$$h = u + p\nu \quad (\text{B.18})$$

## B.4

Substituting this relationship and multiplying out certain terms we get:

$$\frac{\partial}{\partial t} \int u \rho dV + \frac{\partial}{\partial t} \int \frac{1}{2} \bar{g}^2 \nu dV = - \oint \left( h \bar{g} + \frac{1}{2} \bar{g}^3 \nu^2 \right) \cdot \bar{N} dA + \frac{dQ}{dt} - \frac{dW}{dt} \quad (\text{B.19})$$

Now, with regard to the internal energy and enthalpy:

$$u - u_{ref} = c_v (T - T_{ref}) \quad (\text{B.20})$$

$$u_{ref} = 0 \text{ at } T_{ref} = 0$$

$$\therefore u = c_v T \quad (\text{B.21})$$

$$h - h_{ref} = c_p (T - T_{ref}) \quad (\text{B.22})$$

$$h_{ref} = 0 \text{ at } T_{ref} = 0$$

$$\therefore h = c_p T \quad (\text{B.23})$$

$$\frac{\partial}{\partial t} \int c_v T \rho dV + \frac{\partial}{\partial t} \int \frac{1}{2} \bar{g}^2 \nu dV = - \oint \left( c_p T \bar{g} + \frac{1}{2} \bar{g}^3 \nu^2 \right) \cdot \bar{N} dA + \frac{dQ}{dt} - \frac{dW}{dt} \quad (\text{B.24})$$

Now, applying the divergence theorem:

$$\frac{\partial}{\partial t} \int c_v T \rho dV + \frac{\partial}{\partial t} \int \frac{1}{2} \bar{g}^2 \nu dV = - \int \left( \nabla \cdot \left( c_p T \bar{g} + \frac{1}{2} \bar{g}^3 \nu^2 \right) \right) dV + \frac{dQ}{dt} - \frac{dW}{dt} \quad (\text{B.25})$$

$$\frac{\partial}{\partial t} (c_v T \rho V) + \frac{\partial}{\partial t} \left( \frac{1}{2} g_x^2 \nu V \right) = -V \frac{\partial}{\partial x} \left( c_p T g_x + \frac{1}{2} g_x^3 \nu^2 \right) + \frac{dQ}{dt} - \frac{dW}{dt} \quad (\text{B.26})$$

$$\frac{\partial}{\partial t} (m c_v T) + \frac{\partial}{\partial t} \left( \frac{(g_x V)^2}{2m} \right) = -V \frac{\partial}{\partial x} (c_p T g_x) - \frac{\partial}{\partial x} \left( \frac{1}{2} g_x^3 \nu^2 V \right) + \frac{dQ}{dt} - \frac{dW}{dt} \quad (\text{B.27})$$

Equation B.7 can be rewritten as follows:

$$\frac{\partial m}{\partial t} = -V \frac{\partial g}{\partial x} \quad (\text{B.28})$$

## B.5

Equation B.28 can then be substituted into the second term of Equation B.27 as follows:

$$\frac{\partial}{\partial t} \left( \frac{(g_x V)^2}{2m} \right) = \frac{g_x V}{m} \frac{\partial}{\partial t} (g_x V) - \frac{(g_x V)^2}{2m^2} \frac{\partial m}{\partial t} = g_x \nu \frac{\partial}{\partial t} (g_x V) + \frac{1}{2} (g_x \nu)^2 V \frac{\partial g}{\partial x} \quad (\text{B.29})$$

Equation B.12 can also be expanded as follows:

$$\frac{\partial}{\partial t} (g_x V) = -V \frac{\partial p}{\partial x} - F_x - V \frac{\partial}{\partial x} (g_x^2 \nu) \quad (\text{B.30})$$

$$\frac{\partial}{\partial t} (g_x V) = -V \frac{\partial p}{\partial x} - F_x - 2g_x \nu \frac{\partial g}{\partial x} + g_x^2 \frac{\partial \nu}{\partial x} \quad (\text{B.31})$$

Now, after substituting Equation B.31 into Equation B.29, Equation B.29 can be written as follows:

$$\frac{\partial}{\partial t} \left( \frac{(g_x V)^2}{2m} \right) = -g_x \nu V \frac{\partial p}{\partial x} - g_x \nu F_x - \left( \frac{3}{2} (g_x \nu)^2 V \frac{\partial g}{\partial x} + g_x^3 \nu V \frac{\partial \nu}{\partial x} \right) \quad (\text{B.32})$$

Looking back at Equation B.27, the following can be said:

$$\frac{\partial}{\partial x} \left( \frac{1}{2} g_x^3 \nu^2 V \right) = \frac{3}{2} (g_x \nu)^2 V \frac{\partial g}{\partial x} + g_x^3 \nu V \frac{\partial \nu}{\partial x} \quad (\text{B.33})$$

And, by now substituting Equation B.32 and B.33 into Equation B.27, we get the following:

$$\frac{\partial}{\partial t} (m c_v T) + V \frac{\partial}{\partial x} (c_p T g_x) - \frac{dQ}{dt} + \frac{dW}{dt} = g_x \nu \left( V \frac{\partial p}{\partial x} + F_x \right) \quad (\text{B.34})$$

### Neglecting kinetic energy of the working fluid

Taking Equation B.14 and neglecting the kinetic energy of the working fluid, we get the following:

$$\frac{\partial}{\partial t} \int u \rho dV = - \oint u \rho \bar{v} \cdot \bar{N} dA - \oint (p \bar{v}) \cdot \bar{N} dA + \frac{dQ}{dt} - \frac{dW}{dt} \quad (\text{B.35})$$

After substituting the relations for  $\bar{v}$  and  $h$  given by Equations B.15 and B.18 respectively, we get:

$$\frac{\partial}{\partial t} \int u \rho dV = - \oint (h \bar{g}) \cdot \bar{N} dA + \frac{dQ}{dt} - \frac{dW}{dt} \quad (\text{B.36})$$

## B.6

And now, by substituting the relations for  $u$  and  $h$  given by Equations B.21 and B.23 respectively, we get:

$$\frac{\partial}{\partial t} \int c_v T \rho dV = - \oint (c_p T \bar{g}) \cdot \bar{N} dA + \frac{dQ}{dt} - \frac{dW}{dt} \quad (\text{B.37})$$

After applying the divergence theorem and reducing to the one-dimensional case:

$$\frac{\partial}{\partial t} \int c_v T \rho dV = - \int (\nabla \cdot (c_p T \bar{g})) dV + \frac{dQ}{dt} - \frac{dW}{dt} \quad (\text{B.38})$$

$$\frac{\partial}{\partial t} (m c_v T) + V \frac{\partial}{\partial x} (c_p T g_x) - \frac{dQ}{dt} + \frac{dW}{dt} = 0 \quad (\text{B.39})$$

### Comparison of including and neglecting the kinetic energy of the working fluid

When comparing the final equations of including and neglecting the kinetic energy of the working fluid (Equations B.34 and B.39 respectively), we see that the inclusion of the kinetic energy is captured by the following term:

$$g_x \nu \left( V \frac{\partial p}{\partial x} + F_x \right)$$

This implies that:

$$g_x \nu \left( V \frac{\partial p}{\partial x} + F_x \right) = 0 \quad (\text{B.40})$$

$$V \frac{\partial p}{\partial x} + F_x = 0 \quad (\text{B.41})$$

Now, substituting Equation B.41 into Equation B.12, we get the following:

$$\frac{\partial}{\partial t} (g_x V) + V \frac{\partial}{\partial x} (g_x^2 \nu) = 0 \quad (\text{B.42})$$

This, as Urieli (1977) points out, reduces the conservation of momentum equation to a quasi-steady state (Equation B.41). The conservation of momentum equation is reduced to include only the terms for the normal pressure force ( $V \partial p / \partial x$ ) and the frictional drag force ( $F_x$ ), these making up the net applied force on the working fluid in the control volume.

## B.2 Discretisation

The discretisation of the fundamental equations of conservation is done so that they can be applied to the cell and nodal network model, as discussed in Chapter 3.3 and illustrated in Figure B.2.

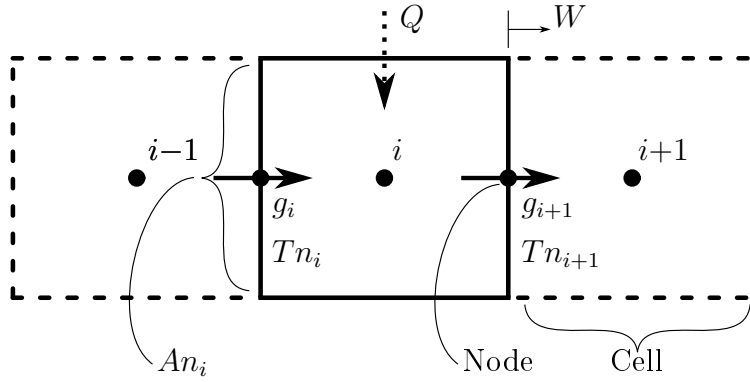


**Figure B.2:** Illustration of cells and nodes.

### B.2.1 Mass

Taking the conservation of mass equation:

$$\frac{\partial m}{\partial t} + V \frac{\partial g}{\partial x} = 0 \quad (\text{B.43})$$

And now discretising:

$$\frac{\partial m_i}{\partial t} = g_i A n_i - g_{i+1} A n_{i+1} \quad (\text{B.44})$$

### B.2.2 Energy

Taking the conservation of energy equation:

$$\frac{\partial}{\partial t} (m c_v T) + V \frac{\partial}{\partial x} (c_p T g_x) - \frac{dQ}{dt} + \frac{dW}{dt} = 0 \quad (\text{B.45})$$

$$c_v \left( m \frac{\partial T}{\partial t} + T \frac{\partial m}{\partial t} \right) = \frac{dQ}{dt} - \frac{dW}{dt} - V \frac{\partial}{\partial x} (c_p T g_x) \quad (\text{B.46})$$

$$\frac{\partial T}{\partial t} = -\frac{T}{m} \left( \frac{\partial m}{\partial t} \right) + \frac{1}{m c_v} \left[ \frac{dQ}{dt} - \frac{dW}{dt} - V \frac{\partial}{\partial x} (c_p T g_x) \right] \quad (\text{B.47})$$

And now discretising:

$$\frac{\partial T_i}{\partial t} = -\frac{T_i}{m_i} \left( \frac{\partial m_i}{\partial t} \right) + \frac{1}{m_i c_{v_i}} \left[ \frac{dQ_i}{dt} - \frac{dW_i}{dt} + c_{p_i} (A n_i T n_i g_i - A n_{i+1} T n_{i+1} g_{i+1}) \right] \quad (\text{B.48})$$

And finally, by substituting Equation B.44 into Equation B.48 we get:

$$\frac{\partial T_i}{\partial t} = \frac{T_i}{m_i} (A n_{i+1} g_{i+1} - A n_i g_i) + \frac{1}{m_i c_{v_i}} \left[ \frac{dQ_i}{dt} - \frac{dW_i}{dt} + c_{p_i} (A n_i T n_i g_i - A n_{i+1} T n_{i+1} g_{i+1}) \right] \quad (\text{B.49})$$



## C. Source code

```

%Function to determine dynamic viscosity @ T [K] for p = 101.325 kPa
%-----
function [u] = DynamicViscosity(material, T)
    if strcmp(material, 'air')
        a = -1.93828643944767E-18;
        b = 1.03241761802884E-14;
        c = -2.37510347996523E-11;
        d = 4.61684702994251E-08;
        e = 1.73767171721498E-05;
        u = @(x) a.*x.^4 + b.*x.^3 + c.*x.^2 + d.*x + e;
    end
    u = u(T-273.15);
end

%Function to determine rate of temperature change by applying the
%conservation of energy equation
%-----
function DT = Energy(Anw, Ane, gw, ge, Tnw, Tne, T, m, ...
    DQ, DW, cp, cv)
    DT = (T/m)*(Ane*ge - Anw*gw) + (1.0/(m*cv))*(DQ - DW + ...
        cp*(Anw*gw*Tnw - Ane*ge*Tne));
end

%Function to return cross-sectional areas, length of displacer and
%hydraulic diameter
%-----
function [Dh, Ld, Ac, Ak, Ar, Ah, Ae] = EngineParameters(Lk, Lr, Lh)
    d = 0.03598; %bore [m]
    drod = 0.014; %displacer rod [m]
    d_i = 0.034; %inner annulus [m]
    d_o = 0.03598; %outer annulus [m]
    Dh = d_o - d_i; %hydraulic diameter [m]
    dd = 0.034; %displacer diameter [m]
    Ld = 0.092; %displacer length [m]

    %cross sectional areas
    Ac = pi*(dd^2.0 - drod^2.0)/4.0;
    Ak = pi*(d_o^2.0 - d_i^2.0)/4.0;
    Ar = pi*(d_o^2.0 - d_i^2.0)/4.0;
    Ah = pi*(d_o^2.0 - d_i^2.0)/4.0;

```

```

    Ae = pi*dd^2.0/4.0;
end

%Function to determine integral by using Euler's method
%-----
function y = Euler(y0, h, dydx)
    y = y0 + h*dydx;
end

%Function to determine specific heat capacity at
%constant pressure @ T [K] for p = 101.325 kPa
%-----
function [cp] = fcp(material, T)
    if strcmp(material, 'air')
        a = 6.20664706257343E-17;
        b = -4.274223250259E-13;
        c = 1.17280812389388E-09;
        d = -1.60750316621237E-06;
        e = 1.05250643343431E-03;
        f = -7.66346173166097E-02;
        g = 1007.59606051261;
        cp = @(x) a.*x.^6 + b.*x.^5 + c.*x.^4 + d.*x.^3 + ...
            e.*x.^2 + f.*x + g;
    end
    cp = cp(T-273.15);
end

%Function to determine thermal conductivity @ T [K] for p = 101.325 kPa
%-----
function [k] = ThermalConductivity(material, T)
    if strcmp(material, 'air')
        a = 4.63950664042692E-12;
        b = -2.5215622354923E-08;
        c = 7.56202902385889E-05;
        d = 2.36359591238952E-02;
        k = @(x) a.*x.^3 + b.*x.^2 + c.*x + d;
    end
    k = k(T-273.15);
end
%-----
%-----
%Title: main.m
%Date: 15 October 2014

```

```

%Author: I.N. Deetlefs (15071618)
%
%Description:
%   Theoretical simulation model for an FPSE. Piston and displacer
%   motions are determined by a force balance while the working
%   space is solved by a quasi-static model.
%-----
tic; %start stop watch
clear; clc; close all; %clear all variables and figures
file_save = 'Nu50_thesis'; %file name for results

%simulation parameters
dt = 0.00001;
Nplot = 100; %how often to plot [number of iterations]
xcell = 0.001; %cell widths [m]
k_end = 80000; %number of iterations

%plotting parameters
Nplot_track = Nplot; %tracking variable
FinalLoopSwitch = 0; %checks when simulation goes into final loop

%engine parameters
Nu = 50; %Nusselt number
C_Fd = 0; %displacer friction coefficient
C_Fp = 6; %piston friction coefficient
md = 0.076; %displacer mass [kg]
mp = 0.511; %piston mass [kg]
kd = 162.8642; %displacer stiffness [N/m]
kp = 270.8892; %piston stiffness [N/m]

%inputs from test data (t=0)
%-----
xd_test = 0.095038068916050; %displacer position from experiment [m]
xp_test = 0.089635135245578; %piston position from experiment [m]
xkd_zero = 0.081054817049745; %displacer zero position [m]
xkp_zero = 0.103741259912878; %piston zero position [m]
p_test = 133686.3964034972; %pressure from experiment [Pa]
p_barometer = 99519; %barometric pressure [Pa]

%checking variables (physical clearances)
xd_max = 0.095906066787151; %[m]
xp_flush = 0.079554437400735; %[m]

```

### C.3

```

%wall temperatures
Twall_1 = 426.7188233617241; %[K]
Twall_2 = 389.2769280772442; %[K]
Twall_3 = 366.4741320227125; %[K]
Twall_4 = 329.0048019806527; %[K]

%set markers along wall and other dimensions
%-----
marker(1) = 15; %end of heater end cap
marker(2) = 15; %interface (h and e)
marker(3) = 54; %interface (r and h)
marker(4) = 94; %interface (k and r)
marker(5) = 133; %interface (c and k)
marker(6) = 111; %start of cooling jacket
markerH1 = 17; %top of heating section
markerH2 = 39; %bottom of heating section

Lk = 0.001*(marker(5) - marker(4)); %length of cooler
Lr = 0.001*(marker(4) - marker(3)); %length of regenerator
Lh = 0.001*(marker(3) - marker(2)); %length of heater
[Dh, Ld, Ac, Ak, Ar, Ah, Ae] = EngineParameters(Lk, Lr, Lh);

%wall grid
%-----
%(1) set areas
%heater head end cap
for i = 1:marker(1)-1
    id = 0.001*(36.98 - 2*(15+1-i)); %inner node diameter [m]
    od = id + 2*0.001; %outer node diameter [m]
    Awall(i) = (od^2 - id^2)*pi/4.0; %[m^2] heat transfer area
end

%corner cell
Awall(marker(1)) = 0;

%heater head tube
for i = marker(1)+1:marker(6)
    id = 0.001*35.98; %inner diameter of tube [m]
    Awall(i) = xcell*pi*id; %[m^2] heat transfer area
end

%(2) set temperatures
%curve fit for specified temperatures from experiment

```

```

Twall_spec = [Twall_1 Twall_2 Twall_3 Twall_4]; %[K]
xwall_spec = [31.09 50.08 69.03 87.65]; %[mm]
Twall_spec_poly = polyfit(xwall_spec, Twall_spec, 1);

%extrapolate temperatures between marker(6) and markerH2
for i = markerH2:marker(6)
    Twall(i) = polyval(Twall_spec_poly, i - 0.5 - marker(1)); %[K]
end

%extrapolate temperatures between markerH2 and markerH1
for i = markerH1+1:markerH2-1
    Twall(i) = Twall(markerH2); %[K]
end

%extrapolate temperatures up to markerH1
for i = 1:markerH1
    Twall(i) = Twall(markerH2); %[K]
end

%lumped mass
i = marker(6)+1;
Twall(i) = polyval(Twall_spec_poly, i-1-marker(1)); %[K]

%working space
%-----
%(1) set number of cells for different spaces
Nc = 1; %compression space cells
Nk = Lk/xcell; %cooler space cells
Nr = Lr/xcell; %regenerator space cells
Nh = Lh/xcell; %heater space cells
Ne = 1; %expansion space cells

Ncell = Nc+Nk+Nr+Nh+Ne; %total number of cells
Nn = Ncell+1; %total number of nodes

%set span of cells for each space
Nc_span = 1:Nc;
Nk_span = Nc+1:Nc+Nk;
Nr_span = Nc+Nk+1:Nc+Nk+Nr;
Nh_span = Nc+Nk+Nr+1:Nc+Nk+Nr+Nh;
Ne_span = Nc+Nk+Nr+Nh+1:Nc+Nk+Nr+Nh+Ne;

%(2) set node areas and cell widths

```

```

An(Nc_span) = Ac;
An(Nk_span) = Ak;
An(Nr_span) = Ar;
An(Nh_span) = Ah;
An(Ne_span) = Ae;

x(Nc_span) = xcell;
x(Nk_span) = xcell;
x(Nr_span) = xcell;
x(Nh_span) = xcell;
x(Ne_span) = xcell;

%Interfaces (correction for An areas)
An(Nc+1) = min(Ac, Ak);
An(Nc+Nk+1) = min(Ak, Ar);
An(Nc+Nk+Nr+1) = min(Ar,Ah);
An(Nc+Nk+Nr+Nh+1) = min(Ah,Ae);
An(Nc+Nk+Nr+Nh+Ne+1) = Ae;

%temperature and area indexing for k, r, h
%-----
%check for cross over
if marker(5) > marker(6)
    markerC0 = marker(6);
else
    markerC0 = marker(5);
end

for i = marker(2)+1:markerC0
    Tindex(Ncell-i+marker(2)) = i;
    Aindex(Ncell-i+marker(2)) = i;
end

i_hold = Ncell-markerC0+marker(2);
if i_hold>2
    for i = i_hold-1:-1:2
        Tindex(i) = size(Twall, 2);
        Aindex(i) = size(Twall, 2)-1; %just set to node at marker(6)
    end
end

%set initial conditions
%-----

```

```

R = 287.0; %air @ 300K, @ atm [J/kg.K]
ginit = 0.0; %mass flux [kg/m^2.s]
pinit = p_test(1); %initial pressure of experiment [Pa]

%clearance variables (set functions)
fxclc1 = @(xd) 0.001*(marker(5) - marker(1)) - Ld - (xd_max - xd);
fxclc2 = @(xp) 0.001*(131.5 - (marker(6)-marker(1))) - (xp-xp_flush);
fxclc3 = @(xp) 0.001*(131.5 - (marker(5)-marker(1))) - (xp-xp_flush);
fxcl_sleeve = @(xp) 0.020 - (xp - xp_flush);
fxcle = @(xd) (xd_max - xd) - 0.001*(marker(2) - marker(1));

%functions for expansion and compression spaces
fxe = @(xd) xd_max - xd; % [m]
fxc = @(xd, xp) 0.0395 - (xd_max - xd) - (xp - xp_flush); % [m]

%motion variables (set to start of experiment)
xd = xd_test;
xp = xp_test;
vd = 0; % [m/s]
vp = 0; % [m/s]
xclc1 = fxclc1(xd_test);
xclc2 = fxclc2(xp_test);
xclc3 = fxclc3(xp_test);
xcl_sleeve = fxcl_sleeve(xp_test);
xcle = fxcle(xd_test);
xc = fxc(xd_test, xp_test); %compression space length
xe = fxe(xd_test); %expansion space length
Vc = Ac*xc/Nc + Ak*xclc3; %[m^3]
Ve = Ae*xe/Ne + Ah*0.001*(marker(2) - marker(1)); %[m^3]

%(1) nodes
g = ones(1,Nn)*ginit;
Tn = zeros(1,Nn);

%(2) cells
%set T = Twall
for i = 1:Ncell
    %space c
    if (i>=1 & i<=Nc)
        T(i) = Twall(end);
    end

    %space k through h

```

```

    if (i>Nc & i<=Nc+Nk+Nr+Nh)
        T(i) = Twall(Tindex(i));
    end

    %space e
    if (i>Nc+Nk+Nr+Nh & i<=Nc+Nk+Nr+Nh+Ne)
        T(i) = Twall(1);
    end
end

V(Nc_span) = Vc;
V(Nk_span) = Ak*x(Nk_span);
V(Nr_span) = Ar*x(Nr_span);
V(Nh_span) = Ah*x(Nh_span);
V(Ne_span) = Ve;

p = ones(1,Ncell)*pinit;
m = p.*V./(R.*T);
M = sum(m);

%rates of change
Dp = zeros(1,Ncell);
DT = zeros(1,Ncell);
Dm = zeros(1,Ncell);

%other
Q = zeros(1,Ncell);
W = zeros(1,Ncell);
pBounce = p_barometer;

%holding variables
%-----
%motion variables
xd_hold = []; xp_hold = []; vd_hold = []; vp_hold = [];

%nodes
g_hold = [];

%cells
DQ_hold = []; DT_hold = [];
p_hold = []; T_hold = []; m_hold = []; V_hold = [];

%other

```



```

Q_hold = []; W_hold = [];

%start simulation -----
for k = 1:k_end
    %determine piston and displacer accelerations
    %-----
    %displacer
    Fd = C_Fd*vd;
    Dvd = (pBounce*(Ae-Ac) + p(1)*Ac - p(end)*Ae - ...
           kd*(xd - xkd_zero) - Fd)/md;

    %piston
    Fp = C_Fp*vp;
    Dvp = ((pBounce-p(1))*(Ac+Ak) - kp*(xp - xkp_zero) - Fp)/mp;

    %clearance check (check only for important clearances)
    %-----
    if xe<0
        display('error: xe<0')
        pause
    end

    if xc<0
        display('error: xc<0')
        pause
    end

    if xclc3<0
        display('error: xclc3<0')
        pause
    end

    %cons. of energy equation: Determine rate of temperature change
    %-----
    %set conditional flux temperatures
    for i = 2:Nn-1 %from 2nd node to 2nd last node
        if (g(i)>=0)
            Tn(i) = T(i-1);
        else
            Tn(i) = T(i);
        end
    end
end

```

```

%determine DQ and DW
for i=1:Ncell
    cp = fcp('air', T(i)); %[J/kg.K]
    cv = cp - R; %[J/kg.K]
    u = DynamicViscosity('air', T(i)); %[kg.m/s]
    k_air = ThermalConductivity('air', T(i)); %[W/m.K]
    h = Nu*k_air/Dh; %[W/m.K]

    %space c
    if (i>=1 & i<=Nc)
        if xclc3 < xclc2
            DQ(i) = h*(xclc3*pi*0.03598^2)*(Twall(end) - T(i));
        else
            DQ(i) = h*(xclc2*pi*0.03598^2)*(Twall(end) - T(i));
            for j = marker(5)+1:marker(6)
                DQ(i) = DQ(i) + h*Awall(j)*(Twall(j) - T(i));
            end
        end
        DV(i) = Ac*(-vp+vd) + Ak*(-vp);
        DW(i) = p(i)*DV(i);
    end

    %space k through h
    if (i>Nc & i<=Nc+Nk+Nr+Nh)
        DQ(i) = h*Awall(Aindex(i))*(Twall(Tindex(i)) - T(i));
        DV(i) = 0.0;
        DW(i) = 0.0;
    end

    %space e
    if (i>Nc+Nk+Nr+Nh & i<=Nc+Nk+Nr+Nh+Ne)
        DQ(i) = 0;
        for j = 1:marker(1)
            DQ(i) = DQ(i) + h*Awall(j)*(Twall(j) - T(i));
        end

        for j = marker(1)+1:marker(2)
            DQ(i) = DQ(i) + h*Awall(j)*(Twall(j) - T(i));
        end

        DV(i) = Ae*(-vd);
        DW(i) = p(i)*DV(i);
    end
end

```

```

        end
    end

    %apply energy equation
    for i = 1:Ncell
        DT(i) = Energy(An(i), An(i+1), g(i), g(i+1), Tn(i), ...
            Tn(i+1), T(i), m(i), DQ(i), DW(i), cp, cv);
    end

    %determine rate of pressure change and mass change
    %-----
    tempVar = sum(m.*(DT./T - DV./V));
    Dp = (p./M).*tempVar; %rate of pressure change in working space

    for i=1:Ncell
        Dm(i) = m(i)*(Dp(i)/p(i) + DV(i)/V(i) - DT(i)/T(i));
    end

    %write values to file at designated intervals
    %-----
    if (Nplot_track == Nplot)
        clc
        fprintf('%0.3f%% complete \n', 100*k/k_end); %completion
        Nplot_track = 0;

        %set energy integrals to zero if the loop in first time step
        if (FinalLoopSwitch == 0)
            Q = zeros(1,Ncell);
            W = zeros(1,Ncell);
        end

        xd_hold = [xd_hold; xd];
        xp_hold = [xp_hold; xp];
        vd_hold = [vd_hold; vd];
        vp_hold = [vp_hold; vp];
        DQ_hold = [DQ_hold; DQ];
        DT_hold = [DT_hold; DT];
        p_hold = [p_hold; p];
        V_hold = [V_hold; V];
        m_hold = [m_hold; m];
        T_hold = [T_hold; T];
        Q_hold = [Q_hold; Q];
        W_hold = [W_hold; W];
    end

```

```

    g_hold = [g_hold; g];

    FinalLoopSwitch = 1;
end

Nplot_track = Nplot_track + 1;

%calculate new values
xd = Dvd*dt^2.0/2.0 + vd*dt + xd;
xp = Dvp*dt^2.0/2.0 + vp*dt + xp;
xc_new = fxc(xd, xp);
xe_new = fxe(xd);
vc = (xc_new-xc)/dt;
ve = (xe_new-xe)/dt;
xc = xc_new;
xe = xe_new;

%check for collision
if (xc<0.001) & (vc<0) %piston and displacer
    vd = (vd*(md-mp)+2.0*mp*vp)/(md+mp);
    vp = (vp*(mp-md)+2.0*md*vd)/(md+mp);
else if (xe<0.001) & (ve<0) %displacr and heater end cap
    vd = 0;
    vp = Euler(vp, dt, Dvp);
else %no collision
    vd = Euler(vd, dt, Dvd);
    vp = Euler(vp, dt, Dvp);
end
end

xclc1 = fxclc1(xd);
xclc2 = fxclc2(xp);
xclc3 = fxclc3(xp);
xcl_sleeve = fxcl_sleeve(xp);
xcle = fxcle(xd);

for i = 1:Ncell
    Q(i) = Euler(Q(i), dt, DQ(i));

    if i == 1
        V(i) = Ac*xc + Ak*xclc3;
    else if i == Ncell
        V(i) = Ae*xe + Ah*0.001*(marker(2) - marker(1));
    end
end

```

```

        else
            V(i) = Euler(V(i), dt, DV(i));
        end
    end

    W(i) = Euler(W(i), dt, DW(i));
    m(i) = Euler(m(i), dt, Dm(i));
    p(i) = Euler(p(i), dt, Dp(i));
end

T = (p.*V)./(m.*R); %calculate new temperatures

%cons. of mass equation: Mass flux at nodes
for i = 2:Nn-1
    if (i == 2)
        g(i) = -Dm(i-1)/An(i);
    else if (i==Nn-1)
        g(i) = Dm(i)/An(i);
    else
        g(i) = (An(i-1)*g(i-1)-Dm(i-1))/An(i);
    end
end
end
end
%end of simulation -----

%save final values
xd_hold = [xd_hold; xd];
xp_hold = [xp_hold; xp];
vd_hold = [vd_hold; vd];
vp_hold = [vp_hold; vp];
DQ_hold = [DQ_hold; DQ];
DT_hold = [DT_hold; DT];
p_hold = [p_hold; p];
V_hold = [V_hold; V];
m_hold = [m_hold; m];
T_hold = [T_hold; T];
Q_hold = [Q_hold; Q];
W_hold = [W_hold; W];
g_hold = [g_hold; g];

save(file_save);
toc; %end stop watch

```

## D. Sensitivity analysis

Since a sensitivity analysis focuses on unknown input parameters,  $m_p$ ,  $m_d$ ,  $k_p$ ,  $k_d$  and  $p_{bounce}$  were not considered, since their values were measured and are known. The results for a variation in  $Nu$  were dealt with in Section 3.8 (page 37).

For completeness, however, a sensitivity analysis was performed for the effect of friction on the displacer. Friction on the displacer is represented by  $Ff_{pd}$ , as explained in Chapter 3.

Firstly,  $Ff_{pd}$  can be expanded as follows:

$$Ff_{pd} = C_{pd}(v_d - v_p) \quad (\text{D.1})$$

The value of  $C_{pd}$  for the B-10B demonstrator engine was measured by Riofrio *et al.* (2008) as 10 N s/m. This sensitivity analysis takes this value for  $C_{pd}$ , as well as a percentage of 50% and 25% (i.e. 5 and 2,5 N s/m). The value for  $Nu$  was set as 50.

As is shown in Figure D.1 (a) to (c), there was a decay in piston and displacer amplitude, as well as a downward creep of both the average piston and displacer positions. The zero position was taken from the experimental test.

There was no use in comparing the piston and displacer motions because of this continuing decay. A comparison rather was made with respect to frequency and phase.

As seen in Table D.1, phase increased with decreasing  $C_{pd}$ , since increasing  $C_{pd}$  means greater coupling between piston and displacer. There seemed to be no pattern with regard to frequency, however. The largest frequency (10,99 Hz) was found for the largest  $C_{pd}$  and then decreased for decreasing  $C_{pd}$ , but increased again to 10,87 Hz for  $C_{pd} = 0$ .

It should also be noted that there were no contact events and the contact assumptions thus have no effect.

The introduction of friction on the displacer is shown to have a debilitating effect on engine operation. As the displacer stroke amplitude decreases, it no longer displaces working fluid effectively between the hot and cold sides of the engine, which decreases the pressure variation, which in turn decreases the piston stroke. When the piston stroke decreases it then affects the displacer stroke, since the pressure variation caused by the movement of the piston is less and the displacer is not driven as effectively any more.

**Table D.1:** Summary of sensitivity analysis results.

Test results	$C_{pd} = 10$	$C_{pd} = 5$	$C_{pd} = 2,5$	$C_{pd} = 0$
Frequency	10,99 Hz	10,87 Hz	10,64 Hz	10,87 Hz
Phase angle between piston and displacer	11,9°	15,7°	19,1°	121,3°

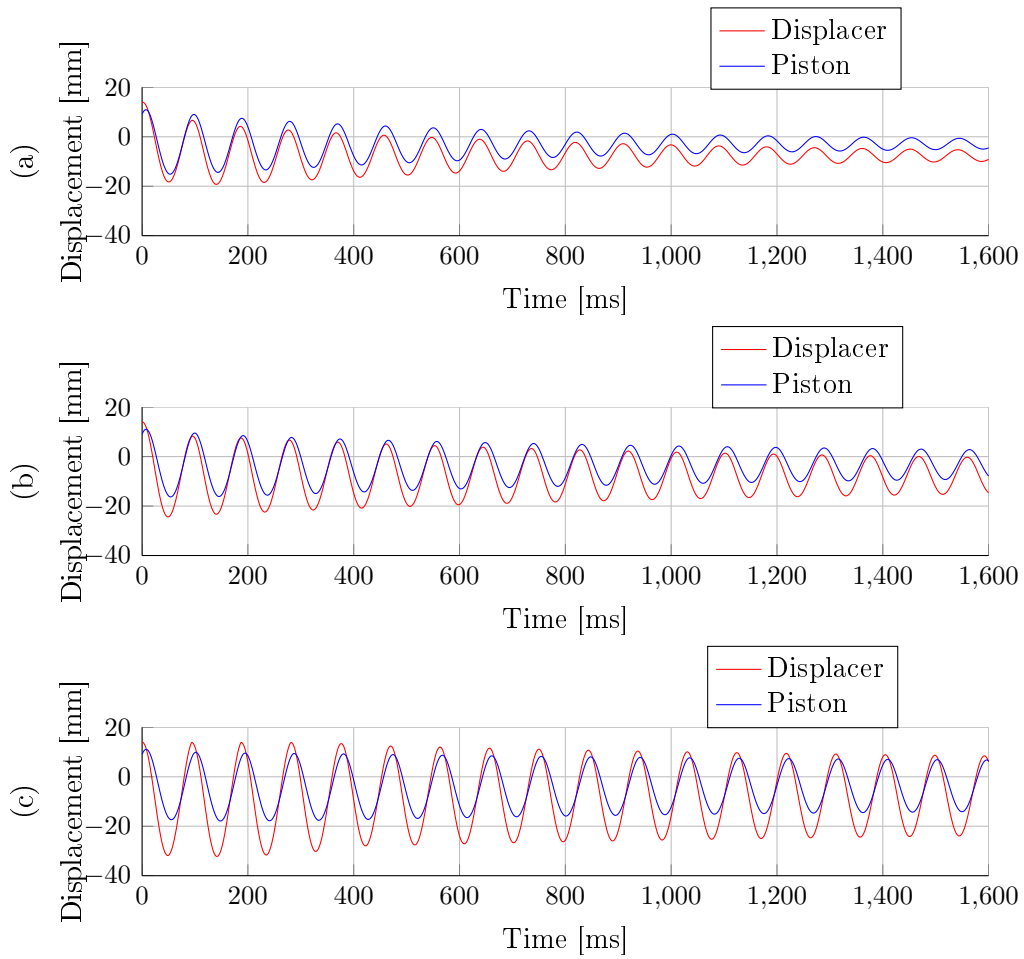


**Figure D.1:** Piston and displacer motions. (a)  $C_{pd} = 10 \text{ N s/m}$ , (b)  $C_{pd} = 5 \text{ N s/m}$ , (c)  $C_{pd} = 2,5 \text{ N s/m}$ .

## List of References

- (2013 August<sup>a</sup>). History of the Stirling Engine.  
Available at: <http://www.microgen-engine.com>
- (2013 September<sup>b</sup>). Stirling-engine Developer Qnergy Acquires US-based Infinia.  
Available at: <http://finance.yahoo.com/news/stirling-engine-developer-qnergy-acquires-1929.html>
- (2014 March<sup>a</sup>). Free Piston Stirling Engine History.  
Available at: <http://www.sunpowerinc.com/about/history.php>
- (2014 February<sup>b</sup>). Introducing The 1 kW Stirling Developer's Kit.  
Available at: <http://us.sunpowerinc.com/1kW.php>
- Çengel, Y. (2006). *HEAT AND MASS TRANSFER: A Practical Approach*. 3rd edn. McGraw-Hill, New York.
- Chen, N. and Griffin, F. (1983). A Review of Stirling Engine Mathematical Models. Tech. Rep., Oak Ridge National Laboratory (ORNL).
- Chen, N. and Griffin, F. (1986). Linear harmonic analysis of free-piston Stirling engines. Tech. Rep., Oak Ridge National Laboratory (ORNL).
- Cheng, C.-H. and Yang, H.-S. (2012). Optimization of geometrical parameters for Stirling engines based on theoretical analysis. *Applied Energy*, vol. 92, pp. 395 – 405. ISSN 0306-2619.
- Cinar, C., Yucesu, S., Topgul, T. and Okur, M. (2005). Beta-type Stirling engine operating at atmospheric pressure. *Applied Energy*, vol. 81, pp. 351 – 357. ISSN 0306-2619.
- Dhar, M. (1999<sup>a</sup>). Stirling Space Engine Program, Volume 1 - Final Report. Tech. Rep., National Aeronautics and Space Administration (NASA).
- Dhar, M. (1999<sup>b</sup>). Stirling Space Engine Program, Volume 2 - Appendixes A, B, C and D. Tech. Rep., National Aeronautics and Space Administration (NASA).
- Dochat, G. (1993). SPDE/SPRE final summary report. Tech. Rep., National Aerospace and Space Administration (NASA).
- Formosa, F. and Fréchette, L.G. (2013). Scaling laws for free piston Stirling engine design: Benefits and challenges of miniaturization. *Energy*, vol. 57, pp. 796 – 808. ISSN 0360-5442.
- Joubert, L.H., Schutte, J., Strauss, J.M. and Dobson, R.T. (2012). Design optimisation of a transverse flux, short stroke, linear generator. In: *Proc. XXth International Conference on Electrical Machines (ICEM)*, pp. 640–646.



- Kankam, M.D. and Rauch, J.S. (1991). Comparative survey of dynamic analyses of free-piston Stirling engines. In: *26th Intersociety Energy Conversion Engineering Conference*.
- Kays, W., Crawford, M. and Weigand, B. (2005). *Convective Heat and Mass Transfer*. 4th edn. McGraw-Hill.
- Lane, N.W. and Beale, W.T. (1997). Free-piston Stirling design features. In: *Eighth International Stirling Engine Conference*.
- Martini, W. (1983). *Stirling Engine Design Manual*. National Aerospace and Space Administration (NASA), 2nd edn.
- Meer, D. and Oriti, S. (2012). Advanced Stirling convertor durability testing: Plans and interim results. In: *10th International Energy Conversion Engineering Conference*.
- Mikalsen, R. and Roskilly, A. (2007). A review of free-piston engine history and applications. *Applied Thermal Engineering*, vol. 27, pp. 2339 – 2352. ISSN 1359-4311.
- Mills, A. and Ganesan, V. (2013). *HEAT TRANSFER*. 2nd edn. Dorling Kindersley, India.
- Noble, J.E., Lehmann, G.A. and Emigh, S.G. (1990). Materials for a Stirling engine heater head. In: *Energy Conversion Engineering Conference (IECEC-90), Proceedings of the 25th Intersociety*, vol. 5, pp. 281 – 291.
- Oriti, S. and Wilson, S. (2011). Advanced Stirling Convertor (ASC-E2) Performance Testing at NASA Glenn Research Center. In: *Nuclear and Emerging Technologies for Space (NETS-2011)*.
- Oriti, S.M. (2012). Extended operation of Stirling convertors at NASA Glenn research center. In: *9th International Energy Conversion Engineering Conference (IECEC)*.
- Peckham Engineering and Tool (1994). Precision linear flexure bearing cartridge. Tech. Rep., Phillips Laboratory, Kirtland Air Force Base, New Mexico.
- Riofrio, J., Al-Dakkan, K., Hofacker, M. and Barth, E. (2008). Control-based design of free-piston Stirling engines. In: *American Control Conference*, pp. 1533 – 1538.
- Saturno, J. (1994). *SOME MATHEMATICAL MODELS TO DESCRIBE THE DYNAMIC BEHAVIOR OF THE B-10 FREE-PISTON STIRLING ENGINE*. Master's thesis, Ohio University.
- Schreiber, J.G. and Thieme, L.G. (2007). Final Results for the GRC Supporting Technology Development Project for the 110-Watt Stirling Radioisotope Generator (SRG110). In: *Space Technology and Applications International Forum (STAIF-2007)*.

Senft, J. (2007). *MECHANICAL EFFICIENCY OF HEAT ENGINES*. Cambridge University Press.

Sier, R. (1995). *Rev Robert Stirling D.D.: A Biography of the Inventor of the Heat Economiser & Stirling Cycle Engine*. L. A. Mair. ISBN 9780952641704.

Urieli, I. (1977). *A COMPUTER SIMULATION OF STIRLING CYCLE MACHINES*. Ph.D. thesis, Faculty of Engineering, University of the Witwatersrand.

Urieli, I. and Berchowitz, D. (1984). *Stirling cycle engine analysis*. Modern energy studies. A. Hilger. ISBN 9780852744352.